The interplay between occludin and ZO-1 is redox sensitive

Inaugural-Dissertation to obtain the academic degree
Doctor rerum naturalium (Dr. rer. nat.)

Submitted to the Department of Biology, Chemistry and Pharmacy of

Freie Universität Berlin

by

VICTOR MANUEL CASTRO VILLELA
from
Mexico City

This work was performed from August 2007 to December 2010 at the Leibniz-Institut für Molekulare Pharmakologie (FMP) in Berlin, Germany.

1st. Reviewer: PD. Dr. Ingolf E. Blasig

2nd. Reviewer: Prof. Dr. Hartmut Oschkinat

Date of defence: December 7th 2011

Acknowledgments

I would like to thank all of those who in one way or another were involved in the conception, design, preparation, execution, analysis and discussion of the work described in this thesis.

A special note goes to my doctoral supervisor, P.D. Dr. Ingolf E. Blasig, for dedicating a substantial amount of time to guide my scientific steps, for his helpful discussions, continuous encouraging, but in particular for nurturing me.

Jörg Piontek provided me with scientific support and greatly contributed with helpful discussions. Reiner Haseloff provided me invaluable assistance, maintained the hypoxic chamber in working conditions and helped me understand the nature and detection of reactive oxygen species. Barbara Eilemann maintained our cell culture laboratory organized, in pristine conditions, and provided technical expertise in cell culture. Christian Tscheik routinely tested our cultured cells to detect Mycoplasma contamination. Sandra Bittmann provided excellent technical assistance and contributed decisively to increase the sensitivity of the immunodetection procedures. Uwe Schlomann provided useful insights to improve the extraction of fluorescent occludin from cultured cells. Christian Bellmann contributed to optimize the fluorescent-PAGE analysis. Sophie Jankowski and Heather Dickens provided technical assistance with routine laboratory procedures. Jenny Eichhorst and Burkhard Wiesner kept operational the confocal microscopy unit and made sure the microscopes were ready to use whenever they were needed. Susanne Krug and Michael Fromm performed the freeze-fracture electron microscopy procedures.

Victor Manuel Castro Villela

To Eugenia and Mareen

Summary

The blood-brain barrier is the interface between the blood and the central nervous system; one of its key elements is the brain capillary endothelium. The paracellular cleft between the brain capillary endothelial cells is sealed by the tight junctions (TJ), protein complexes that restrict the free diffusion of water and water soluble molecules across that space. The intracellular *zonula occludens* protein 1 (ZO-1) and the transmembranal and TJ-specific protein occludin were the first TJ molecules identified. The structure and physiology of both proteins is not well understood; ZO-1 is considered the scaffolding protein of the TJ, and occludin has been assumed to play a regulatory role on the TJ behavior. Based on in-vitro studies using recombinant fragments of occludin, a redox sensitive function of occludin was hypothesized.

Here, it is shown that occludin dimerizes in a redox sensitive manner by forming an intracellular disulfide bridge involving the cysteine 409 (in the C-terminal domain of human occludin). The dimerization is found to be needed for the recruitment of ZO-1 to the plasma membrane. When expressed in a TJ-free cell system, occludin reached the cell membrane and interacted in *trans* with itself. When coexpressed with ZO-1, occludin formed membranal strands and helped ZO-1 to reach the plasma membrane. Under hypoxia or TNF-α induced redox stress, occludin did not dimerize, lost its ability to interact in *trans*, dissociated from ZO-1, and both proteins were delocalized from the plasma membrane. The substitution of the cysteine 409 for alanine (C409A) prevented the dimerization of occludin and the recruitment of ZO-1 to the cell membrane. Although the occludin C409A mutant reached the cell membrane, it did not recruit ZO-1 or formed strands. Based on the experimental data a structural model for the redox-sensitive dimerization of occludin and the interaction of occludin and ZO-1 was proposed.

This work demonstrates how the cellular expression and interplay of occludin and ZO-1 are redox sensitive. After the onset of hypoxia, changes in the intracellular redox potential hinder the interaction of occludin with ZO-1, a novel mechanism that contributes to the regulation of TJ. Thus, this work contributes to a better understanding of the function and regulation of TJ in the brain capillaries of patients undergoing hypoxic and/or inflammatory conditions.

Zusammenfassung

Die Blut-Hirn-Schranke ist die Schnittstelle zwischen dem Blut und dem Zentralnervensystem. Die Funktion baut hierbei auf kapilläre Endothelzellen im Gehirn auf. Der parazelluläre Spalt zwischen den Endothelzellen im Gehirn ist durch Tight Junctions (TJ) verschlossen, einen Membranproteinkomplex, der die freie Diffusion von Wasser- oder wasserlöslichen Molekülen verhindert. Das intrazelluläre Zonula occludens Protein 1 (ZO-1) und das transmembrane, TJ-spezifische Protein Occludin waren die ersten identifizierten TJ-Moleküle. Die Struktur und die Physiologie dieser beiden Moleküle sind bisher nicht eindeutig geklärt. Es wird angenommen, dass ZO-1 das Protein für den Gerüstbau der TJ ist und Occludin das Regulationsverhalten der TJ bestimmt. Ausgehend von einer Studie in-vitro mit rekombinierten Occludinfragmenten wird eine redox-empfindliche Funktion von Occludin vermutet.

Hier wird zum ersten Mal demonstriert, dass eine Dimerisierung von Occludin auf eine redox-sensibel Weise durch das Ausbilden einer intrazellulären Disulfidbrücke mit Cysteine 409 (am C-terminalen Ende von humanem Occludin) stattfindet. Dieses Dimer wird für die Anlagerung von ZO-1 an die Plasmamembran benötigt. Wenn Occludin in einem TJ-freien Zellsystem synthetisiert wird, erreicht es die Zellmembran wo es in *trans,* mit sich selbst interagiert. Falls in diesem System aber ebenfalls ZO-1 synthetisiert wird, formt es mit Occludin membranartige Stränge. Occludin, als dimer, erleichtert ZO-1 die Plasmamembran zu erreichen. Durch Sauerstoffmangel oder auch oxidativen Stress, der durch TNF- α hervorgerufen wurde, kann Occludin das Dimer nicht ausbilden und kann dadurch nicht mehr mit sich selbst-interagieren, trennt sich von ZO-1, sodass beide Proteine von der Plasmamembran delokalisiert werden. Wird Cystine 409 durch Alanine (C409A) ersetzt, wird sowohl die Dimerisierung von Occludin als auch die Anlagerung von ZO-1 an die Zellmembran verhindert. Obwohl die Occludin C409A Mutante die Zellmembran erreicht, regiert es nicht mit ZO-1 oder bildet Stränge aus. Basierend auf diesen Experimentdaten ist ein strukturelles Modell des redox-sensitiven Dimers von Occludin und der Interaktion von Occludin und ZO-1 geplant.

In dieser Arbeit wird gezeigt, dass die zelluläre Expression und das Zusammenspiel von Occludin und ZO-1 redox-sensibel sind. Bei beginnender Hypoxie (Sauerstoffmangel) verändert sich das interzelluläre Redoxpotenzial, welches das Zusammenspiel von Occludin und ZO-1 verhindern; diesen neuartigen Mechanismus, der zur Regulation der TJ beiträgt. Dadurch trägt diese Arbeit zu einem besseren Verständnis der Funktion und Regulation der TJ in den Gehirn-Kapillaren von Patienten bei, die unter Sauerstoffmangel oder/und Entzündung leiden.

Abbreviations

λ: wavelength
ADP: Adenosine biphosphate
AMP: Anenosine monophosphate
ANOVA: Analysis of variance
ATP: Adenosine triphosphate
ATPase: Adenosine triphosphatase
BBB: BBB
cAMP: Cyclic adenosine monophosphate
cDNA: complementary DNA
CFP: Cyan fluorescent protein
CoA: coenzyme A
DNA: deoxyribunucleic acid
dNTP deoxynucleotide triphosphate
DTT: Dithiothreitol
E. coli: *Escherichia coli*
E_c: Corrected FRET efficiency
F-PAGE: Fluorescent PAGE
FRET: Fluorescence resonance energy transfer
GFP: Green fluorescent protein
GSH: Reduced glutathione
GuK: Guanylate kinase domain
HEK: Human embryonic kidney
HIF: Hypoxia inducible factor
IFN-γ: Interferon gamma
JAMs: Junctional adhesion molecules
LSCM: Laser scanning confocal microscopy
LSM: Laser scanning microscope
MAGI: Membrane associated guanylate kinase inverted
MAGUK: Membrane associated guanylate kinase
MARVEL: Myelin / lymphocyte and related proteins for vesicle trafficking and membrane link
MDCK: Madin-Darbey canine kidney
NAD^+: Oxidized nicotinamide adenine dinucleotide
NADH: Reduced nicotinamide adenine dinucleotide
NF-κB: Nuclear factor κB
PAGE: Polyacrylamide gel electrophoresis
PCR: Polymerase chain reaction
PDB: Protein databank
PDZ: PSD95/Dlg/ZO-1
PKA: Protein kinase A
PKC: Protein kinase C
PPA: Protein phosphatase A
qλ-FRET: quantum corrected, lambda scanned FRET
RSCB: Research Collaboratory for Structural Bioinformatics
SDS: Sodium dodecyl sulfate
SEM: Standard error of mean
SH3: Src homology 3 domain
SHG: SH3-Hinge-GuK unit of ZO-1
SOD: Superoxide dismutase
TJ: Tight Junctions
TNF-α: Tumor necrosis factor alpha
VEGF: Vascular endothelial growth factor
WT: Wild-type
YFP: Yellow fluorescent protein
ZO-1: *Zonula occludens* protein - 1
ΔG: Change in free energy

Contents

1. INTRODUCTION

1.1 EPITHELIA

Epithelia are specialized tissues that separate two biological compartments and are responsible for maintaining the homeostasis between them. Two properties are crucial in their physiology: they form a physical and chemical barrier and exhibit asymmetric and selective transport. At the cellular level, two main regions are recognized in the epithelial cells, an apical (luminal or outer-side) and basal (abluminal or inner-side).

1.1.1 ENDOTHELIA

Endothelia are the epithelial lining of the heart, blood vessels, lymph vessels and the serous cavities of the body (Gray, 1918, Testut 1896). In the circulatory system, they ensure the luminal flux of blood, interact with blood cells and plasma molecules, secrete hormones, express surface immunological recognition molecules, prevent thrombosis, and modulate the passage of immunological cells, water and substances between the blood and the underlying tissues. Thus the vascular endothelium forms an interface between the circulating blood and the surrounding tissues. In pathological conditions, such as atherosclerosis, inflammation, edema, thrombosis, and hypertension, the vascular endothelium plays an important physiopathogenic role; furthermore, endothelial dysfunction occurs in metabolic diseases like diabetes mellitus or hypercholesterolemia, where the generation of reactive oxygen species by the endothelial cells constitutes a key trigger of endothelial dysfunction (Deanfield et al., 2005).

1.1.2 THE BLOOD BRAIN BARRIER

The blood-brain barrier (BBB) is the anatomo-physiological structure that regulates the traffic of substances between the blood and the brain parenchyma; it significantly contributes to the brain homeostasis, working as a modulated interface between the peripheral circulation and the central nervous system. The existence of the BBB was first evidenced by Paul Ehrlich (Ehrlich P., 1885), its anatomical substrate is the neurovascular unit, formed by the capillary endothelial cells, the extracellular matrix, pericytes, astrocytes, and the neurons. The brain capillary endothelial cells constitute one of the most efficient selectively permeable biological barriers in mammals; they strictly regulate the transport of water, ions, glucose and other molecules to the brain and play a major role in the removal of toxins and drugs from the brain parenchyma.

1.2 THE EPITHELIAL TRANSPORTING PHENOTYPE

In 1843, it was shown that frog-leg muscle preparations that conserved the skin had lower current intensities than the preparations where the skin was removed (du Bois-Reymond 1843); this prompted the study of the electrophysiological properties of the frog skin. Five years later, it was shown that the frog skin had spontaneous electric activity when placed between two compartments filled with ionic solutions, resulting in the inner-solution becoming more electropositive than the outer-solution (du Bois-Reymond 1848). Half a century later, it was demonstrated that such potential depended on the presence of Na^+/Li^+ ions in the solutions, and for the first time, it was proposed that the electric activity of the skin was generated by the asymmetric permeability of the frog skin to those ions (Galleoti 1904 and 1907). It took, however, another half a century to unambiguously demonstrate that the frog skin is, indeed, capable of transporting Na^+, preferentially in the inward direction, in absence of an external electrochemical gradient, and based on the transepithelial electrical conductivity, the frog skin epithelium was represented as an equivalent electrical circuit, that was later evolved into a more detailed "two membrane" model where the net transepithelial transport would be equal to the net flux of Na^+ across the outer and the inner cell membranes (Ussing and Zehran 1951).

1.2.1 THE EPITHELIAL TWO MEMBRANE MODEL

Further studies demonstrated that in the absence of an electric shunt (an electrochemical leak between the two sides of the epithelium), the outer (luminal) and inner (basal) membranes of the epithelial cells had independent electrical properties, and their combined voltage could be added as if they were in a serial electrical circuit, generating a whole transepithelial voltage. The existence of a sodium pumping mechanism was also proposed, since in the model, a pumping mechanism was needed to transport Na^+ ions against their electrical and concentration gradients through the basal membrane of the epithelial cells (Koefoed-Johnsen and Ussing 1958). Coincidentally, one year earlier, in an unrelated work, an ubiquitous membranal Na^+ pump was identified as the Na^+/K^+-ATPase (Skou 1957), so it was suggested that this ATPase was the same Na^+ pump of the epithelial two-membrane model.

The main features of the two-membrane model were that the luminal membrane would allow sodium to passively enter the cell while the basal membrane would actively transport it through the inner membrane while being exchanged by K^+ (that also exits the cell at the basal membrane following its concentration gradient); it also required the intercellular space to be closed, so the ions would not freely diffuse across. A direct implication of this model was that two different complements of transporters had to be differentially expressed in the apical and basal membranes of the cells, so the differential apical and basal transport could be explained by the existence of a different set of transporters (**Fig. 1**).

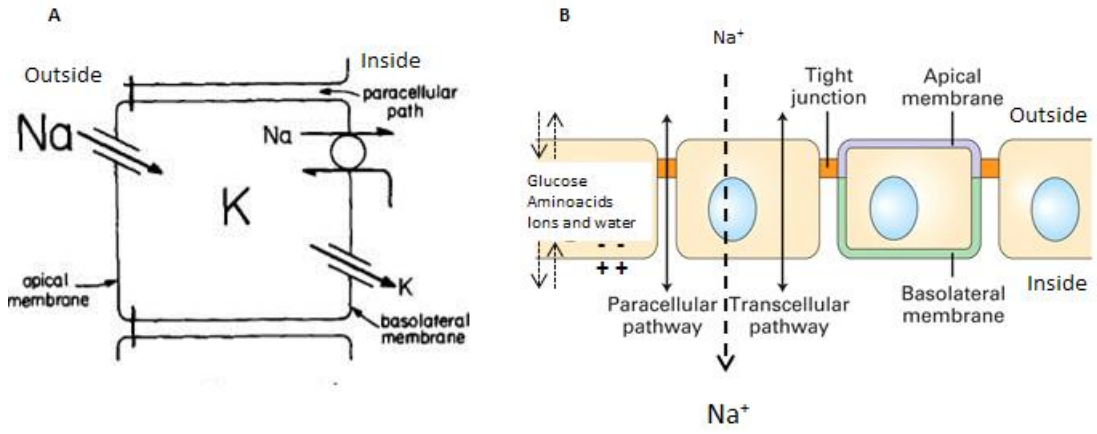

Fig. 1. The epithelial transporting phenotype.

A) The model shows the asymmetric transport capabilities in each of the two membranes of the epithelial cells, as it was proposed by Koefoed-Johnsen and Ussing. The apical membrane is permeably to sodium, while the basolateral membrane is permeable to potassium. A pumping mechanism in the basolateral membrane transports sodium against its electrochemical gradient, exchanging it with potassium. For this model to be functional, a barrier should be present between the cells to prevent the free diffusion of ions. (Fig. modified from Dawson et al. 2011).

B) Current conceptual view of the two membrane model of Koefoed-Johnsen and Ussing. This model defines the epithelial phenotype. Two transport pathways are distinguished, through the cells (transcellular), and across the intercellular space (paracellular). The paracellular space is sealed by membrane protein complexes known as TJ. The membrane polarity (apical and basolateral domains) induced by the TJ is paramount in the proper function of epithelia. The vectorial transport of sodium generates an electrochemical gradient that constitutes the driving force needed to transport water, ions, amino acids, glucose, etc., across the epithelia. (Fig. modified from Lodish et. al. 2000)

Epithelia transport not only ions, but also all the water and solutes (e.g. glucose and amino acids) required to maintain the homeostasis between the two compartments they separate. Epithelial transport occurs via the transcellular or intercellular pathways. The paracellular space is differentially sealed and the passage of substances across this space is regulated by protein complexes expressed at the cell-cell contact areas of the plasma membranes; these complexes are the tight junctions (TJ); they are the intercellular sealing elements of the epithelial two-membrane model, and their expression also polarizes the cell membranes into apical and basolateral domains.

The vectorial transport of sodium (from the luminal to the abluminal side), and the thereof generated transepithelial electrochemical gradient, constitutes the driving force for all the other epithelial transporters to work. Thus, the transepithelial exchange of glucose, amino acids, water, ions, toxins, etc. is driven by the transport of Na^+ whose vectoriality is determined by the expression of TJ.

1.3 THE TIGHT JUNCTIONS

When Koefoed-Johnsen and Ussing introduced their model, they observed a transepithelial “leakage” of ions not explained by the model they proposed. Later on it was shown that the movement of ions through the paracellular space was an important contribution to the so-called “electrical shunt

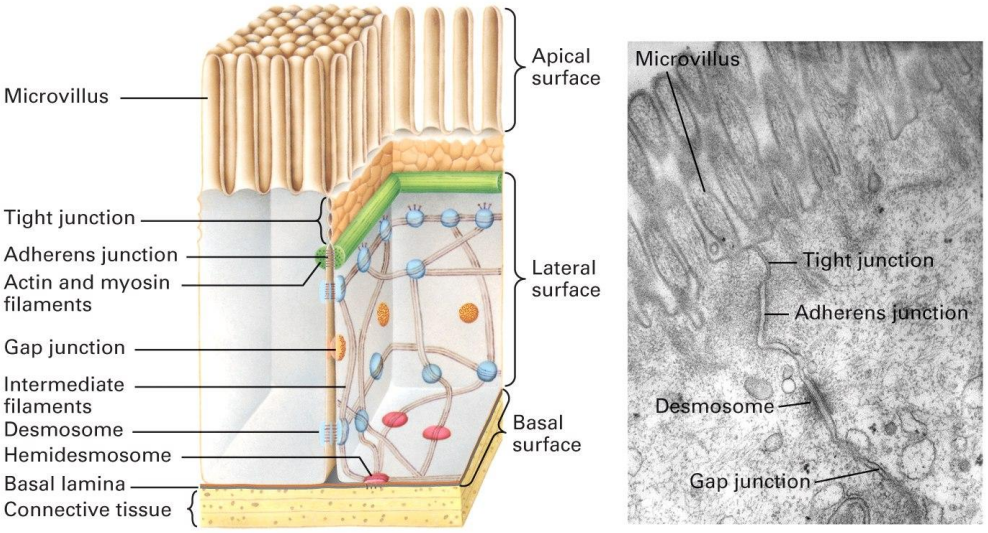

Fig. 2. Junctional complexes in epithelial cells. The three main cell-junctional complexes identified by electron microscopy are the TJ, adherens junctions and desmosomes. From them, the TJ are the most apical complexes and effectively close the paracellular cleft. The gap junctions form intercellular communication channels. All junctional complexes are linked to the cell cytoskeleton. (Figure modified from Lodish et al., 2000)

pathway" (Ussing and Windhager 1964). A large range of paracellular conductivities were identified for different tissues and led to the distinction between "tight" and "leaky" epithelia that respectively expressed low and high transepithelial conductivities (Frömter and Diamond 1972). In fact, the TJ allow the selective paracellular flux of ions, depending on their charge and size, this varies between epithelia, depending on their particular molecular TJ composition (Spring 1998). The property of the TJ to strictly regulate the passage of ions across the paracellular space is known as their "barrier" function, and their ability to prevent the diffusion of proteins and lipids between the apical and basolateral membrane domains is considered their "fence" function (Tsukita et al., 2001).

The systematic analysis of cells by electron microscopy was made possible by the advent of a fixation technique that allowed the conservation of the fine microscopic ultrastructure of the cells (Palade 1952), and the ultrastructure of the cellular junctions was first described as a characteristic tripartite junctional complex between epithelial cells (Farquhar and Palade 1963); the three elements of that complex occupied a juxtaluminal position, and they were introduced, from apical to basal direction, as the *Zonula occludens* (tight junction), *Zonula adhaerens* (intermediate junction) and the *Macula adhaerens* (desmosome).

The zonula occludens was characterized by the apparent fusion of the adjacent cell membranes that resulted in the obliteration of the intercellular space over variable distances from the apical border towards the basal side of the cell; within this obliterated area, the dense outer leaflets of the adjoining cell membranes converged to form a single intermediate line. In contrast, the *zonula adhaerens*, located immediately below the *zonula occludens*, left an open intercellular space of approximately 200

Å, while the intercellular separation at the *macula adhaerens* level reached 240 Å (**Fig. 2)**. It was also noted that the *zonula occludens* appeared to function as a paracellular diffusion barrier, impervious to concentrated protein solutions. Later on it was shown that the intermediate junctions (also known as the adherens junctions) and the desmosomes form a mechanical bridge between adjacent cells, while the TJ seal the paracellular space (Schneeberger and Lynch 1992).

The morphology of the TJ is intensively studied by freeze fracture electron microscopy (Tsukita et al., 2001) where they appear as a continuous intramembranal network of particles organized into multi-branched and interconnected fibrils known as TJ-strands. The number of strands and their branching frequency varies notably between different types of epithelia. The accepted structural model of the TJ is that each strand associates laterally with another strand in an opposing membrane forming a *Velcro* that closes the paracellular space (**Fig. 3**).

1.3.1 Molecular composition of the TJ

After the Farquhar's description of the TJ in 1963, 20 years elapsed until the biochemical nature of the Zonula occludens started to be characterized (Stevenson and Goodenough 1983); in 1983, a tight junction-enriched membrane fraction from mouse liver was used as immunogen to generate a monoclonal antiserum that detected a previously unknown protein of ~225 kDa (Stevenson et al., 1986), this was the first TJ protein identified and was named Zonnula occludens – 1 (ZO-1). In 1993, a second component was found, a transmembranal protein of ~65 kDa that was named occludin (Furuse et al., 1993); shortly after, claudin-1 and claudin-2, the first members of a novel

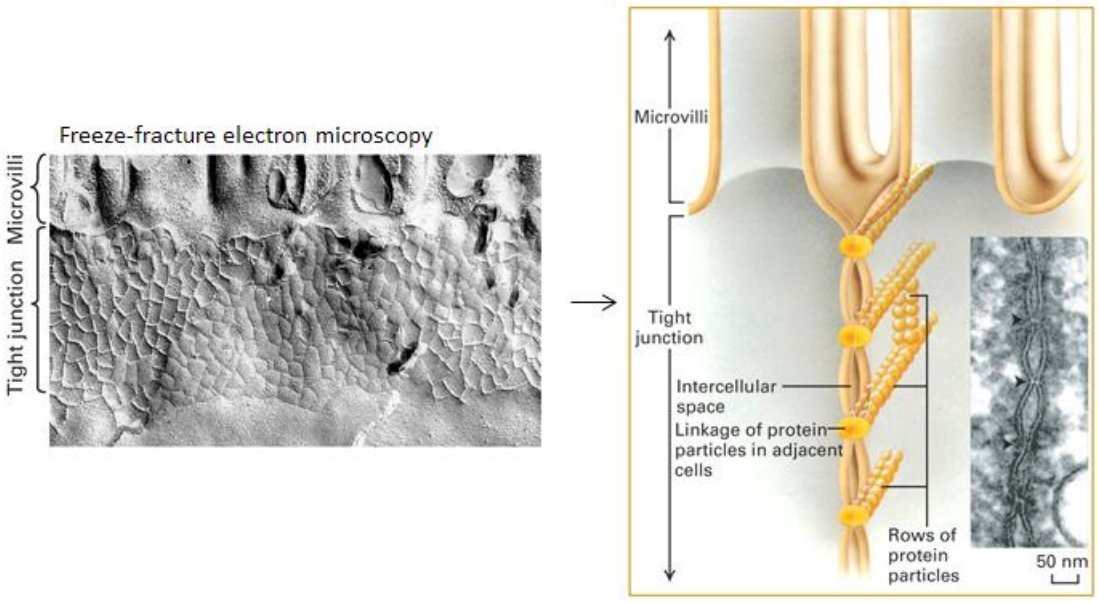

Fig. 3. Tight junction strands. When studied by freeze-fracture electron microscopy, the TJ looks like a network of strands in the cell membrane. These strands are known to be composed of claudins and occludin. These proteins form a bridge across two adjacent membranes, sealing the paracellular space. (Figure modified from Lodish et al., 2000)

transmembranal family of proteins were discovered (Furuse et al., 1998). Currently, more than 40 proteins have been identified as part of the TJ (Gonzalez-Mariscal et al., 2003).

Structurally, the TJ consist of transmembrane and peripheral proteins that interact with each other to form a highly dynamic network; the membranal integral proteins are scaffolded by the peripheral ones that lie immediately below the plasma membrane and link the complexes to the actin cytoskeleton (**Fig. 4**). Additional proteins, involved in signal transduction, cell polarity and gene expression also associate with the TJ network.

1.3.2 TRANSMEMBRANAL PROTEINS

The TJ transmembranal proteins are inserted into the plasma membrane and connect the membranes of adjacent cells and tightly seal the paracellular space. They are grouped in three main families, TJ-associated MARVEL (myelin / lymphocyte and related proteins for vesicle trafficking and membrane link) proteins, claudins, and junctional adhesion molecules (JAMs). MARVEL proteins are related to membrane apposition and vesicular trafficking; the currently known TJ members of this family are occludin, tricellulin and Marvel-D3. The claudin family has 24 members. Both, claudins and MARVEL proteins, are tetraspanins, they have four transmembranal domains, two extracellular loops, one intracellular loop and have their N and C terminal domains in the cytosol. JAMs, on the contrary are single spanning molecules with a large extracellular domain and a short intracellular tail (**Fig. 4)**.

1.3.2.1 Claudins.

Claudins are considered the main constituents of the TJ strands. Although they are tretraspanins, they do not share sequence similarities with occludin (Furuse et al., 1998). In most of epithelial cells, at least two types of claudins are simultaneously expressed (Shin et al., 2006, Tsukita et al., 2001). Claudins mediate the calcium dependent cell-cell adhesion, are responsible for sealing the paracellular space and the formation of paracellular pores that selectively allow the passage of ions through it. The expression of claudin-1 and claudin-2 in L-fibroblasts (TJ free cells) induces cell aggregation, and the formation of cell-cell contact areas, where claudins form well developed networks of strands; if occludin is coexpressed with claudins, both molecules co-polymerize in these strands (Furuse et al., 1998).

Claudins interact with each other in homotypic and heterotypic manner, and also with ZO-1, ZO-2, ZO-3, and the PALS-1 associated tight-junction protein PATJ (Tsukita et al., 2001, Furuse et al., 1999). The cell-type specific variation of the different claudin isoforms in the tight junction, determines the differences in transepithelial electrical resistance and paracellular permeability of different types of epithelia (Shin et al., 2006, Furuse et al., 2001).

1.3.2.2 Occludin

Occludin is also one of the constituents of the TJ strands (Furuse et al, 1993). The N-terminal domain of the molecule is comprised of 66 amino acids, in human, and mediates the ubiquitination of occludin. From the two extracellular loops, the first is structurally flexible and rich in tyrosines and glycines

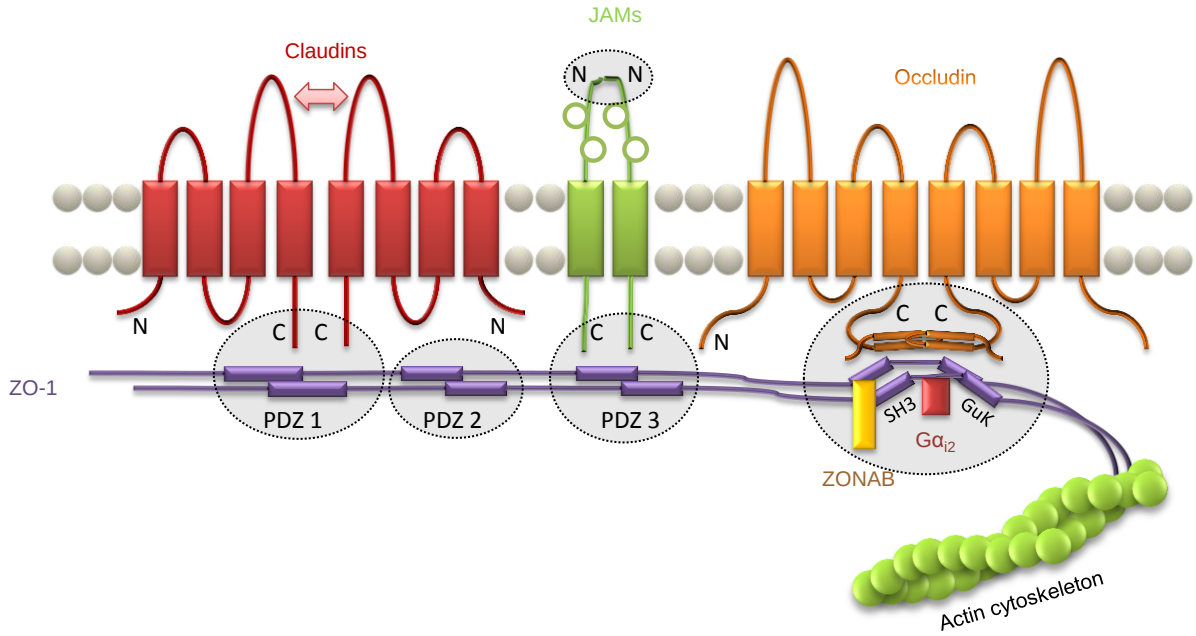

Fig. 4. Schematic representation of the TJ. Claudins, JAMs, and occludin oligomerize in the cell membrane, and are scaffolded by the adaptor protein ZO-1 that, in turn, links them to the submembranal actin cytoskeleton. Claudins are known to self-associate, but their precise oligomerization mechanism is unknown. JAMs dimerize via their N-termini, occludin by its C-terminus, and ZO-1 by its second PDZ domain (PDZ 2). The C-termini of claudins bind to the first PDZ domain (PDZ 1) of ZO-1, the C-termini of JAMs bind to the third PDZ domain (PDZ 3) of ZO-1, and the C-termini of the occludin molecules bind to the SH3-Hinge-GuK unit of ZO-1; to this region, different regulatory molecules attach, like G-proteins (e.g. Gαi2) or the Y-box transcription factor ZONAB. Tricellulin and Marvel-D3 belong to the same family of proteins where occludin belongs (Tight junction associated MARVEL proteins). In mature epithelia, tricellulin is located to the membranal regions where three cells come in contact. The precise oligomerization behavior and molecular interactions of these proteins have not been clearly elucidated yet.

(Ando-Akatsuka et al., 1996), while the second is required for occludin to localize at the TJ and for intercellular adhesion (Van Itallie and Anderson 1997). It has a MARVEL domain that comprises the amino acids 60 to 269 (**Fig. 5)**.

The C-terminal domain of occludin is 256 amino acids long (residues 266 to 522 in human), its presence is needed for occludin to interact with itself, reach the plasma membrane, localize efficiently to the TJ and for their barrier function. It has been suggested, that it mediates endocytosis, and that a basolateral targeting signal might be incorporated into its amino acid sequence, arising the possibility that this domain would regulate the intracellular trafficking of occludin (Nusrat et al., 2000, Feldman et al., 2005).

It has been proposed that the two extracellular loops of occludin, and at least one of its transmembranal domains, are involved in maintaining the selectivity of the TJ barrier (Balda et al., 2000). On the other hand, the expression of occludin chimeras, containing at least one of the occludin transmembranal domains, increased the cellular expression of claudin-4, so it was suggested that

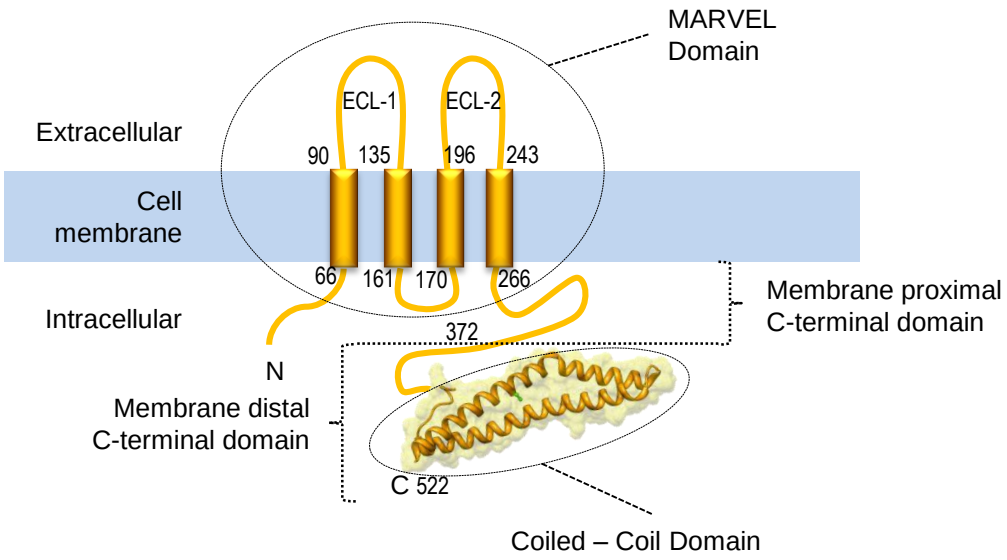

Fig. 5. Schematic representation of occludin. The N and C terminal domains are intracellular. The N-terminus has 66 amino acids. There are four transmembranal domains (TM-1 to 4), one intracellular and two extracellular loops.The MARVEL and coiled-coil domains are shown in dotted circles. The numbers indicate the amino acid positions in the human sequence. The C-terminus is divided into a membrane-proximal (amino acids 266 – 372) and membrane-distal (amino acids 373 to 522) regions.

occludin could be part of a regulatory system that permitted the proper expression of other TJ molecules (Feldman et al., 2005).

The C-terminal domain of occludin can be divided into a membrane-proximal (amino acids 266 to 372 in human), and a membrane-distal domain (amino acids 373 to 522 in human), being the distal domain highly conserved across species (Ando-Akatsuka et al., 1996). The most distal C-terminal region of the molecule (amino acids 426 to 522 in human) is structured into a coiled-coil domain that interacts with the TJ-scaffolding protein ZO-1, as well as F-actin, cingulin, ZO-2 and ZO-3 (Li et al., 2005, Furuse et al., 1994). The association with ZO-1, indirectly links occludin with other molecules that also bind to ZO-1, like claudins, JAM's, and the cytoskeleton. The coiled-coil domain of occludin is also needed for occludin to interact with itself, and with different regulatory proteins like the tyrosine kinase c-Yes, the p85 subunit of the phosphoinositide 3-kinase (PI3K), protein kinases C (PKC's) and the gap junction protein connexin 26 (Nusrat et al., 2000).

The serine/threonine kinase Raf-1 disrupts the TJ by downregulating the expression of occludin, and the overexpression of occludin suppresses tumoral growth induced by Raf-1, in a mechanism that requires the second extracellular loop of occludin (Wang, 2005). Occludin may be involved in the activation of the TJ-associated guanine nucleotide exchange factor GEF-H1/Lfc (Aijaz et al., 2005), and in targeting the tumoral growth factor-ß (TGF-ß) receptors to the TJ; this is a carcinogenic mechanism relevant in the TGF-ß mediated epithelial-to-mesenchymal transition (Barrios-Rodiles et al., 2005). Occludin, together with Claudin-1, is also needed for the hepatitis-C virus to infect hepatocytes (Ploss 2009), and their downregulation prevents cellular superinfection (Liu 2009).

The cellular distribution of occludin, and its interaction with ZO-1, are modulated by the differential phosphorylation of a number of occludin residues (Rao 2009; Feldman et al., 2005). PKC and the casein kinases 1 and 2 are the most prominent kinases involved in occludin phosphorylation (Dörfel et al., 2009; Andreeva et al., 2006, Smales et al., 2003; Cordenonsi et al., 1999); however, other kinases like p34/cyclin-B, the extracellular-signal-regulated-kinase (ERK), c-Yes, the Rho-associated protein kinase ROCK and the Ras-related GTPase Rab13 also phosphorylate occludin (Blasig et al., 2011).

Using two dimensional gel electrophoresis, two phosphorylated forms of occludin were originally identified, but cellular stimulation with vascular endothelial growth factor (VEGF) induced the appearance of three additional forms (Harhaj et al., 2006); by combining those observations with a theoretical prediction of phosphorylation sites, it was suggested that occludin was phosphorylated at the threonine^{168} (in the intracellular loop), the threonine^{404}, and the serines 408, 471 and 490 (Sundstrom et al., 2009). Further studies showed that the threonine^{404} was indeed phosphorylated by PKCη, along with its neighboring threonine^{403} (Suzuki. et al., 2009), the serine^{408} was shown to be phosphorylated by the casein kinase-II –CKII (Dörfel et al., 2009) and the c-Src dependent phosphorylation of the tyrosines 398 and 402 was also demonstrated (Elias et al., 2009).

The phosphorylation of the serine^{490} prevented the association of occludin and ZO-1, presumably by partially changing the surface charge on the occludin binding area of occludin (Sundstrom et al., 2009), phosphorylation of the tyrosines 398 and 402 drastically reduced the binding of occludin with ZO-1, and prevented occludin from reaching the plasma membrane (Elias et al., 2009). On the other hand, the inhibition of PKCη, and as a consequence, lack of phosphorylation of the threonines 403 and 404, induced disruption on the membranal localization of occludin and ZO-1, and promoted disruption on the barrier function of the TJ; furthermore, substitution of such threonines for alanine, prevented occludin from being incorporated in the TJ (Suzuki et al., 2009). In intact epithelia, occludin is highly phosphorylated in threonines and serines, while the tyrosines in its C-terminal domain are dephosphorylated; if on the contrary, those threonines and serines are dephosphorylated, and tyrosines phosphorylated, occludin delocalizes from the TJ. The protein-phosphatases PP1 and PP2A bind to the last 150 amino acids of occludin where they dephosphorylate respectively serines and threonines (Rao, 2009; Sheth et al., 2009; Seth et al., 2007).

1.3.2.3 Junctional adhesion molecules.

JAMs are members of the immunoglobulin protein superfamily, they are found not only in epithelial/endothelial cells, but also in leukocytes, and platelets. They are constituted by a single transmembranal domain, a short intracellular C-terminal tail, and a large extracellular domain with two Ig-like motifs. The family is comprised of four members: A, B, C and 4/L (4 in mouse, L in human). JAM-A and C are localized at the TJ, while JAM-B is expressed along the whole lateral membrane. The extracellular domains of JAM-A, B and C are needed for their *cis*-dimerization. JAMs are also involved in cell-adhesion by forming *trans*-interactions (homophilic or heterophilic) between themselves but also with integrins. Their expression at the TJ also contributes to their barrier function;

it was proposed that, by forming *trans*-homophilic dimers, JAM-A can regulate the TJ; however, the precise mechanisms of such regulation are not well defined. It has been suggested that JAMs could target other proteins to the TJ; the C-termini of JAM-A, B and C have PDZ binding motifs that allow them to bind different membrane-associated guanylate kinase homologous proteins (MAGUKs), i.e. ZO-1, MAGI-1, MUPP1, the serine protein kinase CASK/Lin2, and the cell polarity-related/G protein-coupled receptor Par3. (Shin et al., 2006)

1.3.3 PERIPHERAL PROTEINS

The transmembranal proteins of the TJ bind to the peripheral proteins associated to them. They allow the transmembranal proteins to acquire a proper organization in the cell membrane, link them to the cytoskeleton and can function as signaling transducers. So far, the most studied TJ peripheral proteins are MAGUKs, MAGUK-inverted proteins (MAGIs) and cingulin.

1.3.3.1 Membrane-associated guanylate kinase proteins

The MAGUK proteins are characterized by having one or more PDZ (PSD95/Dlg/ZO-1) domains, a Src homology 3 (SH3) domain and a non-catalytic guanylate kinase homology (GuK) domain (Gonzalez-Mariscal et al., 2000); their general architecture is shown in **Fig. 6**. Most MAGUK proteins work as scaffolding proteins and localize to cell-cell contacts. Their GuK domain has been related to protein-protein interactions. The SH3 and the GuK domains interact with each other and form a structural core that, together with a flexible hinge that connects both, constitute a functional SH3-hinge-GuK (SHG) unit, capable of binding other TJ molecules and second messengers (Lye et al., 2010; Müller, 2005; Schmidt et al., 2004).

There are three known types of zonula occludens proteins: ZO-1, ZO-2 and ZO-3. They play a key role in regulating the protein assembly at cell-cell contacts, clustering of receptors and ion channels, differentiation, and regulation of gene expression (*Schmidt et al., 2004*).

ZO-1 is localized at the TJ in epithelial and endothelial cells, but is also present in fibroblasts, astrocytes, and Schwann cells (Gonzalez-Mariscal et al., 2000); it has two nuclear localization signals,

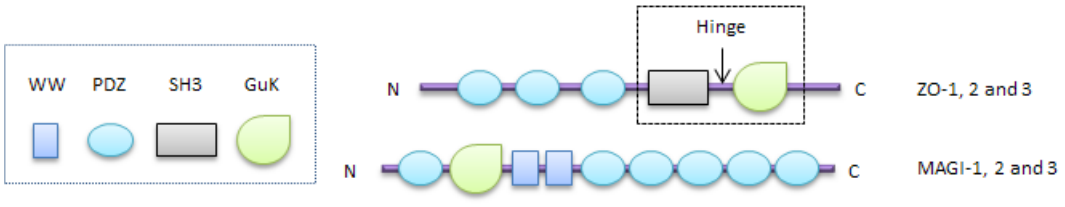

Fig. 6. Schematic representation of tight junction membrane-associated guanylate kinase (MAGUK) proteins. They are structured by several PDZ domains and a guanylate kinase domain. In ZO-1, 2 and 3, an SH3 domain forms a functional unit with the GuK domain; the hinge in between, forms a binding area for signaling molecules. Membrane associated guanylate kinase inverted (MAGI) proteins have several PDZ domains but lack the SH3 domain; however, they have two additional WW domains that bind proline rich domains in other proteins.

and a C-terminal region rich in proline residues. During epithelial maturation, ZO-1 localizes to the cell nuclei where it regulates cell proliferation by interacting with the Y-box transcription factor *ZO-1 associated nucleic acid-binding protein* (ZONAB) via its SHG unit (Balda et al., 2003).

ZO-2 and ZO-3 are also binding partners of ZO-1. ZO-2 has two nuclear localization signals in the first PDZ and the GuK domains. During epithelial maturation, ZO-2 localizes also to the cell nucleus where it interacts with the transcription factors Fos and Jun (that form the AP-1 early response transcription factor), CCAAT/enhancer binding proteins (C/EBPs), and the DNA-binding protein scaffold attachment factor-B (Betanzos et al., 2004, Jaramillo et al., 2004). All ZO proteins interact directly with the coiled-coil domain of occludin (Feldman et al., 2005), ZO-1 interacts with claudins via its first PDZ domain and interacts with itself via its second PDZ domain, and presumably via its SHG unit (Müller et al., 2005). In non-polarized cells, ZO-1 can also interact with proteins of the adherens junctions like E-cadherin and α-catenin, using a common binding site in the hinge region of the SHG unit; since this site is also shared with occludin, it was suggested that the ZO proteins formed a complex with the adherens junction proteins in cells where the TJ are still not formed, during polarization, however, they would separate and occludin and ZO-1 would bind and concentrate to the TJ.

Due to the functional relevance of the SHG unit of ZO-1, an attempt to identify its precise structure by X-ray crystallography was recently published (Lye et al., 2010); however due to the flexibility of the hinge region, it had to be deleted from the molecule so a proper crystallographic resolution could be achieved.

1.4 THE TIGHT JUNCTIONS OF THE BLOOD-BRAIN BARRIER UNDER PATHOLOGICAL CONDITIONS

The barrier properties of the brain capillary endothelial cells are established during the embryonic development, under the influence of the different tissues surrounding the sprouting vessels (Ikeda et al., 1996; Janzer and Raff, 1987). In adults, the endothelial barrier is dynamically regulated in response to changes in the environment, such as shifts in the oxygen pressure in blood or inflammation (Fischer et al., 2004; Ballab et al., 2004; del Zoppo and Mabuchi, 2003). Several pathological conditions like ischemia, diabetic microvascular disease, chronic pain, sepsis, and trauma, lead to an increase in the overall transendothelial permeability that can be causative of life threatening complications, like brain edema, or the influx of pro-inflammatory molecules, toxins or even bacteria from the bloodstream into the brain parenchyma. In many of these situations, different signaling cascades are triggered by inflammatory molecules and oxidative stress, leading to an upregulation of stress response factors like the transcription factor family NF-κβ, Heat-shock proteins (HSPs) and proapoptotic molecules.

The mechanisms by which the barrier properties are lost in neurovascular endothelium, under critical clinical conditions such as stroke, are still poorly understood. Claudins 1, 3, 5 and occludin are sensi-

tive to hypoxia, and the expression patterns of these proteins and MAGUKs changes drastically in the brain vascular endothelium upon hypoxia, trauma and inflammation: occludin is redistributed from the cell surface to intracellular compartments, ZO-2 translocates to the cell nucleus, ZO-1 is delocalized from the plasma membrane and is accumulated in the cytosol, while claudins 3 and 5 are overexpressed (Raymond et al., 2007; Brooks et al., 2005; Huber et al., 2002; Mark and Davis, 2002). As a consequence of this molecular rearrangement, the permeability of the brain capillaries is increased, and brain edema, a life threatening condition, ensues.

1.4.1 HYPOXIA AND CELLULAR NADH CONTENT

The term hypoxia indicates a reduction on the cellular availability of oxygen produced either by the reduccion of the oxygen supply, like in stroke, or due to an excess in oxygen consumption, as induced, for example, during sepsis.

The main energy production in the cells comes from respiration. In this process, energy, in the form of ATP, is generated during oxidative phosphorylation in the mitochondria. Oxidative glycolysis is the first step in the respiratory system and is the only one that occurs in the cytosol, generating pyruvate and 2 molecules of NADH, and consuming 2 molecules of NAD^+. The cytosolic NADH, via the malate/oxaloacetate shuttle, enters the mitochondria, where the rest of the cellular respiration process occurs. There, pyruvate is transformed into acetyl-coenzyme A (acetyl-CoA) generating another NADH molecule. The acetyl-CoA is then incorporated into the Krebs cycle, converting three moles of NAD^+ into three moles of NADH (plus one mole of $FADH_2$) per mole of acetyl-CoA. Finally the NADH and $FADH_2$ are incorporated into the electron transport chain (respiratory chain) where NAD^+ is regenerated; this creates a proton gradient across the internal mitochondrial membrane that is used in a further step to generate ATP from ADP by the ATP synthase.

The respiratory chain is formed by several coupled oxidoreductases, and its final redox reaction can be summarized as $NADH + O_2 \rightarrow NAD^+ + H_2O$, where NADH is the electron donor and the oxygen the final electron acceptor. Thus, the regeneration of NAD^+ and the consequent decrease of the NADH pool depend on the cellular availability of oxygen. Under hypoxia/anoxia, the reduced oxygen concentration impairs the efficiency of the respiratory chain, and induces mitochondrial dysfunction; as a result, the $NADH/NAD^+$ equilibrium is impaired and the pyruvate is transformed into lactate to produce a reduced amount of energy, but inducing cellular acidosis. This condition generates a drastic cellular redox imbalance, and the concomitant NADH increase can be measured to estimate the extent of metabolic/redox imbalance (Rex, et al., 2001; Cordeiro, et al., 1995).

NADH can be measured by detecting its fluorescence in cells or tissues; it has a spectral peak of light absorbance at 340 nm, and a characteristic emission peak at 460 nm. In contrast, NAD^+ has an absorbance peak at 260 nm, hardly absorbs energy at 340 nm and exhibits nil fluorescence at 460 nm (Kay et al., 2008, Kasimova et al., 2006, Bruce et al., 2004, Bose et al., 2003),thus, NADH can be measured in living cells using biphotonic confocal microscopy.

1.4.2 Behavior of occludin in response to the cellular redox conditions

The activity of NAD(P)H oxidase is related to the disrupted expression of occludin and ZO-1 in murine epithelial cells (Choi et al., 2010), and there is evidence implicating NAD(P)H as an important source of reactive oxygen species (Harrison and Gongora, 2009). The NAD(P)H oxidase generates superoxide from either NADPH or NADH, and its excessive activation is related to different inflammatory diseases (El-Benna et al., 2009).

The effects of reactive oxygen species on occludin are subject of intense study, however, their mechanisms are still poorly understood. Superoxide and hydrogen peroxide are among the most important species involved in the redox modulation of occludin (Blasig et al., 2011); superoxide redistributes occludin via tyrosine-phosphorylation in a process that putatively involves the dissociation of occludin from the cytoskeleton (Krizbai et al., 2005; Rao et al., 2002). Hydrogen peroxide promotes serine-phosphorylation and threonine-dephosphorylation of occludin, inducing its cellular redistribution, and decreasing the barrier function of the TJ; furthermore, the phosphatase PP2A has been shown to increase its association with occludin after stimulation with hydrogen peroxide (Sheth et al., 2009).

1.5 Hypothesis and objectives of this work

There is strong evidence indicating that the TJ molecules oligomerize (Westphal et al., 2010; Krause et al., 2008; McCaffrey et al., 2007; Blasig et al., 2006); however, little is known about the structural determinants and the biological relevance of such oligomerization. On the other hand, cumulative evidence shows that occludin plays a pivotal role in regulating the formation and maintenance of the TJ (Blasig et al., 2010); furthermore, occludin also oligomerizes, and inflammation leads to changes in the oligomerization status of occludin (McCaffrey et al., 2008).

It was suggested that occludin could oligomerize by forming one or more disulfide bridges, and that possibly, if disulfide bridges were involved, they could be disrupted during inflammation (McCaffrey 2007 and 2009); this possibility has not been yet explored, as it is its physiological significance. The amino acid sequence of occludin contains seven cysteines, in human, at positions 76, 82, 148, 216, 237, 409 and 500, and it is unclear which of them could be involved in the oligomerization. Nevertheless, the C-terminal domain of occludin is required for its dimerization (Chen et al., 2009), and two cysteines are present in this region (**Fig. 7**).

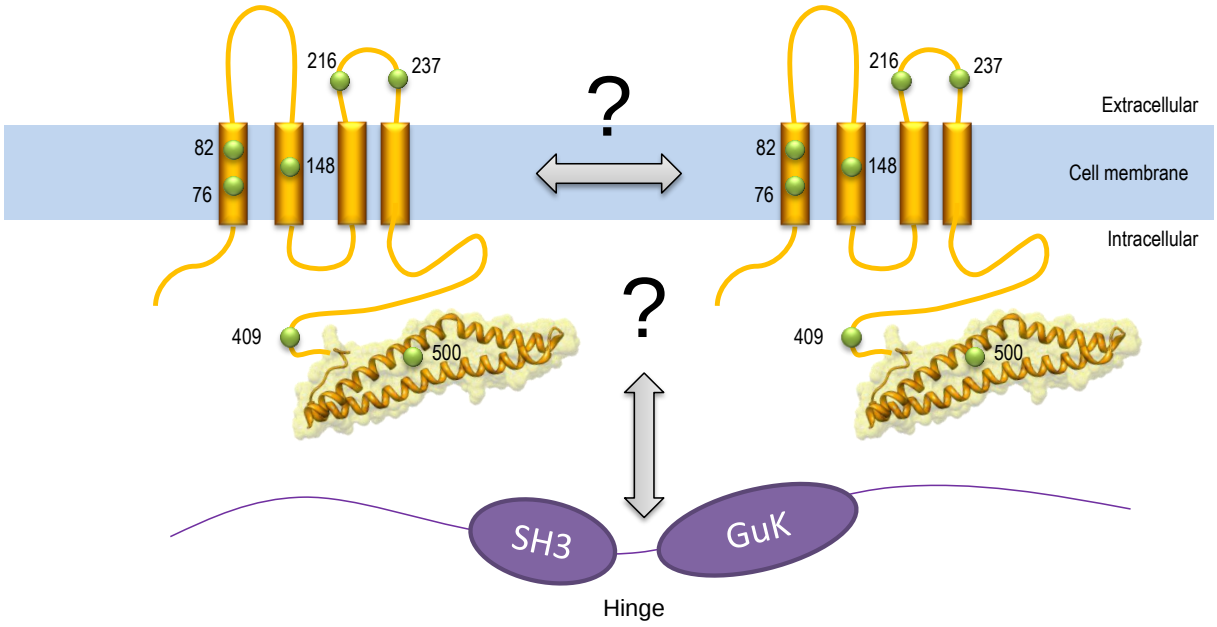

Fig. 7. The amino acid sequence of occludin contains seven conserved cysteines. The position of the cysteines in human occludin is marked with green circles. It is unclear whether the cysteines in occludin would have an influence in the dimerization of the molecule. Furthermore, it is not known if the dimerization of occludin has an effect on its subcellular localization, or if its dimerization has an influence on its association with its binding partner ZO-1.

As basis for this work, it was hypothesized that the dimerization of occludin would be dependent on one or more disulfide bridges; in particular, formed by the cysteines located in its C-terminal domain; in these conditions, redox changes in the cytosol, like those caused by hypoxia and inflammation would prevent occludin from forming a disulfide bridge and consequently, would hinder its dimerization. These changes would be then reflected by changes in the cellular expression pattern of occludin and its interaction with ZO-1.

To explore this hypothesis, it had to be determined, **(I)** whether the dimerization of occludin is redox sensitive, and if so, **(II)** explore whether loss of the dimeric form, under reducing conditions, correlates with differences in the expression pattern of occludin in cells subjected to redox-challenging conditions such as hypoxia or inflammation. This would be a strong indication of the involvement of one or more disulfide bridges; thus in a further step, it had to be identified **(III)** whether both, or only one of the C-terminally located cysteines are needed for the dimerization of occludin. Then, it was required to assess whether the dimerization of occludin, mediated by a disulfide-bridge, had any biological effect, thus, **(IV)** the behavior of occludin and its ability to interact with ZO-1 had to be explored under redox-challenging conditions.

Occludin and ZO-1 were studied in a cellular model where no other TJ molecules could potentially interact with them, leading to unspecific results. The TJ-free HEK-293 cells were used as an

expression system. Fluorescently labeled (CFP and YFP) occludin and ZO-1 were expressed in these cells, either alone, or together. Confocal microscopy allowed the observation of occludin and ZO-1 in living cells. Cellular redox insult was performed by culturing cells in hypoxia, or stimulating them with inflammatory cytokines (IFN-γ and TNF-α). The dimerization of occludin was studied by gel electrophoresis, and a series of occludin mutants were generated to identify the cysteines involved in its dimerization.

2 MATERIAL AND METHODS

2.1 CELL CULTURE

2.1.1 GENERAL GROWING CONDITIONS

Human embryonic kidney (HEK-293) cells, and Madin Darbey canine kidney (MDCK-II) cells were cultured in tissue culture treated flasks using Gluta-MAX Dulbecco's modified eagle medium (DMEM), enriched with 10% fetal calf serum and 10% penicillin/streptomycin (growing medium). The cells were cultured in a 10% CO_2 standard atmosphere at 37 °C in a cell incubator. Regardless of the confluency conditions, growing medium was exchanged each other day, with a single room-temperature, Ca^{++}/Mg^{++} free, phosphate-buffered saline (PBS) wash. Previous to usage, growing medium was warmed up to 37 °C in a water bath. For 25 cm^2 flasks, 5 ml of medium was used, 10 ml for 75 cm^2, and 20 ml for 175 cm^2 flasks. When confluent, all cells were washed twice with Ca^{++}/Mg^{++} free-PBS and trypsinized for 5 min at 37 °C with 0.05% trypsin/0.02% EDTA, using 100 µl of trypsin solution per 25cm^2 of cells. After trypsination, cells were reseeded; the standard seeding density was approximately 40 x 10^3 cells / cm^2; and confluent flasks produced a density of 60 x 10^3 to 80 x 10^3 cells/cm^2. For microscopical experiments, cells were seeded directly on glass coverslips; in order to facilitate cell attachment, the coverslips were bathed in a solution of poly-L-lysine (PLL) diluted 1:4 in mili-Q water and kept at 37 °C for 1 to 2 h, afterwards, the PLL was removed and the coverslips washed twice with Ca^{++}/Mg^{++} free PBS. When not used for experiments, cells were splitted at a 1:3 ratio (approximately 20 x 10^3 cells/cm^2). Each trypsination – reseeding cycle was counted as one "passage". The first passage immediately after introducing the cells to culture (i.e., thawing them for the first time, or when just received from another laboratory) counted as passage one; all experiments were performed in cells between passages 7 and 23, above passage 23 the cells showed irregular growing rates and were therefore not used for experiments. When cytokine stimulation was required, TNF-α or IFN-γ was added to the growing medium at a concentration of 200 ng/ml, and incubated for 3 h, cells were analyzed immediately after without exchanging growing medium.

2.1.2 HYPOXIC CONDITIONS

For hypoxia experiments, the cells were previously incubated until confluency in a normal incubator at 37 °C and 10% of CO_2. Hereupon, they were transferred to an anaerobic workstation, and incubated for 3 h at 37 °C. Chemical catalyzers maintained the oxygen concentration in the anaerobic workstation below detectable levels. When the cells were needed for microscopy, the wells where these cells were cultured were sealed with parafilm inside of the workstation.

2.1.3 CELL STORAGE, FREEZING AND THAWING

When not in use, cells were cryogenically stored at 77–123 °K with liquid nitrogen as cooling agent and dimethyl sulfoxide (DMSO) as preservative. Previous to storage, they were washed twice in PBS, tripsinized, recovered with a Pasteur pipette into preservation medium (5% DMSO in fetal calf serum),

and transferred into a cryogenic vial. The vial was stored in an isopropanol-bathed cryo-freezing container, chilled down and kept at -76 °C for 24 to 74 h; then the vial was transferred to a liquid nitrogen tank. Isopropanol assured a steady temperature decrease of 1 °C/min.

During storage, cells were kept in a cryogenic container serviced by an automatic liquid-nitrogen refill system. When needed, they were thawed at room temperature, and seeded directly into a flask containing growing medium at 37 °C, after 12 h, once the cells had attached, the growing medium was exchanged, and no intermediate centrifugation steps were required, reducing the handling stress on the cells. Less than 10% of the cell population was lost after thawing and reseeding.

2.1.4 TRANSFECTION

HEK-293 cells were seeded the night before at 75% of confluency, so they reached more than 80% of confluency on the day of transfection, the cells were washed three times with Ca^{++}/Mg^{++} free-PBS, and the growing medium was substituted with uncomplemented DMEM without antibiotics (plating medium). For transfection, Lipofectamine 2000 was mixed with the cDNA, according to the manufacturer's instructions. Briefly, for a single 2 cm^2 well with 500 µl of of plating medium (24 well plate), 800 ng of DNA were mixed with 50 µl of the dilution reagent Optimem, simultaneously, 2 µl of Lipofectamine 2000 were diluted in another 50 µl of Optimem. After a 5 min incubation, both, Lipofectamine 2000 and the DNA, were mixed and incubated at room temperature for 30 min, so the DNA-containing Lipofectamine complexes could form. Afterwards, the complexes were added by floating drops on the surface of the plating medium. Cells were transferred to the incubator after transfection. Plating medium was exchanged for normal growing medium after 24 h.

2.1.5 CLONAL SELECTION

For the establishment of stable cell lines, HEK-293 cells were seeded in 10 cm^2 wells (6 well plate) and transfected with the cDNA encoding for the desired fluorescently tagged protein, inserted via BamH-I and Sal-I in the multicloning site of pEYFP-C1. These vectors contained the gentamicin resistance gene. Thus, 72 h after transfection, the cellular expression of the protein was assessed by confocal microscopy, and the cells reseeded in a 60 cm^2 petri dish. At this point, geneticin (G418, a gentamicin analogue) was added to the growing medium, at a concentration of 50 mg/ml; the cells were cultured in this condition for two weeks (medium was exchanged each other day); only those cells expressing the gene of interest (i.e. the fluorescently labeled protein with the resistance gentamicin gene) survived the treatment and formed small antibiotic-resistant colonies.

After the initial selection, the cells were slightly detached by brief/mild trypsination and recovered with a 10 µL pipet as follows: cells were washed twice in Ca^{++}/Mg^{++} free-PBS (each was lasted 1 min), after the last wash, most of the PBS was removed and only a small amount was left, enough to cover the cells; 500 µl (for a 60 cm^2 dish) of a 0.05% trypsin/0.02% EDTA solution were added afterwards. After one minute, and under direct microscopical (phase contrast) observation, the cells from individual colonies were retrieved by pipetting and deposited in 2 cm^2 wells (24 well plates). Two wells, one of

them containing a small glass coverslip, were seeded per colony. Hereafter, geneticin was always added to the growing medium.

One week after, the cells were observed under confocal microscopy and the cells that expressed the fluorescent protein in detectable amounts, localized it as desired, and showed low intracellular aggregates, were counted, subcultured in 0.5 cm^2 wells (96 well plate) at a calculated density of 0.5 to 1.5 cells per well, grown for five days and reseeded into 2 cm^2 wells for a second round of microscopical evaluation. The best cells were counted again and reseeded for a second time into 0.5 cm^2 wells, at a calculated density of 0.5 to 1.5 cells per well, and grown until confluency. Each well received a particular identifier (e.g. clone 1, 2, 3.) and was subcultured again into 2 cm^2 wells for a final microscopical evaluation, this passage was arbitrarily considered as passage "1" for all the clones. The best clones were selected, passed into 10 cm^2 wells, grown and transferred to 25 cm^2 flasks; upon confluency, they were collected and stored in liquid nitrogen until use (**Fig. 8**).

2.2 Cell imaging.

2.2.1 Laser Scanning Confocal Microscopy

Live cell imaging was performed on HEK-293 cells expressing YFP or CFP tagged proteins; when needed, the cell membranes were stained with a 0.5% trypan blue solution (75 µl per 500 µl of cell medium). For all observations, the cells were cultured in poly-L-lysine covered Nunc 4-well borosilicate glass bottom coverslips (thickness 1.0). Analysis was performed in a Zeiss LSM 510 laser scanning confocal microscope system equipped with Helium/Neon and Argon laser lines, a Titanium-Sapphire, near-Infrared, multiphotonic laser, and a spectral detector. All measurements were performed using a Plan-Apochromat[1] 63X oil immersion objective with a numerical aperture of 1.4. For detection purposes, YFP was excited with the Argon laser line at 488 nm (50% of power and 1-7% of transmission), but for functional analysis, including fluorescence resonance energy transfer, the fluorophore was excited with the same Argon line at 514 nm (50% of power and 1-5% of transmission), in both cases, the fluorescence emission was detected spectrally at 516-554 nm. Excitation of CFP was performed with the Argon line at 458 nm (50% of power and 5-21% of transmission), and its fluorescence detected spectrally at 468-554 nm. Trypan blue detection was performed by exciting at 633 nm with the Helium/Neon laser line, and detecting at 644-719 nm. Cellular NADH was detected by using the Titanium-Sapphire infrared laser tuned and locked at 810 nm, and its fluorescence detected spectrally at 436 – 475 nm. In all cases scanning was unidirectional, with a speed of ~2.56 µs per pixel; the detection was averaged from 8 sequential linear scans to filter out background noise. The recorded images were stored in 12-bit format in Zeiss-LSM proprietary format.

[1] *Spherically and chromatically corrected for red, blue, and green wavelengths, as well as field curvature*

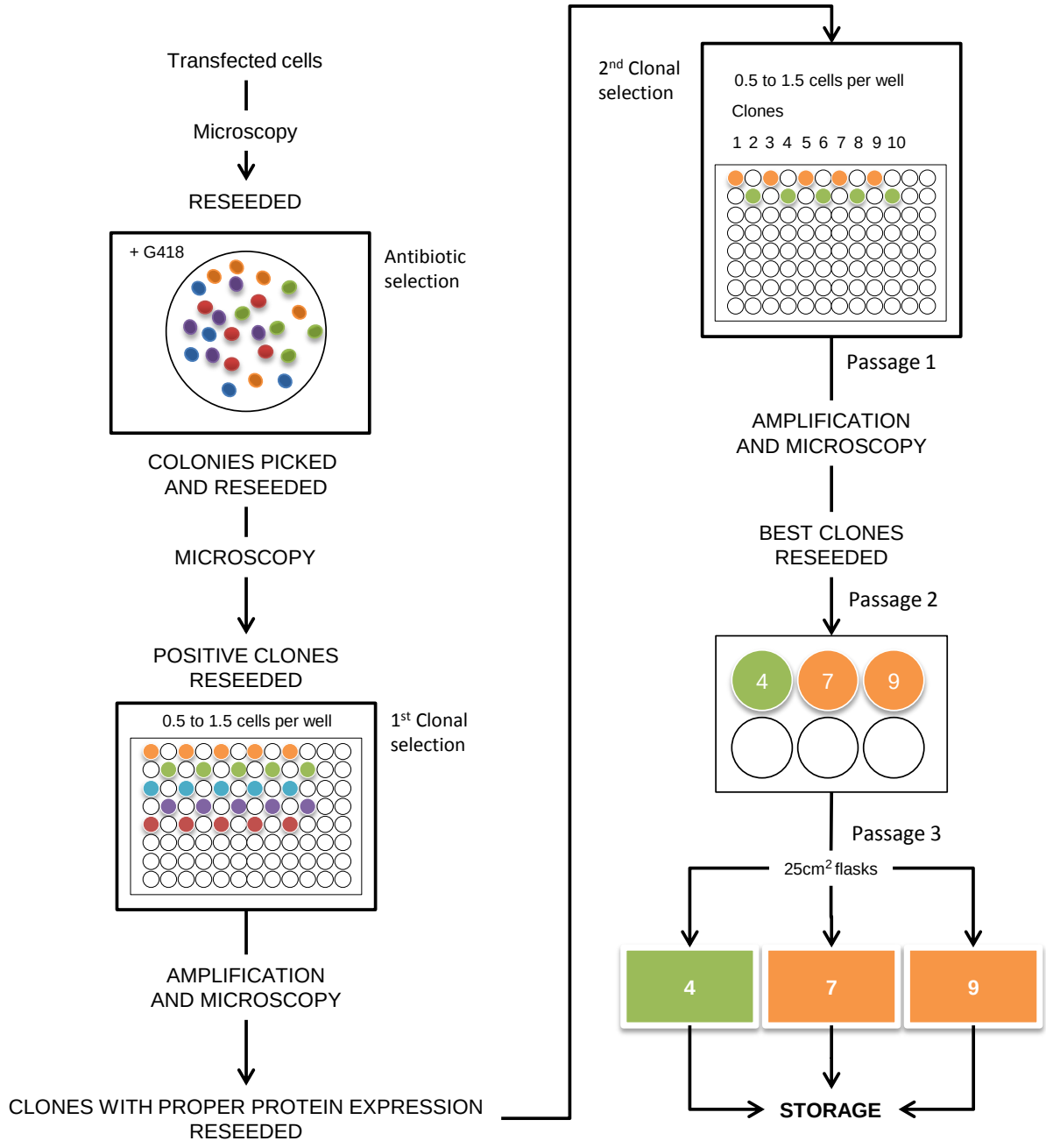

Fig. 8. Simplified pipeline for the establishment of stable cell lines. After transfection, cells were selected with G418. Two seeding steps, at a density of 0.5 – 1.5 cells/well, and consecutive confocal microscopy analysis, assured a single parental cell for each definitive clone.

The signal acquisition was performed considering the Nyquist criterion (Matsumoto 2002; Shannon 1948; Nyquist 1928) the pixel size and zoom factors were calculated according to the following equations:

(1) $Pixel\ size = \frac{SC}{Pixels\ per\ line * Zoom\ factor * Magnification}$, and

(2) $Zoom\ factor = \frac{3.92 * NA * SC}{Pixels\ per\ line * Magnification * \lambda}$,

where NA represents the numerical aperture of the objective lens, SC is the system correction constant specific for the Zeiss LSM 510 system (8940 µm), and λ is the wavelength of the emission signal (in µm). Pixels per line refer to the vertical pixel resolution of the resulting image (most of the images were recorded either in 720p-HD or 1080p-HD formats). The pinhole aperture was optimized by defining the size of 1 Airy unit (Matsumoto 2002; Airy 1835) for the Zeiss LSM-510 confocal system, according to the following equation:

(3) $AU = \frac{0.51 * \lambda * Magnification * 8.8}{NA}$,

where AU is the size of an Airy unit, NA is the numerical aperture of the objective lens, and λ represents the wavelength of the emission signal (in µm).

Tridimensional image acquisition was performed by scanning the samples at sequentially increasing depths, each scan produced one image, and all the images were then superimposed to create z-stacks. The z-stacks were then transformed into orthogonal representations. In order to satisfy the Nyquist criterion, the z-step (separation in µm between each image in the z-stack) was calculated as:

(4) $z\ step = \frac{DOF}{2}$, where DOF stands for depth of field and was calculated as:

(5) $DOF = \frac{\lambda}{2 * NA^2}$,

where λ represents the wavelength (in µm) of the emitted signal and NA is the numerical aperture of the objective lens.

2.2.2 Fluorescence Resonance Energy Transfer

FRET analysis takes advantage of the radiative and coulombic transfer of energy that occurs between an energy donor (i.e. CFP), and an acceptor (i.e. YFP) fluorophores (Andrews 1989). Since the amount of transferred energy (FRET efficiency) is proportional to the sixth power of the distance that separates the fluorophores, FRET has been used successfully to demonstrate that two proteins are in such close proximity that a direct association between the two can be presumed

The most efficient way to show FRET when using CFP/YFP fluorophore pairs is to perform acceptor photobleaching (apFRET). In this technique, YFP is bleached up to a point when it is not able to accept any more energy, and the fluorescence intensity of CFP is compared before and after the bleaching process (**Fig. 9**).

In apFRET, if energy transfer existed, upon excitation, the amount of the CFP-emitted energy that was being transfered to YFP will not find a suitable acceptor, and will be emitted as light, as a result, the CFP fluorescence intensity is increased upon YFP bleaching (Bastiaens and Jovin, 1996; Wouters et al., 1998). The advantage of this approach is that each cell serves as its own negative control, and thus is regarded as one of the most accurate techniques for measuring FRET without needing a

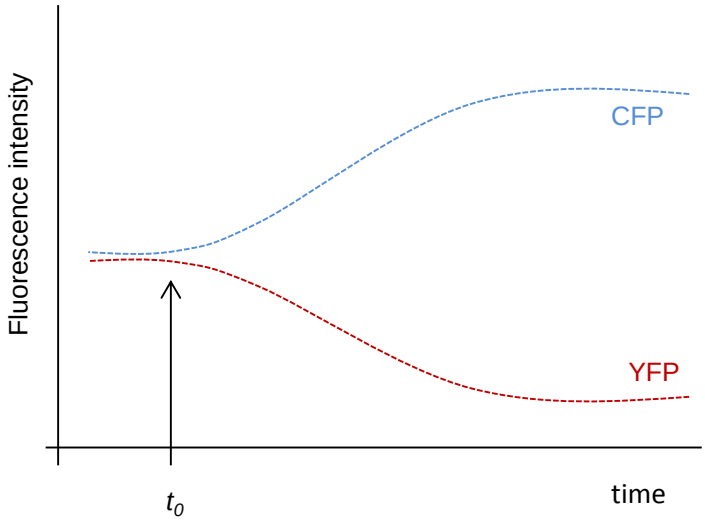

Fig. 9. FRET by acceptor photobleaching in CFP / YFP pairs. The fluorescence intensity of CFP (donor) increases during bleaching (inactivation) of YFP (acceptor). t_0 represents the bleaching starting time.

complex set of images to be used as control references (Chen and Periasamy 2006). One of its drawbacks is that the acceptor is considered “irreversibly” bleached (Day et al., 2001) and additional measurements cannot be repeated in the same cell.

When YFP is bleached, the CFP molecules are also bleached; inducing an unwanted partial loss in the CFP fluorescence, a phenomenon that results in underestimation of the FRET efficiencies (Chen et al., 2007). When working with molecules that are expressed in high amounts, the CFP fluorescence will still be high enough to give a good signal to noise ratio; however, that is not the case for low-abundant proteins, or fluorophores that show low emission yields. Increasing the laser excitation intensity to increase the CFP fluorescence often leads to cellular photodamage and does not increase the fluorescence intensity of CFP above certain threshold. In the confocal system used in this work, increasing the laser intensity transmission above 9% (with 50% of its basal power) resulted in a very low increase in the CFP emission, considerably produced CFP photobleaching and in some cases induced cellular photodamage.

Acceptor photobleaching was the method of choice in this work. To counter for the underestimation of the CFP fluorescence during YFP bleaching, a modified approach was sought, thus the quantum corrected-lambda-FRET (qλ-FRET) technique was developed by incorporating the advantages of three different FRET techniques into a single method, while avoiding most of their inherent disadvantages: for that, it used spectral detection of CFP and YFP to provide the best possible identification of the YFP and CFP signals, the mathematical analysis of in-vitro spectrofluorometric FRET was applied to the confocal microscopy measurements, and YFP was only partially bleached so a change in the CFP intensity could be observed upon small reduction of the YFP fluorescence.

Conventionally, the CFP and YFP signals are measured several times before, during, and after the bleaching process, and if protein-protein interaction occurs, the intensity of CFP is expected to increase while the YFP intensity decreases; this continuous measuring is time consuming and gives enough time for the structure being recorded to move before the process is finished, leading to false FRET appreciations. In view of that, fast detection algorithms are traditionally used and small regions of interests are selected, often with suboptimal (non Nyquist) resolution. In qλ-FRET, the sample is scanned once at the beginning, bleached a single time (with multiple iterations) and rescanned once at the end. Besides increasing the scanning speed, whole cells or even whole fields can be recorded at once.

For FRET experiments, YFP/CFP pairs for the proteins of interest were expressed in HEK-293 cells cultured on poly-L-lysine covered glass-bottom chambers. The chambers were directly observed under the confocal microscope. The YFP and CFP excitation, as well as their detection was performed as described in the former chapter (2.2.1 - page 21). Spectral acquisition of YFP and CFP was performed to identify their respective fluorescence intensity peaks. Excitation of CFP produced two intensity peaks at 468 and 500 nm, and the spectral area in the range of 468 nm to 500 nm was used to integrate the CFP signal. Excitation of YFP produced an intensity peak at 532 nm; when FRET occurred, after the excitation of CFP with a 458 nm laser, the energy absorbed by YFP produces an additional peak at 532 nm in the CFP spectrum; the 458 nm excitation of CFP cross-excited YFP (due to the partial juxtaposition of the YFP excitation spectrum with the CFP excitation spectrum), and as a result, the spectral peak intensity at 532 nm is slightly reinforced. Bleaching of YFP dramatically decreased the 532 nm peak by reducing the availability of YFP to accept energy either directly from CFP or due to cross-excitation with the 458 nm laser. If FRET existed, the reduction on the YFP peak at 532 nm was paired with an increase in the overall CFP intensity. The general principle of qλ-FRET is shown in **Fig. 10**.

The procedure itself consisted of four steps: 1) a fast scan was performed to detect colocalization of YFP and CFP, 2) CFP was excited once and the emission spectrum recorded in the range of 458 – 544 nm (λ-scan with 8 simultaneous detection channels), 3) The YFP signal was partially bleached, exciting a whole microscopic field with a single pass of ten iterations with 100% of the laser intensity with a speed of ~2.6 µs per pixel. 4) CFP was excited once more and the emission spectrum recorded again in the range of 458 – 544 nm. The process was repeated in a minimum of ten fields per well. The corrected FRET efficiency (E_c) was then calculated as follows:

(6) $$E_c = \frac{\left(\frac{\int m_i - \int m_0}{\int m_i}\right)}{\left(\frac{\int n_0 - \int n_i}{\int n_0}\right)},$$

where $\int m_0$, $\int m_1$, $\int n_0$ and $\int n_1$ respectively correspond to the CFP intensity before bleaching of YFP, the CFP intensity after bleaching, the YFP intensity before bleaching, and the YFP intensity after bleaching (Fig. 10). This formula is equivalent to that used by others (Roy, et al., 2008; Ha, et al., 1999) to calculate corrected energy transfer in single molecule FRET, and intrinsically considers the correction γ factor (quantum factor - the ratio of intensity change of CFP vs intensity change of YFP) of single molecule FRET measurements. Calculation of the FRET efficiencies using the equation (6) or that of single molecule FRET produced equal results.

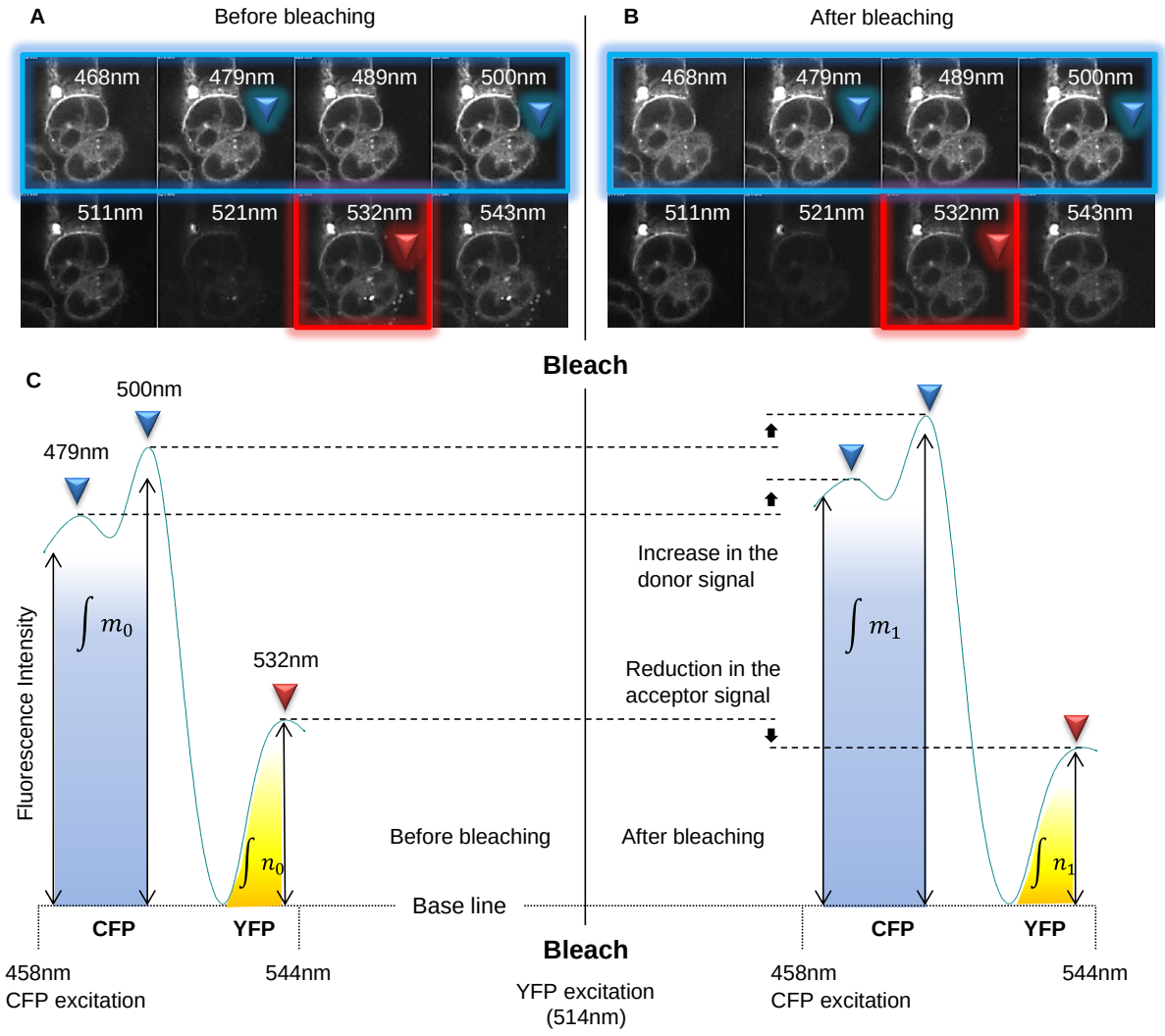

Fig. 10. General principle of quantum corrected, lambda scanned (qλ) FRET.

A and B) The composed image shows the lambda stacks of the same field acquired before (left) and after (right) partial YFP bleaching.

C) The data obtained from the images is converted into a spectral graph where the CFP and YFP intensity peaks can be identified (blue and red triangles respectively). The intensity difference of the three peaks, before and after photobleaching of YFP is used to calculate the energy transfer. $\int \mathbf{m_0}$, $\int \boldsymbol{m_1}$, $\int \boldsymbol{n_0}$ **and** $\int \boldsymbol{n_1}$ correspond to the integrated CFP and YFP intensities before and after bleaching (detailed calculations are given in the text)

The values for the change in YFP intensity after bleaching were obtained by reconstructing the real YFP spectrum (as when excited with a 514 nm laser and detected at 532 nm) from the YFP signal detected by exciting with a 458 nm laser and detected at 532 nm. For such purposes, a cross-excitation table for YFP was generated (measuring YFP-Occludin expressed alone in HEK-293 cells): The 532 nm YFP peak was measured by exciting YFP separately with the 515 and 458 nm lasers, before and after bleaching. The data was fitted with linear regression (R^2 = 0.8084) and the following function was obtained:

(7) a = 20.051 b – 18.838, where, a is the ratio of pre to post-bleached YFP signal in the real YFP spectrum, and b is the ratio of the pre to post-bleached YFP signal detected by cross-excitation.

The ratio of the non-bleached YFP peak at 532 nm detected by exciting at 458 vs 514 nm was also calculated (YFP-peak factor). The YFP-peak factors and b *-from equation (7)-* were linearly fitted (R^2=0.8423) and a second function was generated:

(8) c = 36.372 b – 35.458, where *c* is the YFP-peak factor.

Then, the values for $\int n_0$ and $\int n_i$ were obtained as:

(9) $\int n_0 = {}_C\mathrm{YFP}_0 \bullet c$, where ${}_C\mathrm{YFP}_0$ is the cross-excited YFP intensity at 532 nm before bleaching and

(10) $\int n_i = \frac{\int n_0}{a}$

The values for a and c were compared and correlated linearly (R^2=0.9815). As a negative control, the FRET efficiency between the corticotrophin releasing factor receptor-1 YFP and claudin 5-CFP was measured. HEK cells do not normally express the corticotrophin releasing factor receptor (Blasig et al., 2006; Heinrich et al., 1998). To ensure the reproducibility of the technique, the FRET efficiency between claudin-5 CFP and claudin-5 YFP (a known FRET pair) was used as a positive control. The FRET values for the positive control, measured by qλ-FRET and conventional apFRET (Blasig et al., 2006; Piontek et al., 2008) correlated linearly (R^2=0.9287). The negative controls always produced negative values, when compared by both techniques, and the data of both correlated also linearly (R^2=0.9999) (**Fig. 11**).

Measurements were always performed whenever both fluorophores were simultaneously found in the plasma membrane for membranal proteins, regardless if they were located at cell-cell contacts or not. In each scanned field, 20 circular regions of interest (ROIs, 5 pixels in diameter) were traced, and their FRET efficiencies averaged. The position of the ROIs was randomly selected, for as long as both YFP and CFP signals were colocalizing in the same spot; the number of cells measured per field varied ranged from three to five. The process was repeated at least in 10 fields per sample and a minimum of

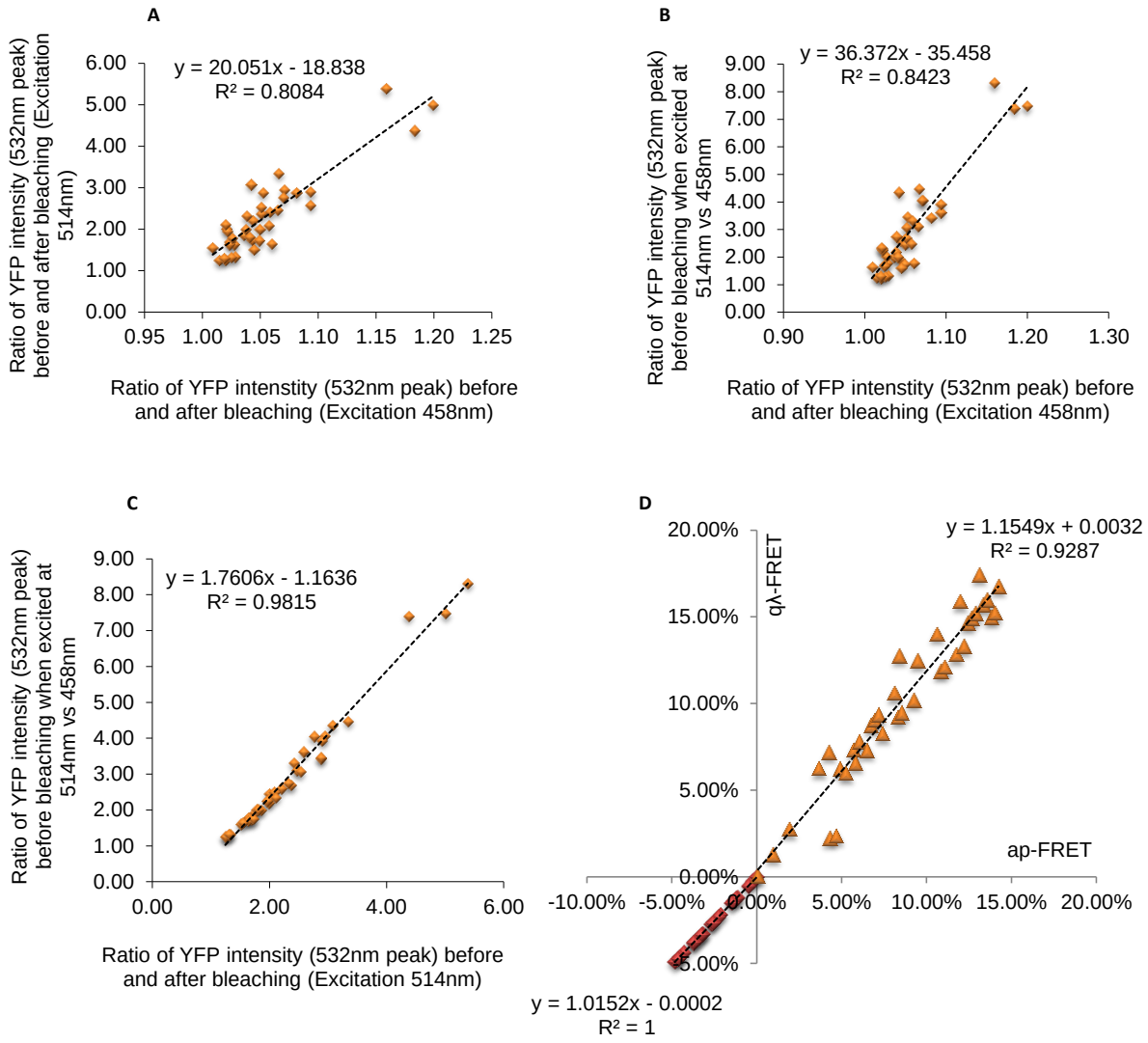

Fig. 11. Regression analysis of the parameters used to reconstruct the true YFP signal during qL-FRET.

A and B) Show the correlation of the data used to generate the equations **(7)** and **(8)** respectively

C) Shows the correlation between the variables *a* and *c* (obtained by solving the equations **(7)** and **(8)** respectively - see text).

D) Shows the correlation of FRET efficiencies for positive (orange triangles- Claudin-5 CFP vs Claudin-5 YFP) and negative (red squares Claudin-5 YFP vs Corticotropin releasing factor receptor-1 YFP) controls. The correlation is higher than 90% for the positive and 99.99% for the negative control.

4 experimental repetitions were performed. If the tested proteins were not in the plasma membrane (visualized by trypan blue staining) and FRET measurements were necessary, a similar number of ROIs per field was positioned in the cytosol of the cells (excluding the cell nuclei) in a random pattern wherever CFP and YFP colocalized.

2.2.3 FREEZE-FRACTURE ELECTRON MICROSCOPY

Cells expressing ZO-1 and occludin were grown on 6-well chambers; the protein expression was assessed by conventional fluorescence microscopy (non-confocal) and upon confluency the cells were quick-frozen in liquid N_2, immediately after, they were fixed with phosphate buffered glutaraldehyde solution (2.5% glutaraldehyde in Ca^{++}/Mg^{++} free PBS) for 2 h, afterwards, the fixed cells were washed with Ca^{++}/Mg^{++} free PBS and conserving glutaraldehyde buffer (0.4% glutaraldehyde in Ca^{++}/Mg^{++} free PBS) was added. Hereupon, the fixed cells were transferred to the Institute for Clinical Physiology at the Charité – Campus Benjamin Franklin (in cooperation with Dr. Susanne Krug) where they were fractured and analyzed by electron microscopy.

2.3 MOLECULAR BIOLOGY

2.3.1 DNA PROPAGATION

For propagation, DNA vectors were transformed into *E. coli* (BL-29E or DH5α). Transformation was performed in electroporation cuvettes by adding 1 µl of DNA (100 ng/µl in water) to 50 µl of bacterial suspension, and applying a single multi-pulsed current discharge of 2400 V. 1 ml of LB medium (0.5% yeast extract, 1% peptone from casein, 85 mM NaCl), without antibiotics, and warmed up to 37 °C, was added immediately after to the cuvette, then it was mixed with the transformed bacteria and retrieved into 1.5 ml Eppendorf tubes. The bacterial suspension was then incubated for 2 h at 37 °C while shaked at 300 rpm, then pelleted by centrifugation at 956xG for 2 minutes at room temperature, and resuspended in 50 µl of warm LB medium. The whole bacterial suspension was then homogenously spread on the surface of 10 cm^2 Petri dishes containing agar complemented with the antibiotic needed for clonal selection (50 mg/ml of kanamycin or 100 mg/ml of ampicillin). The dishes were stored overnight at 37 °C in a bacterial incubator and retrieved the next morning. Colonies were picked up by puncturing and pipetting into a sterile 1000 µl tip using a Gilson pipette; in this way, a small cylinder of agar, along with a thin layer of bacteria were collected into the tip. The tip was then washed inside a 15 ml Falcon tube containing 5 ml of LB medium with selective antibiotic (50 mg/ml of kanamycin or 100 mg/ml of ampicillin), and the presence of the agar cylinder into the tube was confirmed visually. If the cylinder was not deployed after repeated washing, the whole tip was left inside the tube. The bacteria-containing Falcon tubes were transferred to an orbital shaker, and incubated for 16 h at 37 °C at 300 rpm. This was considered the primary bacterial culture; from here, 500 µl were taken into a 1.5 ml Eppendorf tube and mixed with 500 µl of glycerol (80%); this glycerol stock was stored at -76 °C. When directly needed, either for DNA amplification and purification, or for polymerase-chain reaction screening, a subsequent subculture was generated from the primary culture, by transferring 100 µL of bacterial suspension into 25 mL of antibiotic-containing LB medium.

2.3.2 Amplification and purification of DNA

When required, glycerol stocks were scrapped with a 1000 µl Eppendorf tip; the obtained samples were diluted into 25 µl of warm (37 °C) LB medium (containing kanamycin or ampicillin) and shaked overnight at 300 rpm (37 °C). The bacterial suspension was centrifuged once at 1592xG for 60 min, and the pellets either frozen (or stored up to three weeks) or immediately processed as follows:

The bacterial pellets were resuspended in 1200 - 1800 µl of water and aliquoted in 600 µl samples in 1.5 ml Eppendorf tubes. Using a plasmid mini-prep kit (Zippy), each sample was incubated with 100 µl of lysis buffer (included in the kit) and mixed by inverting the tube 6 times. Once the mixture turned clear blue, 350 µl of chilled neutralization buffer (included in the kit) were added and mixed thoroughly, when the sample turned yellow, and formed a precipitate, it was centrifuged at 15000xG for 3 minutes; the supernatant was then transferred into a Zymo-Spin™ IIN column (provided with the kit), the column was placed into a collection tube and centrifuged 30 s in a table top centrifuge at maximum speed (18000xG); the flow-through was discarded and the column was washed with 200 µl of endo-wash buffer (included in the kit), upon a brief 15 s incubation, the column was centrifuged again for 30 s at maximum speed (18000xG) and the flow-through discarded. A second washing step was then performed by adding 400 µl of washing buffer (included in the kit) to the column, after a 15 s incubation, the column was centrifuged again for 30 s at maximum speed (18000xG) and the flow-through discarded. Finally, 30 µl of elution buffer (included in the kit) were added to the column and incubated for 1 – 2 h; afterwards the column was centrifuged at maximum speed (18000xG) for 60 s and the flow-through with the purified plasmidic DNA was transferred to a new 1.5 ml Eppendorf tube.

2.3.3 DNA quantitation

The concentration and relative purity of DNA in all our samples was measured by light absorption at 260 and 280 nm using a Nanodrop ND-1000 micro-scale spectrophotometer (accuracy of 2 ng/µl ± 2%), the equipment was initialized with a water sample and calibrated to zero (blanked) with the same buffer where the DNA was diluted. 1 µl of the undiluted sample in question was used for each determination. In this process, the sample, deposited in the spectrometer pedestal, formed a liquid column, held in place by surface tension and trapped between the moving arm and the pedestal itself. The pedestal then moved automatically to adjust the length of the liquid column (between 0.05 and 1 mm) so an optimal length for the light path could be used. An absorption curve across the 200 – 350 nm spectral range was generated; the absorption value at 260 nm was used to determine the double-stranded DNA concentration according to the formula:

(11) $Conc = (OD_{260} - OD_{320}) \times 50\mu\mathrm{l/mL}$, where OD represents the optical density of the sample at 260 and 320 nm.

2.3.4 Polymerase Chain Reaction

DNA was amplified by PCR using the Advantage 2 Polymerase mix system; the reagent mixtures and programs for Occludin and ZO-1 were the following:

ZO-1 Reaction:
18 µL mili-Q H_2O
5 µL 10x Advantage 2 Buffer
2 µL 50 mM $MgCl_2$
2 µL dNTP mix (Pre-mixed stock 25 mM each dNTP)
6 µL forward primer (10 µM) 5' – ACT ATG TCG ACA TGG AGG AAA CAG CTA TAT GG – 3'
6 µL reverse primer (10 µM) 5' – CTA TAC CCG GGC AAA GTG GTC AAT AAG GAC AG – 3'
10 µL DNA template (10-100 ng/µl)
1 µL 50x Advantage 2 DNA polymerase mix (2.5 U/µl)

ZO-1 Amplification program:

1) DENATURATION	96 °C	10:00 min
2) DENATURATION	94 °C	0:40 min
3) ANNEALING	60 °C	0:40 min
4) ELONGATION	68 °C	7:00 min
5) Goto **2)** another 26 times		
6) STORAGE	4 °C	until samples were retrieved

Occludin reaction:
39 µL mili-Q H_2O
5 µL 10x Advantage 2 Buffer
2 µL dNTP Mix (Pre-mixed Stock 25 mM each dNTP)
1 µL Forward PRIMER (10 µM) 5' – ATG TCA TRCC AGG CCT CTT GAA AGT CCA CCT CCT – 3'
1 µL Reverse PRIMER (10 µM) 5' – CTA TGT TTT CTG TCT ATC ATA GTC TCC AAC C – 3'
1 µL template (10-100 ng/µl)
1 µL 50x Advantage 2 DNA polymerase mix (2.5 U/µl)

Occludin amplification program:

1) DENATURATION	95 °C	1:30 min
2) DENATURATION	98 °C	0:45 min
3) ANNEALING + ELONGATION	68 °C	4:30 min
4) Goto **2)** another 19 times		
5) ELONGATION	70 °C	15:00 min
6) STORAGE	4 °C	until samples were retrieved

2.3.4.1 Mutagenic PCR

Site directed mutagenesis was used to introduce different mutations in occludin; a multistep mutagenic PCR was performed. For the first step, two reactions were prepared as follows:

Reaction 1
0.5 µl of 50x Advantage 2 Polymerase mix (2.5 U/µl)
1.5 µl of 10x Advantage 2 Buffer
1 µl of 10 µM dNTP mix
1 µl of 100 µM Forward mutagenic primer
60 ng of DNA template
Volume was adjusted with mili-Q water to 15 µl

Reaction 2
0.5 µl of 50x Advantage 2 Polymerase mix (2.5 U/µl)
1.5 µl of 10x Advantage 2 Buffer
1 µl of 10 µM dNTP mix
1 µl of 100 µM Reverse mutagenic primer
60 ng of DNA template
Volume was adjusted with mili-Q water to 15 µl

Both reactions were amplified simultaneously using the following program:

PCR Step 1:

1) DENATURATION	95 °C	2:00 min
2) DENATURATION	95 °C	0:30 min
3) ANNEALING	65 °C	0:45 min
4) ELONGATION	68 °C	10:00 min
5) Goto **2)** another 4 times		
6) STORAGE	4 °C	until samples were retrieved

Immediately after, both reactions were mixed together, additional 0.5 µl of Advantage 2 Polymerase (2.5 U/µl) were added, and the resulting reaction mixture was amplified using the following program:

PCR Step 2

1) DENATURATION	95 °C	0:30 min
2) DENATURATION	95 °C	0:30 min
3) ANNEALING	62.5 °C	1:00 min
4) ELONGATION	68 °C	10:00 min
5) Goto **2)** another 16 times		
6) ELONGATION	68 °C	20:00 min
7) STORAGE	4 °C	until samples were retrieved

The primers used to introduce the C409A mutation in human occludin were:

Forward: 5' – TGG CGG CGA GTC CGC TGA TGA GCT G – 3'
Reverse 5' – CTC CAG CTC ATC AGC GGA CTC GCC G – 3'

and those to introduce the C500A mutation in human occludin were:

Forward: 5' – GTA AGA AGA ATC ATG CCA AGC AGT TAA AGA GC – 3'
Reverse 5' – GCT CTT TAA CTG CTT GGC ATG ATT CTT CTT AC – 3'

2.3.5 DNA ELECTROPHORESIS AND VISUALIZATION

For DNA visualization, either to corroborate the presence of a specific PCR product, compare concentrations, evaluate for cross-contamination, or to isolate specific DNA types during cloning procedures, the samples in question were mixed 1:1 with loading buffer (bromophenol blue 0,25%, xylene cyanol 0.25%, glycerol 40% in water) loaded into 0.8 – 1.2% Agarose gels, simultaneously with a DNA ladder (1 Kb), and run at 80-100 V for 40-60 min in TAE buffer (Tris base 24.2%, glacial acetic acid 5.71% and 0.5M EDTA-pH 8.0- 10% in water). Visualization was achieved by covering the surface of the gel with Sybr-Safe (1 ml per 50 cm^2 of surface), after a 10 min incubation, the gel was scanned in a fluoroscanner. Usage a laser fluoroscanner instead of a normal UV trans-illuminator allowed the detection of faint DNA bands not visible otherwise and the fast image acquisition reduced the energetic excitation of DNA to less than a second. Besides the increased safety, laser image acquisition provided a way to circumvent UV-related damage to the DNA.

2.3.6 GENERATION OF ELECTROCOMPETENT *E. COLI* DH5α CELLS

Fresh cultures of *E.coli* DH5α cells were prepared from permanent-stocks by inoculation of a frozen scratch into 5 ml of LB medium, without antibiotics, incubating at 37 °C overnight in an orbital shaker at 300 rpm. The whole culture was then transferred to 500 ml of fresh LB medium and regrown at 37 °C until the optical density of the culture (absorption at 600 nm) was between 0.5 and 0.75. The bacteria was then transferred into two 250 ml centrifuge bottles and chilled on ice for 15 minutes. To separate the bacteria from the growing medium, the bottles were centrifuged at 1592 x G for 10 min at 4 °C and the supernatants discarded. The bacterial pellets were then resuspended in ice-cold, mili-Q water and transferred to sterile 50 ml Falcon tubes. After a second centrifugation step (622 x G, 4 °C, 15 min), the supernatants were discarded and the pellets washed with 50 ml of ice cold mili-Q water. A third centrifugation was performed (622 x G, 4 °C, 15 minutes), and the supernatants discarded. The bacterial pellets were then resuspended in 20 ml ice cold, sterile glycerol (10%). Afterwards, the samples were pooled into a single 50 ml Falcon tube and centrifuged again at 622 x G at 4 °C during 15 min. After discarding the supernatants, the bacterial pellets were resuspended in 1 ml of ice cold, sterile 10% glycerol for a total volume of 3 – 4 ml. Aliquots of 50, 100, 250 and 1000 µl were prepared and frozen at -86 °C for storage until use.

2.4 PROTEIN ANALYSIS

2.4.1 WESTERN BLOT

MDCK II cells were cultured until confluency in two 10 cm^2 wells and scrapped in 500 µl of extraction buffer (Triton X-100 1%, 25 mM HEPES/NaOH pH 7.4, 150 mM NaCl, 4 mM EDTA, and 1:500 Protease inhibitor cocktail in water). The samples were fractionated by centrifugation at 15000 rpm for 5 min. The supernatant and pellet contained, respectively, the Triton X-100 soluble and insoluble fractions. Both were resuspended in loading buffer (60 mM Tris-Cl pH 6.8, 2% SDS, 10% glycerol, 5% β-mercaptoethanol, 0.01% bromophenol blue) without reducing agents, boiled for 10 min and loaded into a discontinuous Tris-glycine polyacrylamide system (Laemmli 1970) with 8% or 10% of acrylamide. A molecular weight marker was loaded simultaneously in an adjacent well of the same gel. The samples were then separated electrophoretically. The standard running times were 10 min at 80 V followed by 1 h at 120 V.

After electrophoresis the gels were taken out of their casings, and the proteins blotted to methanol-activated PVDF membranes in a semi-dry transfer cell, using 20 V during 35 min and transfer buffer (0.3% trizma-base, 1.44% glycine, 20% methanol in water). The presence of colored weight marker proteins in the PVDF membrane, but not in the gel, indicated successful protein transfer. The membranes were then washed in TBST buffer (0.1% Tween, 20 mM Tris, 150 mM NaCl in water, pH 7.4) for 5 min on a rocking plate, and incubated overnight at 4°C in blocking solution (5% fat-free milk powder in TBST); alternatively, the membranes were stained in Ponceau-Red solution (0.2% Ponceau S in 1% acetic acid diluted in water) and each protein column cut out, then washed with running water

until no traces of red staining were observed, and incubated overnight in blocking solution at 4 °C. The overnight blocking incubation time could also be substituted by a 2 h incubation at room temperature.

After blocking, the membranes were washed three times with TBST buffer, on a rocking plate, for 3, 5 and 10 min consecutively. In between, an antibody mixture containing the primary and secondary antibodies was prepared diluting them together in 1% fat-free milk powder in TBST. Primary antibodies were diluted 1:50 to 1:250 and secondaries 1:1000 to 1:5000. Once the washing steps were finished, the membranes were enclosed in tight fitting polyethylene bags, the antibody mixture was added on top of them, and the bags sealed. 150 µl of antibody mixture were used per 10 cm^2 of membrane surface. The membranes were incubated for 2.5 h on a rocking plate; afterwards, they were retrieved from the plastic bags, and washed three times, on a rocking plate, with TBST buffer for 3, 5 and 10 min consecutively.

The secondary antibody was conjugated with horseradish peroxidase, thus an acridan-based chemiluminiscent reaction (ECL) was performed immediately after to visualize the bound antibodies using a photodocumenter.

2.4.2 Fluorescent Polyacrylamide Gel Electrophoresis

HEK-293 cells stably expressing YFP-Occludin, or HEK-293 cells transiently transfected with YFP-Occludin^{C409A}, YFP-Occludin^{C500A}, YFP-Occludin$^{C409+500A}$, Claudin-5 YFP, Claudin-12 YFP or Na^+ / K^+ - ATPase's ß-subunit YFP, were quick frozen by submersion in liquid Nitrogen and incubated 30 s in a warm plate. Before they thawed, 12.5 µl/cm^2 of extraction buffer (Triton X-100 1%, 25 mM HEPES/NaOH pH 7.4, 150 mM NaCl, 4 mM EDTA, and 1:500 Protease inhibitor cocktail in water) was added. Cells were scrapped while still icy and transferred into 1.5 ml Eppendorf tubes, which were stored at -86°C for a maximum of 48 h. One or more continuous polyacrylamide gel were then prepared (6%, 8%, or 10% acrylamide) with 0.5 M Tris-HCL (pH 8.8) and 0.05% of SDS and cast in transparent glass cassetes.

Once cast, the gels were placed in a chilled electrophoresis chamber and cooled down to ice temperature. Afterwards, the cell lysates were thawed, sonicated for 10 s (20 kHz, 25 W with power output at 40%) and centrifuged at 15000 rpm for 15 min at 4 °C. The supernatants were diluted with loading buffer (0.5-2% of SDS, 20% of glycerol and 125mM of Tris-HCL pH 6.8, colorless and free of reducing agents) at a 1:1 ratio and loaded into the gel. A fluorescent molecular weight marker was loaded simultaneously, in an adjacent well of the same gel. Only when required, the reducing agent dithiothreitol (DTT) was added (final concentration of 150 mM) to the loading buffer, and the samples incubated for 15 minutes at 37 °C. If needed, a small amount of a 20% Glycerol solution stained with Orange G (0.01%) was poured on the wells to make them visible before loading the samples. Conventional blue dyes were avoided, since they interfered with the subsequent fluorescent laser detection.

Electrophoresis was performed with 120 V for 30 - 40 min, and ice-cold running buffer (0.25 M Tris, 1.92 M Glycine, 1% SDS, pH 8.3 – diluted 1:10) was used. Immediately after, the gel was visualized, while still inside its casing; for this purpose a fluoroscanner (FUJI FLA-5000) equipped with a 473 nm laser line was used. Fluorescence was read with a 510 nm long-pass filter (LPB/Y510) using a photomultiplier current of 500 V. The resulting images were stored in FUJI proprietary format and converted into TIFF 16-bit grayscale images for further analysis using AIDA (v. 3.52 – Raytest, Germany) and Image J (NIH, USA).

2.5 SPECTROSCOPY AND SPECTROPHOTOMETRY

2.5.1 DETERMINATION OF NADH CONSUMPTION BY ULTRAVIOLET-VISUAL SPECTROSCOPY

HEK-293 cells stably expressing YFP-Occludin^{WT} or YFP-Occludin^{C409A} were harvested as if they were to be processed for Fluorescent-PAGE; once the extraction buffer was added, they were kept on iced water and centrifuged at 20817 x G for 15 minutes, the supernatant was then divided in several aliquots in UV transparent cuvettes, each aliquot was diluted to 5% in Ca^{++}/Mg^{++} free-PBS for a final volume of 750 µL. To each of the aliquots, 150 µL of a NADH solution (in water) at concentrations ranging from 10 µM to 3 mM were added and mixed. The light absorbance was determined after one minute, in the range from 250 to 400 nm using a UV-Vis (Jasco V-550) spectrophotometer.

The light absorbance of a 10 mM solution of NADH measured alone showed an absorbance peak at 340 nm. In contrast, a 50 mM solution of NAD^+ showed nil absorbance at such wavelength. The absorbance values at 340 and 260 nm were used to measure the NADH and NAD^+ concentrations respectively.

The experiments were repeated using a Nanodrop ND-1000 micro-scale spectrophotometer. For such purpose 4 µl of cell extracts were mixed with 4 µl of NADH (at different concentrations). When required DTT was added directly to the cell extracts before the experiment to a final concentration of 100 mM. The results using both spectrophotometers were similar.

2.6 IMAGE ANALYSIS

2.6.1 MICROSCOPICAL IMAGERY

All confocal microscopy images were acquired and saved in LSM-Zeiss proprietary format. For general evaluation, LSM Image examiner and Zeiss Efficient Navigation – ZEN (Carl Zeiss, Germany) were used. For complex procedures, e.g. fluorescence density measurements, digital substraction, particle counting, intensity profiling, surface profiling, precise tridimensional reconstructions, and 3 or 4 dimensional stack calculations, the images were imported and analyzed in Image J.

2.6.2 QUANTITATION OF THE MEMBRANE AND INTRACELLULAR OCCLUDIN POOLS

A plug-in for Image J was created to compare the amount of YFP-Occludin associated with the plasma membrane (membrane pool) against the amount of YFP-Occludin found elsewhere inside of the cell (considered here as the intracellular pool). Trypan blue was used as membrane marker (75 µl of a 4 °C 0.4% trypan blue solution per 500 µl of plating medium), and the confocal detection channel for trypan blue was used as an alpha channel to perform a logical negation on the whole YFP-Occludin signal (as in YFP-Occludin **NOT** Trypan Blue). The resulting image contained exclusively the cytosolic pool of YFP-Occludin; this image was used to perform a second logical negation of the whole YFP-Occludin signal (as in YFP-Occludin **NOT** intracellular pool). The result was an image containing exclusively the membrane pool of YFP-Occludin. The amount of occludin in the membrane and intracellular pools was then quantified; the images were binarized and the surface occupied by all the YFP-signals was measured. The membrane to intracellular ratio was calculated as

(12) Membranal ratio = Membrane pool / intracellular pool

2.6.3 FLUORESCENCE PROFILING

Fluorescence intensity profiles were generated by creating a straight or curved vectorial path on a confocal microscopy image. The fluorescence intensity at each point in that vector was measured using Image J.

2.6.4 ELECTROPHORESIS IMAGERY

Images obtained from gel electrophoresis (Western Blot or F-PAGE) were converted to 16-bit TIFF images and analyzed in Image J (Public domain – NIH). When required, and only for better visualization, contrast enhancement was used and applied similarly to all the samples from the same experiment. Intensity analysis and quantification was performed on the raw unaltered format of the images.

2.7 IN-SILICO ANALYSIS

2.7.1 PROTEIN ANALYSIS

Theoretical analysis of proteins was achieved using a series of online, free access software platforms. Protein sequence similarity searches were performed using the Basic Local Alignment Search Tool (BLAST)[2]. Multiple sequence alignments were performed using EBI-ClustalW2[3]. The primary structures, basic biochemical data, and sequence annotations were obtained from the UNIPROT database[4] (Jain et al., 2009). The entry reference number for ZO-1 was Q07157 and for Occludin Q16625. Automatic translation of DNA sequence was performed using the Translate tool at the Swiss

[2] http://blast.ncbi.nlm.nih.gov/Blast.cgi
[3] http://www.ebi.ac.uk/Tools/msa/clustalw2/
[4] http://www.uniprot.org/

Institute of Bioinformatics[5]. Reverse translation, was performed using the Reverse translate tool[6] of the Sequence Manipulation Suit from the University of Alberta, Canada. Prediction of phosphorylation sites was performed using the NetPhos 2.0 and NetPhosK 1.0[7] servers from the Center for Biological Sequence Analysis at the Technical University of Denmark (Blom et al., 1999).

2.7.2 MOLECULAR MODELING

2.7.2.1 Modeling of the occludin c-terminal 266-415 fragment

Molecular modeling from scratch was performed using the iterative threading-assembly-refinement algorithm[8] (Roy et al., 2010; Zhang 2008) from the I-TASSER server at the University of Michigan, USA.

The I-TASSER algorithm involves the retrieval of super-secondary structure templates by the Local Meta-Threading Server (LOMETS)-based protein-fold recognition software[9] (Wu and Zhang 2007). Those templates, and additional small protein fragments, were retrieved from solved tridimensional structures and were assembled into full-length models by Monte-Carlo replica-exchange simulations, threading the missing regions built by ab-initio modeling. If no appropriate templates were found, the whole structure was built ab-initio. In all cases, from all the possible predictions, the models with the nearest-to-native protein folding patterns (those with the lowest free energy) were selected, using the SPICKER service[10] (Zhang and Skolnick 2004), by clustering the simulation decoys (assemblies that are structurally different than the native configuration being built but are thermodynamically indistinguishable from it); this allowed the identification of the decoy cluster centroids, which served as starting point to build an improved version of the model; during this second iteration, the spatial restrictions, imposed by the super-secondary structures templates and small protein fragments, were used to guide the modeling simulations. The proper protein fragments and templates were selected by 1) alignment of the best possible equivalent residues based on structural similarities using TM-ALIGN[11], and 2) calculation of their overall amino acid equivalency score[12] -TM-SCORE- (Zhang and Skolnick 2004 and 2005). This process was used to get rid of steric clashes and to refine the global topology of the cluster centroids; afterwards, the generated decoys were clustered again, and the lowest energy structures were selected.

---

[5] http://expasy.org/tools/dna.html
[6] http://www.bioinformatics.org/sms2/rev_trans.html
[7] http://www.cbs.dtu.dk/services/NetPhosK/, and http://www.cbs.dtu.dk/services/NetPhos/
[8] http://zhanglab.ccmb.med.umich.edu/I-TASSER/
[9] http://zhanglab.ccmb.med.umich.edu/LOMETS/
[10] http://zhanglab.ccmb.med.umich.edu/SPICKER/
[11] http://zhanglab.ccmb.med.umich.edu/TM-align/
[12] http://zhanglab.ccmb.med.umich.edu/TM-score/

The final tridimensional atomic model was generated by applying a protocol to refine the full atomic protein, modeled from the C-alpha traces, by optimizing the hydrogen-bonding networks using -REMO[13]- (Li and Zhang 2009).

2.7.2.2 Modeling of the hinge region of ZO-1

The hinge region of ZO-1 was modeled in Swiss-model[14] (Arnold et al., 2006), the program was fed with the whole sequence of the SH3-Hinge-GuK unit of ZO-1, and the known crystal structure[15] of the SH3-GuK core of ZO-1, but without the hinge region, was chosen as a template. The resulting hybrid model contained the predicted hinge region structure attached to the crystal structure model and was stored as a PDB file.

2.7.2.3 Calculation of binding interfaces and modeling of quaternary structures

The "Protein interfaces, surfaces and assemblies service - PISA" at the European Bioinformatics Institute[16] (Krissinel and Henrick 2007) was used to analyze the asymmetric units of the SH3-GuK unit of ZO-1 and the coiled-coil domain of occludin for possible oligomeric forms. The oligomeric structure with the lowest solvation free energy upon forming of the binding interface was stored as a PDB file. Thermodynamical stability of the assemblies was analyzed with the formula $\Delta G_0^{diss} = -\Delta G^{Int} - (T\Delta S)$, where ΔG_0^{diss} is the free energy of dissociation, ΔG^{Int} is the free energy gain upon bringing the assembly units together (calculated per each monomer), T is the absolute temperature and ΔS is the entropy change upon dissociation ($T\Delta S$ represents the entropy driving force of dissociation). The ΔG^{Int} for a given oligomeric assembly, depends on the changes on solvation energy (ΔG_{Solv},), and immediate contact-dependent (ΔG_{cont}) and electrostatic interactions (ΔG_{elec}) of the different assembly subunits. Thus, the ΔG^{Int} of a molecular assembly "A" was calculated, according to Krissinel (Krissinel and Henrick 2007), as:

$$\Delta G^{Int}(A) = \Delta G_{Solv}(A) - \sum_{i=1}^{n} \Delta G_{Solv}(A_i) + \sum_{j>i} \Delta G_{cont}(A_i, A_j) + \sum_{j>i} \Delta G_{elec}(A_i, A_j)$$

Where i and j are two subunits in the complex A. The solvation energy can be interpreted as the energy required to replace a cavity in a solvent with the molecular assembly A.

2.7.2.4 Calculation of surface electronegativity values

Surface electronegativity maps for the PDB models were calculated by solving the Poisson-Boltzmann equation for the respective models, using the Adaptive Poisson-Boltzmann Solver (ABPS) program (Baker et al., 2001), according to the formula:

---

[13] http://zhanglab.ccmb.med.umich.edu/REMO/
[14] http://swissmodel.expasy.org/
[15] 3lh5.pdb
[16] http://www.ebi.ac.uk/msd-srv/prot_int/pistart.html

(15) $$\vec{\nabla} \cdot \left[\epsilon(\vec{r})\vec{\nabla}\Psi(\vec{r})\right] = -\rho^f(\vec{r}) - \sum_i c_i^{\infty} z_i q\, \lambda(\vec{r}) \cdot e^{\left[\frac{-z_i q \Psi(\vec{r})}{k_B T}\right]}$$

Where $\vec{\nabla}$ represents the vector divergence operator (magnitude of vector's field sourge or sink at a given point), $\epsilon(\vec{r})$ is the dielectric constant at the evaluation position r. $\vec{\nabla}\Psi(\vec{r})$ is the change in electrostatic potential (gradient), $-\rho^f(\vec{r})$ is the solute's electrical charge density, c_i^{∞} is the concentration of the ion in question (in this case i) when is located at an infinite distance from the solvent, z_i is the charge of such ion, q is the charge of the proton, $\lambda(\vec{r})$ is the position dependent accessibility factor for ion *i* at the evaluation position r. k_B is the Boltzmann constant equivalent to 1.38065 x 10^{-23}, T is the temperature and e is the Euler's number, equivalent to 2.71829.

The equation (15) describes the electrostatic interactions between molecules in ionic solutions, and solving the equation for a particular molecule is one of the most popular ways to model implicit solvation (Continuum solvation), used to represent the solvent as a continuous medium, in opposition to individual solvent molecules. Continuum models are commonly used to describe electrostatic interactions between molecular solutes in salty, aqueous media, and continuum electrostatic simulations play an important role in modeling protein – protein interactions or protein – ligand interactions since they are used for simulations to determine theoretical binding kinetics and molecular dynamics.

In order to solve the equation for the hybrid model of the SH3-hinge-GuK unit of ZO-1, the crystal structure model of the coiled-coil domain of occludin, and its theoretical dimeric model, their respective PDB files were modified by adding missing heavy atoms, determining the pKa of the amino acid side-chains, placing missing hydrogen atoms, optimizing the models to favor hydrogen bonding, and assigning charges and atomic radii parameters. These procedures were performed using a standalone version of the PDB2PQR program (Dolinsky et al., 2004 and 2007). An AMBER (Assisted Model Building with Energy Refinement) molecular dynamics force field (Wang et al., 2000) was used for the calculations and the outcome files were stored in PQR format.

The APBS program was fed with the PQR files and a single dx file was obtained, this was recalled in the molecular viewing program Chimera-UCSF (University of California, San Francisco, USA) to superimpose the electrostatic parameters on the surface of the different molecular models that were studied.

2.7.2.5 Model visualization

Molecular graphic images, visualization, angle and distance measurements, tridimensional alignments, surface mapping, representation of surface electrostatic potentials, and analysis for structural complimentary, were performed using the UCSF Chimera package from the Resource for Biocomputing, Visualization, and Informatics at the University of California, San Francisco (Pettersen EF et al., 2004).

2.8 STATISTICS

Statistical analysis was performed in Excel 2010 data sheets (Microsoft), using the built-in statistical functions, supported by the XL-STAT 2010 plugin (Addinsoft SARL). Normality tests were done by the Kolmogorov-Smirnov and Pearson's chi squared methods; variance was analyzed by one-way ANOVA, and binomial groups were compared with two-tailed, heteroscedastic t-tests.

2.9 REAGENTS

The reagents used, lot numbers, and their respective sources are summarized in table I:

Table I. Reagents

Reagent	**Company**	**Location**	**Lot No.**
Acetic acid	MERCK	Darmstadt, Germany	Diverse
Acrylamide **Acrylamide bis-Acrylmide 30% Solution Mix ratio 20:1**	Sigma-Aldrich chemie	Steinheim, Germany	51K9292
Advantage 2 Polymerase system **50x BD Advantage 2 Polymerase mix 10x Advantage 2 PCR buffer**	Clontech. BD Biosciences	Heidelberg, Germany	Diverse
Agar-agar	Carl Roth	Karlsruhe, Germany	Diverse
Agarose	SERVA	Heidelberg, Germany	090916
Ammonium persulfate	Bio-Rad	Hercules, CA. USA	170483A
Ampicillin sodium salt	Carl Roth GmbH	Karlsruhe, Germany	15463604
Anaerobic indicator **BR55**	Oxoid Limited	Basingstoke, Hampshire. UK	102835001
DMSO **Dimethyl sulphoxide Hybri-MAX**	Sigma-Aldrich Chemie	Taufkirchen, Germany	
dNTP **mixed set PCR grade (100 mM)**	Invitrogen	Carlsbad, CA. USA	302526
DTT **1,4-Dithiothreitol**	Biomol	Hamburg, Germany	3044
GLUTA-MAX DMEM. **Dulbecco's Modified Eagle Medium + GLUTA MAX I**	Invitrogen. GIBCO	Karlsruhe, Germany	Diverse
ECL "**Amersham™ ECL-Plus"**	GE Healthcare.	Buckinghamshire, UK	155
EDTA "**Ethylenenendiamine-tetraacetic acid 2Na H_2O"**	Carl Roth	Karlsruhe, Germany	2053583
Ethanol **(99.9%) Undenatured**	Berkel AHK	Berlin, Germany	Diverse
Fluorescent molecular weight marker. **Fluorescent protein standard Benchmark**	Invitrogen	Karlsruhe, Germany	660638
DNA Ladder **GeneRuler 1Kb DNA Ladder (0,5 µg/µL)**	Fermentas	St. Leon-Rot, Germany	00033708

Genetycin **(G418)**	Calbiochem / EMD Bioisciences	La Jolla, CA. USA	Diverse
Glutaraldehyde **Grade I 25%**	Sigma-Aldrich Chemie	Steinheim, Germany	088K5321
Glycerol **Rotipuran >86%**	Carl Roth	Karlsruhe, Germany	Diverse
Glycine	SERVA	Heidelberg, Germany	100087
HEPES **2-[4-(2-Hydroxyethyl)-1-piperazinyl]ethane sulfonic acid**	Biochrom	Berlin, Germany	AD0210
IFN-γ	Immunotools	Friesoythe, Germany	351574
Isopropanol **2-Propanol**	VWR International	Briare, France	Diverse
Kanamycin sulfate	Carl Roth	Karlsruhe, Germany	19465104
Lipofectamine 2000	Invitrogen	Carlsbad, CA. USA	Diverse
Methanol	Mallincrkrodt Baker B.V	Deventer, Holland	Diverse
Methylene blue	MERCK	Darmstadt, Germany	K21532979 447
Molecular weight marker. **SeeBlue Plus2 pre-stained**	Invitrogen	Carlsbad, CA. USA	Diverse
NADH **Reduced Nicotinamide-adenine-dinucleotide.**	VEB Arzeinmittelwerk	Dresden, Germany	1110880
NAD^+ **Oxidized Nicotinamide-adenine-dinucleotide.**	Boehringer Manheim GmbH	Germany	1156398
Optimem	Invitrogen	Karlsruhe, Germany	Diverse
Orange G	Fluka chemie AG	Buchs, Switzerland	370045/1 45097
PBS **Dulbecco Phosphate buffered saline with or without Ca^{++}/Mg^{++}**	Biochrom AG	Berlin, Germany	Diverse
Penicillin (10000 U/ml) / streptomycin (10000 µg/ml)	Biochrom	Berlin, Germany	Diverse
Peptone from casein	Carl Roth	Karlsruhe, Germany	Diverse
Plasmid mini-prep kit Zyppy.	Zymo Research	Irvin, CA. USA	Diverse
PLL **Poly-L-Lysine hydrobromide**	Sigma-Aldrich chemie	Steinheim, Germany	Diverse
Ponceau S. Sodium salt	Sigma-Aldrich Chemie GmbH	Steinheim, Germany	Diverse
Primary antibodies (**rabbit anti-occludin**)	ZYMED	San Francisco, CA. USA	00660748 21074197 30678347 and 40186141
Protease inhibitor cocktail	Sigma-Aldrich Chemie	Steinheim, Germany	014K4011
Secondary antibodies **(Alexa fluor 488 labeled goat anti-rabbit)**	Invitrogen. Molecular Probes	Eugene, OR. USA	Diverse

NaCl **Sodium chloride**	Mallincrkrodt Baker B.V.	Deventer, Holland	0019230066
Sodium dodecylsulfate	SERVA	Heidelberg, Germany	060698
Sodium hydroxide	Chemapol	Prague, Czech republic	503661083
SYBR-Safe **DNA gel stain 10,000 X in DMSO**	Invitrogen. Molecular Probes	Eugene, OR. USA	665872
TEMED **N,N,N',N'-Tetrramethylethylendiamine**	Sigma-Aldrich Chemie	Steinheim, Germany	38H0438
TNF-α	Immunotools	Friesoythe, Germany	351942
TRIS-Base **TRIS-(Hydroxymethyl-aminomethane) (>99%)**	Carl Roth	Karlsruhe, Germany	120155197
TRIS-HCL **Tris Hydrochloride (>99%)**	Carl Roth	Karlsruhe, Germany	210153298
Triton X-100	SERVA	Heidelberg, Germany	Diverse
Trypan blue	Sigma.Aldrich chemie	Steinheim, Germany	Diverse
Trypsin 0,05% – EDTA 0,02%	Invitrogen. GIBCO	Karlsruhe, Germany	Diverse
Xylene cyanol	Fluka chemie AG	Buchs, Switzerland	372837/1 54497
Yeast extract	Carl Roth	Karlsruhe, Germany	Diverse

2.10 MATERIALS AND EQUIPMENT

The equipment used, is summarized in table II.

Table II. List of Equipment

Reagent	Company	Country of origin
Anaerobic workstation Concept plus	IUL Instruments / Ruskinn Technology Limmited	UK
Biological Safety Cabinet BDK	Luft-und Reinraumtechnik	Germany
CCTV - 3CCD Microscopic color video camera	Sony	Japan
CCTV-F15HS High sensitivity microscopic camera	Panasonic	Japan
CCTV-WV-BL200 Photodocumenting camera	Panasonic	Japan
Cell counter – CASY 1	Schärfe system	Germany
Cell incubator (37° 10% CO2) CB210	Binder	Germany
Cell incubator (37° 5% CO_2)	Nalge-Nunc	USA

Cell scrappers	TPP	Switzerland
Centrifuge 5415C	Eppendorf	Germany
Centrifuge 5810 Rotors: F45-30-11 and A-4-62	Eppendorf	Germany
Centrifuge Falcon tubes	TPP	Switzerland
Confocal biphotonic laser module Titan/Saphir (720-930nm) – Tunable.	Coherent	UK
Confocal system LSM 510 Meta Stative AXIOVERT 200M Laser module LSM 510: He/Ne line (543nm, 633nm) + Ar line (458nm, 488nm, 514nm)	Carl Zeiss	Germany
Cryo 1°C Freezing container	Nalgene	USA
Cryo preserver tank CHRONOS Liquid N2 tank APOLLO and automatic regulator ADUR-ß	Cryotherm	Germany
Cryo vials 1.2 ml	Corning	Mexico
Deep freezer -86 ULT	Thermo Forma	USA
DNA Gel Electrophoresis Chamber Agagel-mini	Biometra	Germany
Electrophoresis chamber Mini-protean II	Bio-rad	USA
Electrophoresis power supply 3000 Xi	Bio rad	USA
Electrophoresis Power supply E835	Consort	Belgium
Electroporation cuvettes 1mm electrode gap	Peqlab biotechnologie	Germany
Electroporator EQUIBIO Easyject Prima	Thermo electron corporation	USA
Fluorescence microscope OLYMPUS BH2-RFCA	Olympus	Japan
Fluoroscanner – FLA-5000. Fluorstage and Multistage 4046. Filter LPB/Y510	FUJIFILM	Japan
Glass-bottom tissue culture chambers. Lab-Tek. Thickness 1.0	Nunc	USA
Heating plates Präzitherm PZ-28-1T	Störktronic	Germany
Inverted phase contrast microscope	Olympus optical Co.	Japan
Multiwell chambers (6, 12, 24 and 96)	TPP	Switzerland
Orbital incubator TH-15	Edmund Bühler	Germany
Petri dishes (different sizes)	TPP	Switzerland
Ph Meter	Toledo	Switzerland
Photodocumenter ChemiDoc EQ	Bio rad	USA

Precision Balance	Sartorius	Germany
Rocking plate Polymax 2040	Heidolf	Germany
Serological pipettes (2, 5, 10 and 25 ml)	TPP	Switzerland
Spectrofluorometer FP-6500 Temperature controller ADP-303T	Jasco	Germany
Spectrophotometer DU 640	Beckman	Germany
Spectrophotometer NanoDrop ND-1000	Thermo Scientific	USA
Spectrophotometric cuvettes	BrandTech Scientific	USA
Thermocycler PTCDNA Engine	Bio-rad	Germany
Thermomixer 5436	Eppendorf	Germany
Tissue culture-treated flasks (T75)	TPP	Switzerland
Tissue culture-treated flasks Cellstar	Greiner bio-one	Germany
Trans-blot SD Cell Semi-Dry Transfer cell	Bio-rad	Germany
Ultrasound microhomogenizator Vibracell 72434	Bioblock Scientific	France
UV/VIS Spectrophotometer V-550 Temperature controller ETC-505T	Jasco	Germany
Vacuum pump	Helmut Saur Laborbedarf	Germany
Vortex Genie 2	Bender & Hobein	Switzerland
Water bath	Gesselschaft für Labortechnik	Germany

3 RESULTS

3.1 OCCLUDIN IS EXPRESSED IN THE PLASMA MEMBRANE OF HEK 293 CELLS

3.1.1 EXPRESSION PATTERN OF YFP-OCCLUDIN IN HEK-293 CELLS

Stably transfected HEK-293 cells expressed exogenous YFP-Occludin in the plasma membrane and intracellular compartments. Although the membranal YFP-Occludin formed a quasi-continuous ring surrounding the cells, a strong difference in the fluorescence intensity was observed between cell-cell contacts (the regions of the plasma membrane where two cells came in contact) and non-cell-cell contact regions; under similar observation conditions, the fluorescence intensity, in any given region of the plasma membrane, correlates to the fluorescent protein concentration in that location. The concentration of YFP-Occludin at cell-cell contacts, in HEK-293 cells, was higher than elsewhere in the membrane and was considered enriched at cell-cell contacts (**Fig. 12A**).

The degree cell-cell contact enrichment correlates with the capability of a membranal protein to self-interact in *trans* (between two neighboring membranes). As means to quantify the degree of occludin trans-interaction, the YFP fluorescence ratio between cell-cell contacts and non-cell-cell contacts (contact enrichment factor), was calculated by fluorescence profiling; the average contact enrichment factor of YFP-Occludin was 2.44 ± 0.10 (**Fig. 12 B and C**).

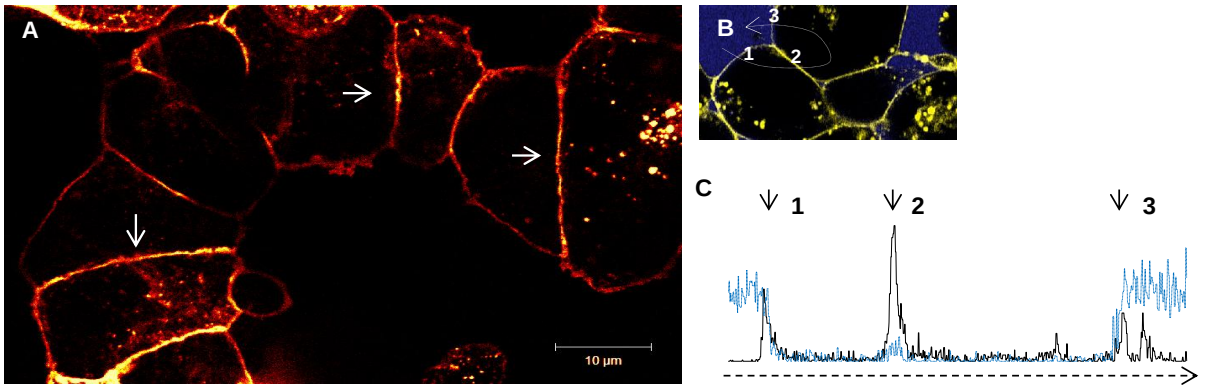

Fig. 12. Membranal expression and trans-interaction of YFP-Occludin in HEK-293 cells.

A) The areas where occludin is enriched are shown in brighter color. It's noticeable the enrichment at the cell-cell contacts (arrows). A number of intracellular vesicles containing occludin are also observed

B and C) The fluorescence intensity of YFP-Occludin was measured across the path shown by the white line in B and the resulting profile is shown in C (black plot). The fluorescence profile of trypan blue, used to identify the plasma membrane, is also shown in C (blue plot). The black horizontal arrow in C follows the direction of the white arrow in B. The small arrows labeled 1, 2 and 3 in C mark the three membranes where the fluorescence intensity was measured to calculate the enrichment factor and correspond to the same numbered locations in B. The contact enrichment factor equals the YFP-fluorescence intensity at peak 2, divided by the sum of the fluorescence intensity at peaks 1 and 3.

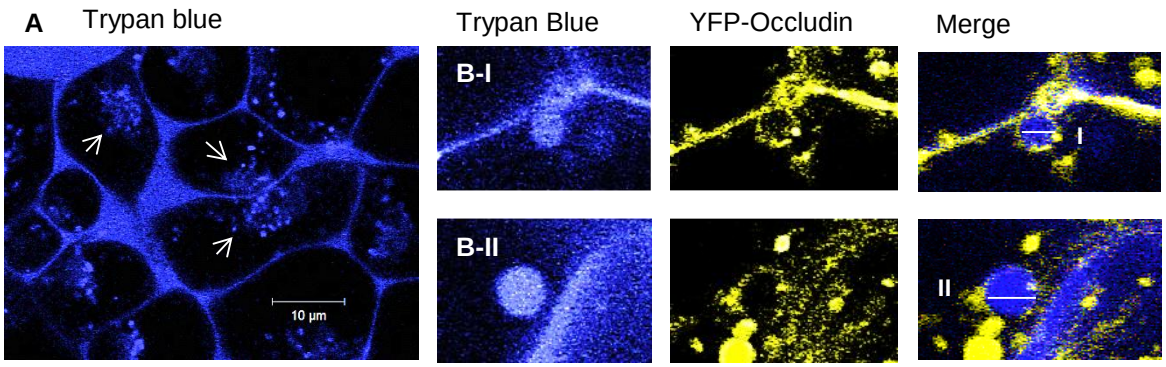

Fig. 13. Internalization of YFP-Occludin in HEK-293 cells, visualized by trypan blue.

A) Several intracellular compartments where trypan blue was collected are seen in the cytosol of HEK-293 cells (Arrows). These are presumed to be endocytic / recycling compartments.

B-I and B-II) provide detail on two different trypan blue containing vesicles in HEK-293 cells expressing YFP-Occludin. In the frames to the right, YFP-Occludin can be seen surrounding these internalized vesicles. In the merged frames, the line labeled as I measures 1.86 µm and the line II 2.10 µm.

Trypan blue was used to identify the cell surface. Besides being adsorbed into the cell membrane (Wallace 1972), it was also internalized into intracellular compartments ranging from 0.2 to 3 µm in diameter; a number of these compartments showed YFP-Occludin in their periphery (**Fig. 13**). Since the uptake of trypan blue directly correlates with the surface area of the plasma membrane (Wajc

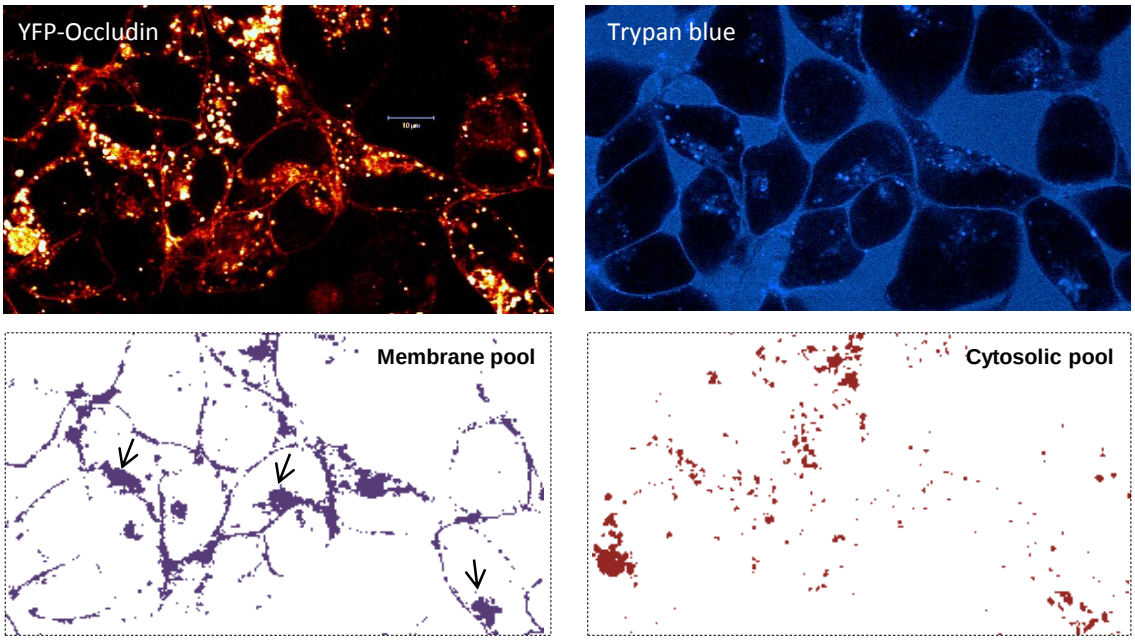

Fig. 14 Digital substraction of the membrane and intracellular pools of YFP-Occludin. The membranal occludin pool was considered as the YFP-Occludin signal colocalizing with trypan blue. The membrane pool was larger than the intracellular pool in HEK-293 cells expressing YFP-Occludin and cultured in normoxic conditions. The arrows show YFP-Occludin colocalizing trypan blue at intracellular compartments.

1977, Jacques 1973), the intracellular YFP-Occludin signal colocalizing with trypan blue was considered as bound to the cell membrane. Thus, the entire YFP-Occludin signal colocalizing with trypan blue was referred to as the *membrane pool*. Using digital substraction, the membrane pool of YFP-Occludin was separated from the YFP-Occludin signal found elsewhere in the cell, the *intracellular pool* (**Fig. 14**). The mathematical comparison of both pools was considered as the **membranal ratio** and provided an objective way to measure the amount of YFP-Occludin expressed in the plasma membrane. The average membranal ratio for YFP-Occludin when expressed in HEK-293 cells was 2.23 ± 0.10.

3.1.2 YFP-Occludin is distributed apically at the cell-cell contacts

Further microscopic analysis of HEK-293 cells expressing YFP-Occludin, revealed that the cell-cell contact areas where occludin was enriched were located in the upper half (apical) of the lateral membrane. In contrast, this apical localization was not found in HEK-293 cells expressing claudin-5 YFP alone (**Fig. 15**).

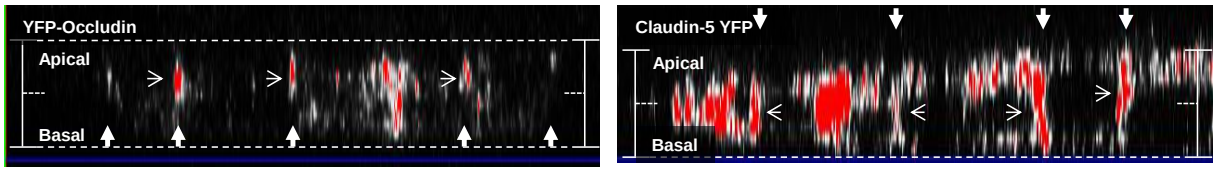

Fig. 15 Preferential localization of YFP-Occludin in HEK-293 cells at the apical region of the cell-cell contacts. YFP-Occludin was enriched in the apical half of the lateral membrane, at the cell-cell contact regions when expressed in HEK-293 cells (arrows). In contrast, another tight junction protein, Claudin-5 YFP, although enriched at cell-cell contacts (arrows) when expressed also in HEK-293 cells, did not show the same apical tendency. The vertical filled arrows mark the spatial position of the cell membranes. Red areas represent regions with higher fluorescence intensities then white areas. The threshold to define “high” and “low” was selected arbitrarily to favor understandability.

3.2 Occludin forms dimers that are sensitive to reduction

To further characterize the expression pattern of occludin and investigate its oligomerization potential, immunodetection of endogenous occludin in MDCK-II cells was performed by western-blots. A band at approximately 64 kDa was consistently found; in only a few experiments, an additional faint band was present at approximately 130 kDa (**Fig. 16**). The apparent molecular weight of this band was consistent with an occludin dimer; however, this band proved to be particularly difficult to detect under several experimental conditions and with different antibody batches.

To overcome the immunodetection problems, a Fluorescent PAGE (F-PAGE) assay was used to detect occludin without relying on antibodies, taking advantage of the fluorescent tag already incorporated into YFP-Occludin.

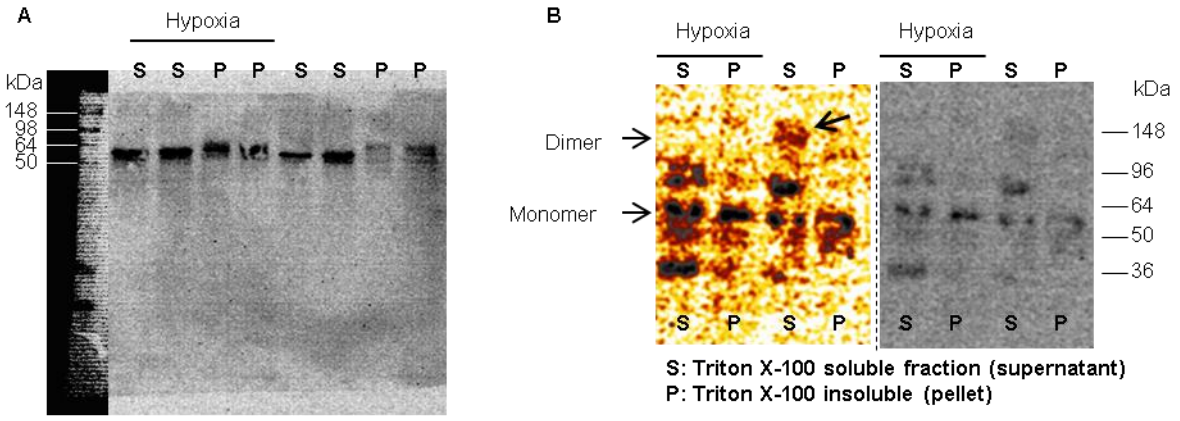

Fig. 16. Immunodetection of Occludin in MDCK II cell lysates. Cells were lysed and treated with Triton X-100 to extract the membrane proteins, after centrifugation, The Triton X-100 soluble (S) and resistant (P) fractions were loaded into a polyacrylamide gel for electrophoresis. After blotting, immunodetection was performed using monoclonal mouse anti occludin antibody.

A) The image shows an intense band of occludin at approximately 64 kDa, two additional weak bands are observed right on top and below, and presumably correspond to different phosphorylation species of occludin

B) Strong monomeric bands at approximately 64 kDa, and an additional band in the supernatant, at around 80-90 kDa (in the Triton X-100 soluble fractions). A third faint band can be observed at around 130 kDa (yellow arrow). Digital enhancement was required to make this weak band apparent. The left (enhanced) and right (original) halves of the image show the same blotted membrane.

The F-PAGE analysis of HEK-293 cells expressing YFP-Occludin showed six groups of bands: one group at ~90 kDa, corresponding to the calculated molecular weight of the monomeric YFP-Occludin (64 kDa of occludin itself plus 25 kDa of the YFP tag), the two or three bands observed here were presumed to correspond to the different known phosphorylation forms of occludin. A second group of bands was observed at ~180 kDa, correlating with the expected molecular weight of dimeric YFP-Occludin. A third group of faint bands was found at ~270 kDa, correlating with the expected molecular weight of trimers; the fourth band region, with extremely high molecular weight corresponded to higher order oligomers. A fifth group of bands, presumably corresponding to partially degraded occludin, was observed at <60 kDa (**Fig. 17 A**). Further analysis revealed that treating the samples with the reducing agent dithiothreitol (DTT - 150 mM) induced the loss of the 180 kDa band (dimer), while trimers and higher order oligomers were apparently unaffected (**Fig. 17 B**). Our study was focused on the study of the dimeric / monomeric forms of occludin.

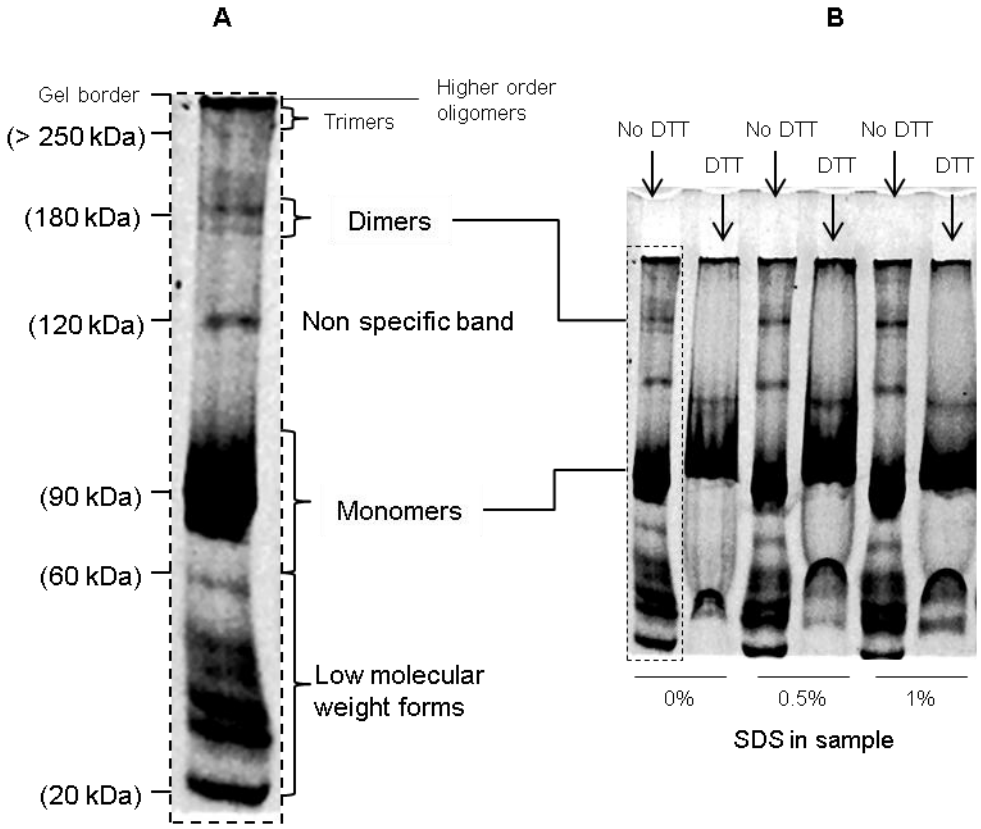

Fig. 17 Occludin forms dimers that are sensitive to chemical reduction.

A) Different electrophoretical forms of YFP-Occludin as shown by Fluorescence-PAGE (F-PAGE).

B) The dimeric forms of YFP-Occludin disappeared when the reducing agent dithiothreitol (DTT) was added to the samples (150 mM).

3.3 HYPOXIA DISORGANIZES THE EXPRESSION PATTERN OF OCCLUDIN

3.3.1 CELLULAR CONTENT OF NADH DURING HYPOXIA

NADH can be used to estimate the cellular redox conditions. The cellular content of NADH in untransfected HEK-293 cells was measured by confocal microscopy and compared between cells cultured under hypoxia for 3 h and normoxic cells. The average NADH fluorescence intensity in hypoxic cells was 720.4 ± 7.63 A.U. while normoxic cells showed an average of 665.5 ± 4.16 A.U (n=10 p < 0.001). (**Fig. 18 A**). Trypan blue staining showed that the cells were still viable after 3 h of hypoxia, but the dye internalization was strongly reduced compared to normoxic cells (**Fig. 18 B**); this behavior was reversed if the cells were maintained at 37°C in normal air (20% O_2) for 2 h, and cells remained viable for the following days if returned to normal culturing conditions. If hypoxia was sustained for more than 17 h the cells rounded up, detached from the substrate, and allowed a diffuse cytosolic staining of trypan blue, signs that indicated cell death (**Fig. 18 B**). This indicated that hypoxia for 3 h induced cellular physiological changes without compromising the cell viability. Thus 3 h were used as a standard time for all experiments involving hypoxia.

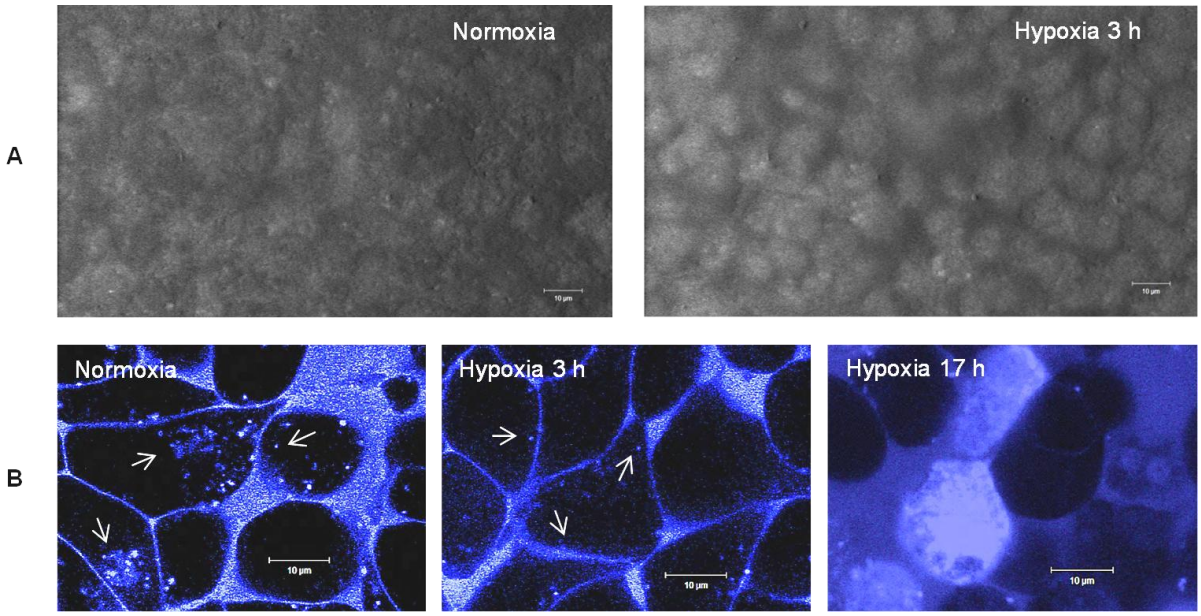

Fig. 18. Effects of hypoxia (3 h) on the cellular NADH content and trypan blue internalization in HEK-293 cells

A). Microscopical appearance of the NADH content in HEK-293 cells cultured in normoxic and hypoxic conditions. The cells showed a moderate increase in the NADH fluorescence (diffuse gray signals) after 3 h of hypoxia

B) Internalization of trypan blue in untransfected HEK-293 cells. The arrows point to intracellular compartments containing trypan blue. The amount internalized trypan blue considerably decreased after 3 h of hypoxia; this behavior was reversed if the cells were re-oxygenated and returned to normal culturing conditions. If hypoxia was maintained for longer times, the cells rounded up, detached and allowed a diffuse cytosolic trypan blue staining, and indication of cell death.

3.3.2 Expression of YFP-Occludin in Hypoxic HEK-293 cells

Confocal microscopy analysis of HEK-293 cells expressing YFP-Occludin, cultured in hypoxia, showed that YFP-Occludin was located mainly inside of the cells while some of the protein remained in the plasma membrane (**Fig. 19 A**).

The intracellular vesicles/compartments where occludin was localized were either immobile, or, in a minority of cases, showed exceptionally low mobility. Exposing the cells to normal air for 2 h induced the recovery on the mobility of these vesicles, but the subcellular distribution of occludin remained unchanged during this time. Re-incubation of these hypoxic cells for 24 h in normoxic conditions induced full recovery of the cells, and they were undistinguishable from those not exposed to hypoxia.

Fluorescence profiling of hypoxic HEK-293 cells expressing YFP-Occludin showed that the average contact enrichment factor of YFP-Occludin was 1.49 ± 0.13 (n=10 p < 0.0001 vs normoxic cells), this represented 61% of its otherwise normal average and was indicative of a decrease on its ability to interact in *trans* during hypoxia (**Fig. 19 B**).

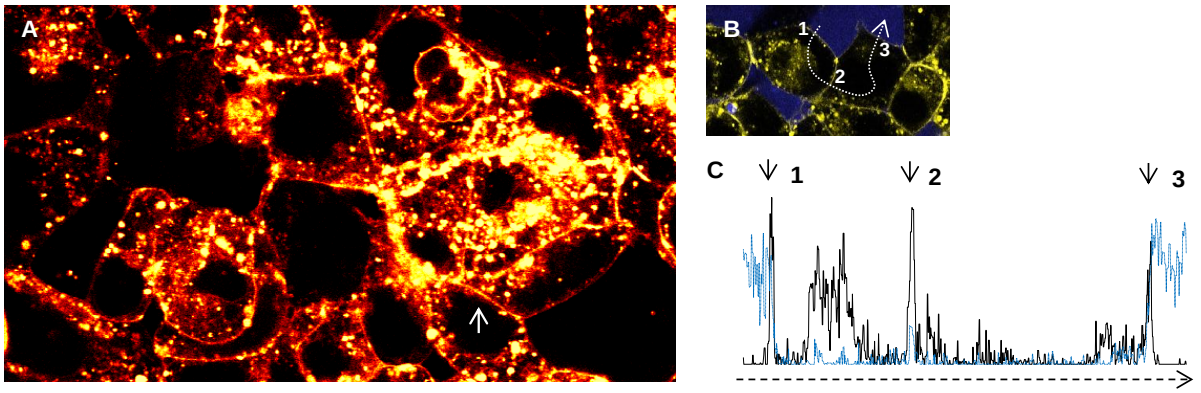

Fig. 19. Expression of YFP-Occludin in hypoxic HEK-293 cells.

A) YFP-Occludin was still found in the plasma membrane, but a large amount of it was intracellular. The arrow shows a cell-cell contact where enrichment can still be seen.

B and C). Fluorescence profiling of HEK-293 cells expressing YFP-Occludin. The horizontal arrow in C follows the same direction of the dotted arrow in B. The black profile corresponds to the YFP-Occludin fluorescence, and the blue profile shows the trypan blue signal. The YFP intensity at the point 2 (cell-cell contact) is comparable to that of points 1 and 3 (non-cell-cell contacts).

Digital substraction and analysis of the membrane and intracellular pools of YFP-Occludin showed that the average membranal ratio in hypoxic HEK-293 cells expressing YFP-Occludin was 1.08 ± 0.07 (n=10 p < 0.0001 vs normoxic cells). This indicated no preferential cytosolic or membranal location and represented 43% of the average ratio observed in normoxic HEK-293 cells expressing YFP-Occludin (**Fig. 20 A**). This was paired with a strong decrease of internalized trypan blue (**Fig. 20 B**).

Orthogonal reconstructions evidenced that, although YFP-Occludin was located at the cell-cell contacts, its enrichment was noticeably decreased and, contrasting with normoxic cells (**Fig 15**), no lateral-apical preferential expression was observed; instead, occludin was diffusely distributed along the whole lateral membranes with scarce enrichments (**Fig. 20 C**). To further analyze the expression pattern of YFP-Occludin during hypoxia, Triton X-100 extracts of hypoxic HEK-293 cells expressing YFP-Occludin were studied by F-PAGE. In normoxic cells, monomers and dimers were observed, but dimers were not seen in hypoxic cells (**Fig. 21**).

3.3.3 Effect of TNF-α and IFN-γ in the expression pattern of YFP-Occludin

Tumoral necrosis factor α (TNF-α) and interferon γ (IFN-γ) were separately used to increase the NADH content of HEK-293 cells expressing YFP-Occludin in normoxic conditions. A 3 h stimulation with TNF-α (200 ng/mL) increased the cellular NADH fluorescence from 665.5 ± 4.16 (unstimulated) to 700 ± 6.04 A.U, this increase approximated that of hypoxic cells (n=10 p < 0.001 vs. unstimulated cells, and < 0.1 vs hypoxic cells). On the other hand, after a 3 h stimulation with IFN-γ (200 ng/mL), the cellular NADH fluorescence was 685.5 ± 7.31 A.U, this value did not differ strongly from unstimulated cells and was significantly different from that of hypoxic cells (n= 10 p > 0.1 vs. unstimulated cells, and

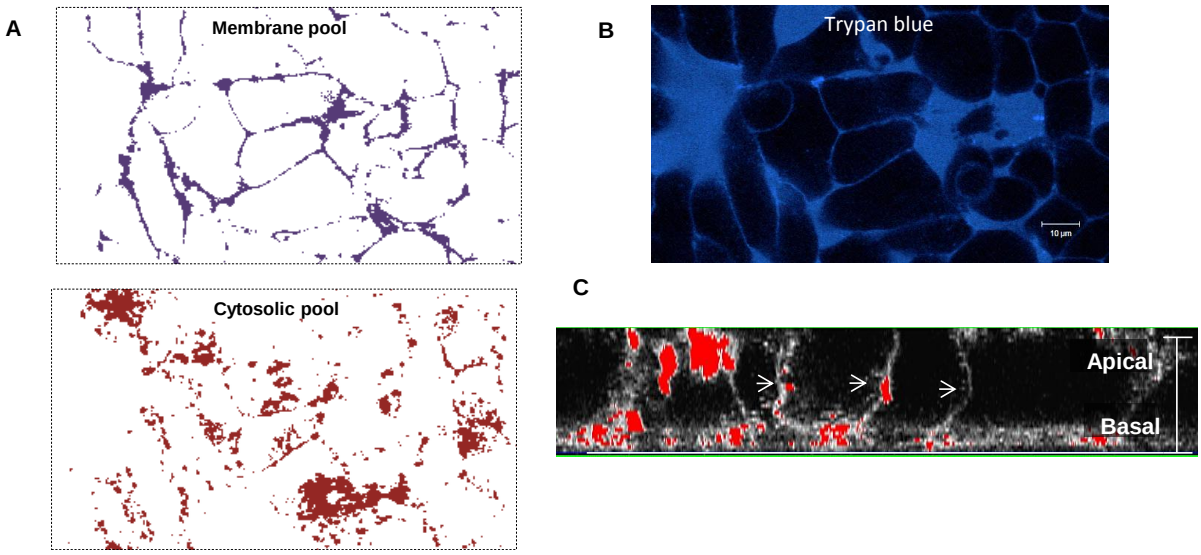

Fig. 20. The membranal ratio of YFP-Occludin, as well as its lateral-apical preferential expression at cell-cell contacts are altered during hypoxia.

A and B) The amount of occludin in the intracellular pool was similar to the membrane pool. It is noticeable the strong reduction in the amount of internalized trypan blue (B), compared to normoxic cells (shown in.**Fig. 14** and **Fig. 18B**)

C) The lateral-apical preferential localization of YFP-Occludin at cell-cell contacts (shown in **Fig. 15**). was lost during hypoxia. YFP-Occludin was diffusely distributed along the whole lateral membrane with non-specific enrichments (arrows).

<0.01 vs hypoxic cells). In those cells stimulated with TNF-α, YFP-Occludin was found largely intracellularly and exhibited an expression pattern that resembled that of hypoxic cells. Stimulation with IFN-γ did not induce noticeable changes in the expression pattern of YFP-Occludin when compared to normoxic unstimulated cells (**Fig. 22 A**). Digital substraction showed that the average membranal ratio for occludin expressed in cells treated with TNF-α was 0.64 ± 0.05, and 1.41 ± 0.14 for those treated with IFN-γ (n=10 p < 0.001). A higher amount of intracellular YFP-Occludin colocalizing with trypan blue was observed after stimulation with TNF-α than after stimulation with IFN-γ (**Fig. 22 B** arrows).

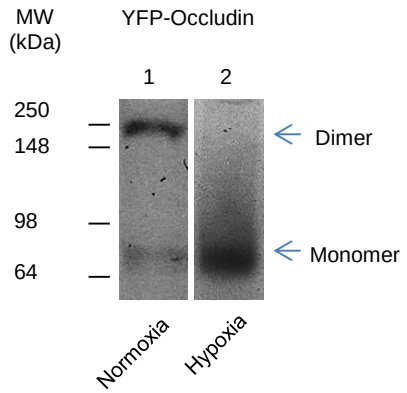

Fig. 21. Hypoxia prevents YFP-Occludin from dimerizing. Triton X-100 extracts of normoxic and hypoxic HEK-293 cells expressing YFP-Occludin were electrophoretically analyzed by F-PAGE. The dimeric band observed in normoxic conditions is absent in hypoxic cells.

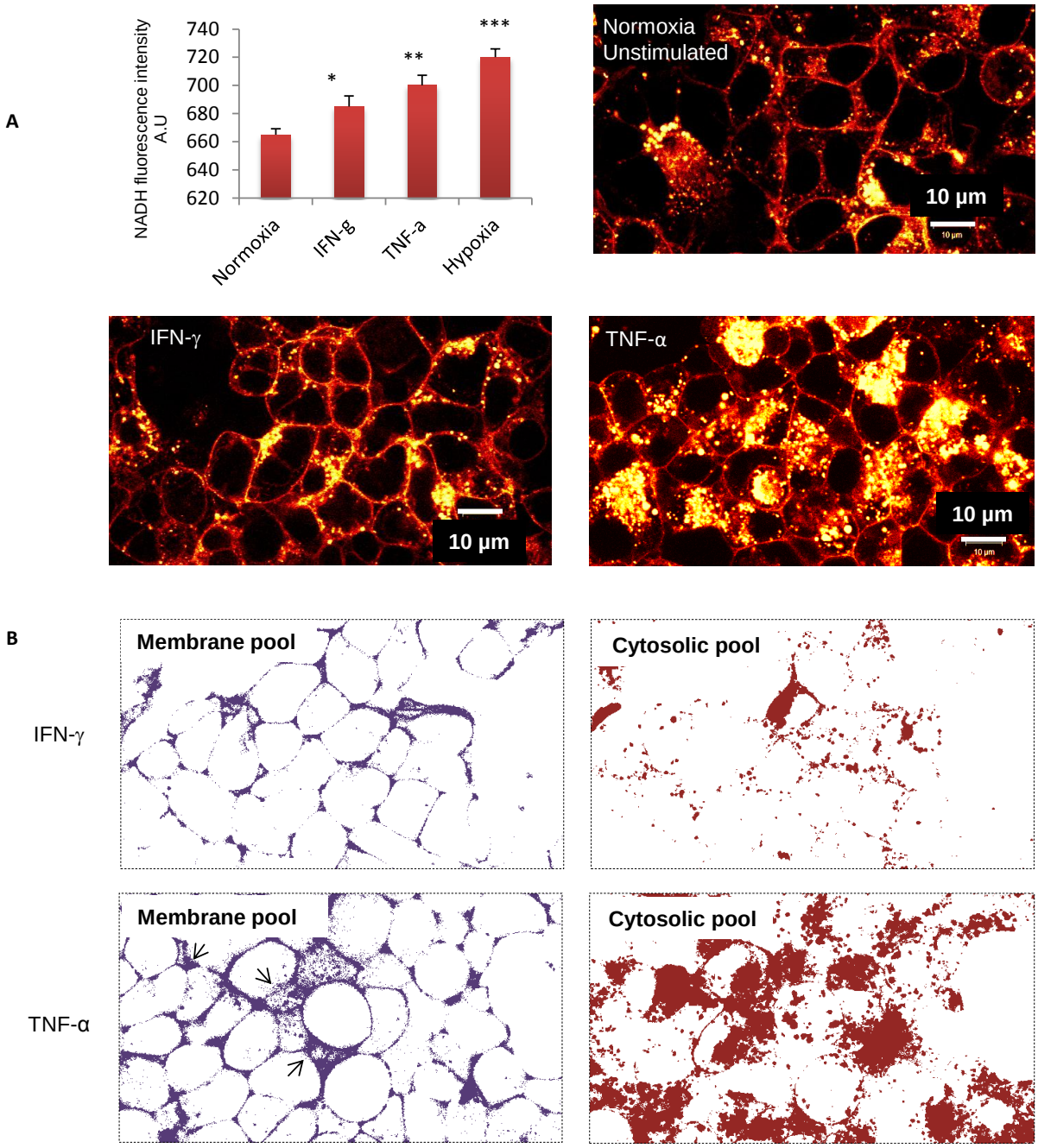

Fig. 22 Stimulation with TNF-α induced changes in the distribution pattern of YFP-Occludin.

A) The columns show the NADH fluorescence in HEK-293 cells expressing YFP-Occludin, and stimulated 3 h with 200 ng/ml of TNF-α, 200 ng/ml of IFN-α, or unstimulated during normoxia and hypoxia (*n*=10 * p<0.1, ** p>0.01, *** p<0.001). The expression pattern of YFP-Occludin expressed in HEK-293 cells was significantly altered (in comparison to normoxic unstimulated cells) after stimulation with TNF-α. The most evident changes were a strong increase in the intracellular YFP-Occludin and loss of enrichment at cell-cell contacts, resembling the effects of hypoxia. IFN-γ did not induce such changes. Error bars represent SEM.

B) Membrane and intracellular pools of YFP-Occludin expressed in normoxic HEK-293 cells stimulated with IFN-γ or TNF-α. The intracellular pool of YFP-Occludin in those cells stimulated with TNF-α was larger than in cells stimulated with IFN-γ. After TNF-α stimulation, some cells showed a higher amount of internalized YFP-Occludin colocalizing with trypan blue (arrows), compared with the cells stimulated with IFN-γ.

A comparison of the occludin membranal ratios and the amount of cellular NADH in unstimulated normoxic and hypoxic cells, as well as in normoxic cells stimulated with TNF-α or IFN-γ, is shown in **Fig. 23**.

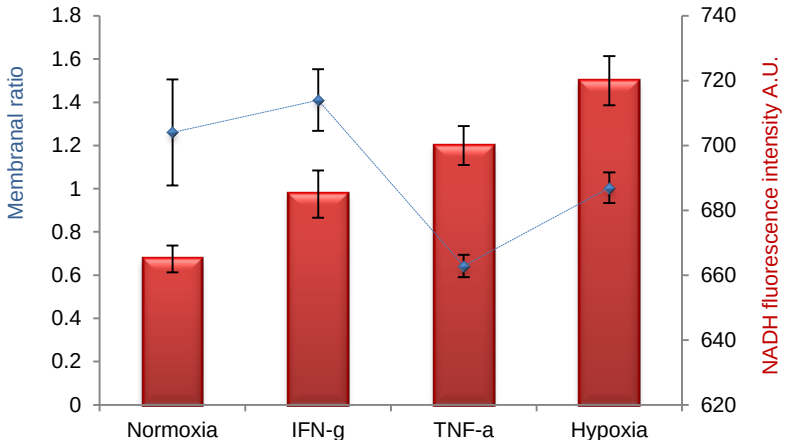

Fig. 23. Membranal occludin vs NADH content. The graph represents the YFP-Occludin membranal ratio (blue squares) plotted together with the total intracellular NADH content (red columns). The membranal ratios, for the case of normoxia and IFN-γ stimulation, did not differ statistically. Further increase of the cellular NADH level by TNF-α induced a strong inversion in the membranal ratio. Error bars represent SEM.

3.4 THE C-TERMINUS OF OCCLUDIN FORMS A DISULFIDE BRIDGE

The membrane-distal C-terminal domain of occludin is highly conserved among mammalians and has two cysteines. In human, these are the cysteines 409 and 500, and their potential role in forming an intermolecular disulfide bridge was analyzed.

Study of the crystallographic structure of the coiled-coil domain of human occludin (1XAW.PDB), revealed that the Cysteine^{500} was embedded in one of the alpha helical segments of the coiled-coil domain, and its reactive sulfur is masked by a neighboring helix that renders it unable to form a disulfide bridge (**Fig. 24 A**). Although the occludin fragment used to obtain the crystal contained the sequence between the lysine^{384} and tyrosine^{522}, only the fragment between the tryptophane^{416} and tyrosine^{522} showed crystalline packing (Li et al., 2005). This suggested that the fragment between the alanine^{383} and the aspartate^{415} was flexible. The cysteine^{409} is located in this flexible fragment and thus, was considered to be freely accessible to form a disulfide bridge (**Fig. 24 B**).

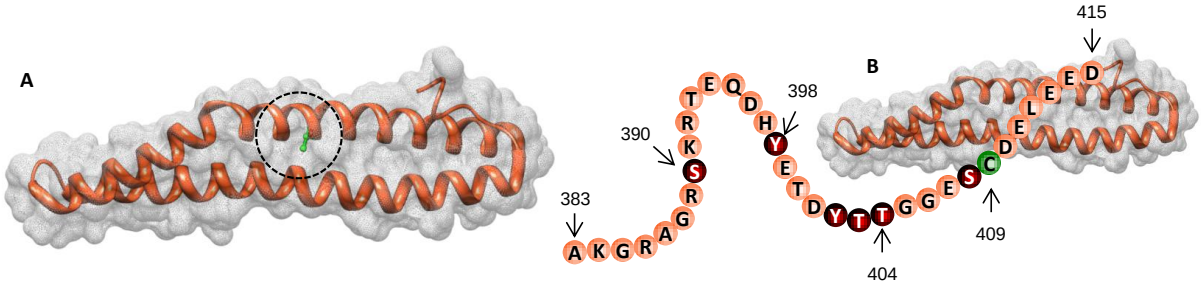

Fig. 24 Structure of the asymmetric unit of the crystalized occludin coiled-coil domain (1XAW.PDB). The molecular surface is shown as the white mesh wrapped around the brown coiled ribbon representing the helical trace of alpha-carbons shaped into a coiled-coil structure.

A) The lateral group of the Cysteine^{500}, highlighted with a dotted circle, extends towards the center of the structure and is masked by the neighboring helix that renders it unable to form a disulfide bridge.

B) The occludin fragment comprised between the alanine^{383} and the aspartate^{415} (AKG…EED) is shown. This fragment is considered flexible and contains five known phosphorylation sites at the positions 398, 402,403,404 and 408 (dark red - phosphorylation of the Ser^{390} is only predicted), before the cysteine^{409} (green); this cysteine may not be sterically blocked and may be available to form a disulfide bridge.

In order to determine whether the cysteine^{409} was indeed involved in the dimerization of occludin, a mutant, where the cysteine^{409} was substituted for alanine (YFP-Occludin^{C409A}), was generated and expressed in normoxic unstimulated HEK-293 cells. Triton X-100 extracts of these cells were analyzed by F-PAGE. In addition to the group of low-molecular-weight signals, only the 90 kDa (monomer) and higher order oligomeric bands, but not the 180 kDa band (dimer), were observed. To further analyze if only the cysteine^{409}, but not the cysteine^{500}, was involved in the dimerization of occludin, another two substitution mutants were generated: YFP-Occludin^{C500A} and YFP-Occludin$^{C409+500A}$, where respectively, the cysteine 500 or the cysteines 409 and 500 were replaced for alanine. F-PAGE analysis of Triton X-100 extracts of HEK-293 cells transfected with either of these two mutants showed that YFP-Occludin^{C500A} was able to dimerize, as indicated by the presence of the 180 kDa band, but YFP-Occludin$^{C409+500A}$ was found only as a monomer (**Fig. 25**).

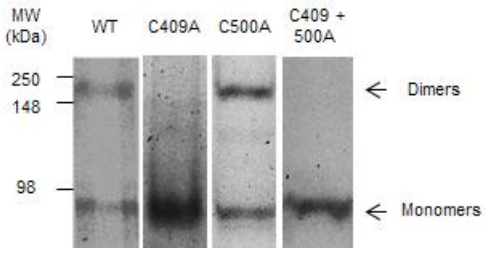

Fig. 25. The cysteine^{409} mediates the dimerization of occludin. F-PAGE of Triton X-100 extracts from HEK-293 cells expressing YFP-Occludin^{C409A} (C409A) showed monomers at approximately 90 kDa, but the dimeric band at 180 kDa was not seen. A mutation of the Cysteine500 (C500A) showed both, monomers and dimers, while the double mutant (C409+500A) showed only monomers. YFP-Occludin^{WT} (WT) showed both, monomers and dimers.

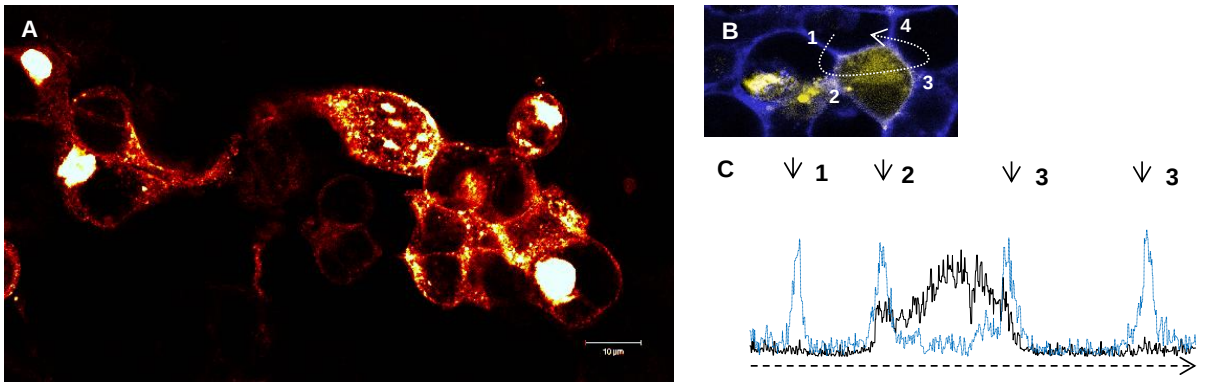

Fig. 26. Expression of YFP-Occludin^{C409A} in normoxic HEK-293 cells.

A) The protein was expressed mainly in the cytosol, but also reached the plasma membrane; no specific enrichment pattern was observed.

B and C). The fluorescence intensity of YFP-Occludin^{C409A}, measured across the path shown by the white arrow in B is shown in C (black). The trypan blue profile is shown in blue. The accumulation of YFP-Occludin^{C409A} in the cytosol is notorious, as well as the lack of enrichment at the plasma membranes, whose position is indicated by the small vertical arrows labeled 1 – 4. The profile is drastically different from that of HEK-293 cells expressing YFP-Occludin^{WT} (Fig. 12), where the majority of the YFP signal is at the plasma membrane. In addition, the trypan blue signal is more intense at the positions where the plasma membranes were located, this behavior was not seen in normoxic cells expressing YFP-Occludin^{WT} (Fig. 12)

3.5 THE MEMBRANAL LOCALIZATION OF OCCLUDIN CORRELATES WITH ITS ABILITY TO DIMERIZE

HEK-293 cells expressing YFP-Occludin^{C409A} and cultured under normoxic conditions were analyzed by confocal microscopy. YFP-Occludin^{C409A} was found mainly in cytosolic compartments, but was still able to reach the plasma membrane (**Fig. 26**). Fluorescence profiling showed that this mutant had a contact enrichment factor of 0.82 ± 0.08 (n=10 $p < 0.0001$ vs WT), indicating that it lost its ability to interact in trans (**Fig. 26 B and C**). Digital substraction showed that YFP-Occludin^{C409A} had a preferential intracellular expression with an average membranal ratio of 0.46 ± 1.14 (n= 10 $p < 0.0001$) (**Fig. 27 A and B**). Orthogonal reconstructions showed that this occludin mutant was randomly distributed in the cell surface without preferential localization in the apical half of the lateral membrane at cell-cell contacts (**Fig. 27 C**).

Further microscopical analysis was performed in HEK-293 cells expressing the mutants YFP-Occludin$^{C409+500A}$ or YFP-Occludin^{C500A}, and cultured in normoxia. YFP-Occludin^{C500A} was found mainly in the plasma membrane. YFP-Occludin$^{C409+500A}$, in contrast, was predominantly expressed intracellularly, with low amounts in the plasma membrane, and no specific membrane enrichment patterns (**Fig. 28**).

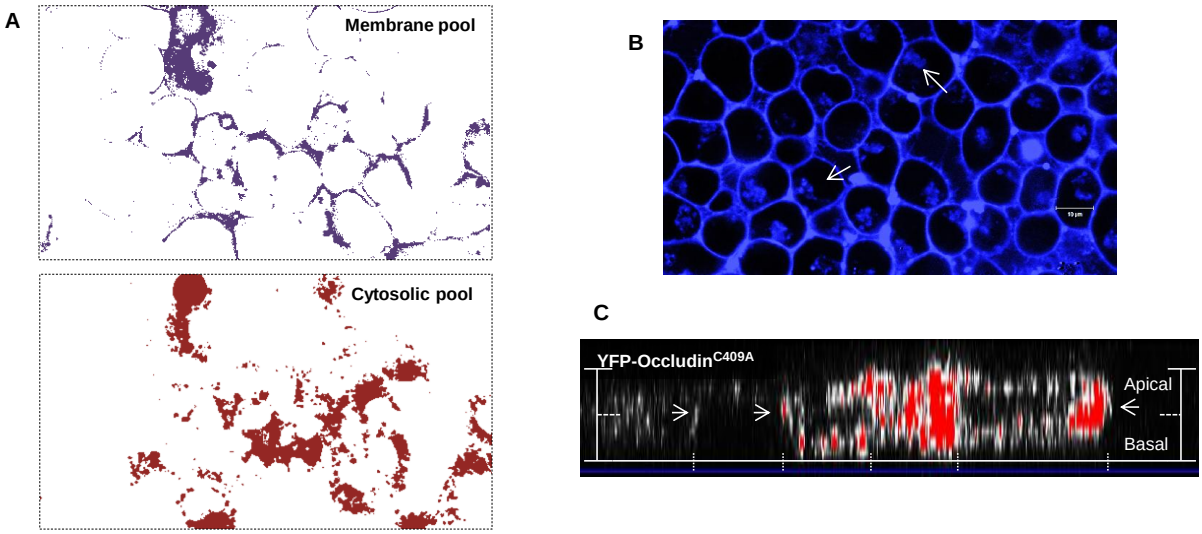

Fig. 27. The membranal ratio of YFP-Occludin^{C409A} expressed in HEK-293 cells, as well as its distribution at cell-cell contacts, resembles the behavior of YFP-Occludin^{WT} during hypoxia.

A and B) The intracellular pool of YFP-Occludin^{C409A} was larger than the membrane pool. The average membranal ratio was 0.44. B) shows internalized trypan blue in HEK-293 cells expressing YFP-Occludin^{C409A} (arrows). Mostly, the membrane pool contains occludin colocalizing with intracellular trypan blue.

C) Orthogonal reconstruction of the YFP-Occludin^{C409A} expression in HEK-293 cells, showing a random distribution and unspecific enrichment. The position of the cell-cell contacts is shown by the vertical lines at the bottom of the image; the horizontal arrows mark the expression of YFP-Occludin^{C409A} at the cell cell contacts. No preferential lateral-apical expression was observed. (as with YFP-Occludin^{WT} in **Fig. 15**)

3.5.1 YFP-Occludin^{C409A} does not associate with YFP-Occludin^{WT}

In order to determine if the dimerization potential of YFP-Occludin^{C409A} was lost at the plasma membrane, fluorescence resonance energy transfer (FRET) assays were performed in normoxic HEK-293 cells co-expressing YFP-Occludin^{C409A} and CFP-Occludin^{WT}, and the FRET efficiency compared to that of a YFP/CFP pair of wild-type occludin. The average corrected energy transfer efficiency (E_c) for YFP-Occludin^{WT} and CFP-Occludin^{WT}, when expressed in normoxic HEK-293 cells, was 8% ± 0.02, and -1% ± 0.005 (no energy transfer) for CFP-Occludin^{WT} vs YFP-Occludin^{C409A} (**Fig. 29**).

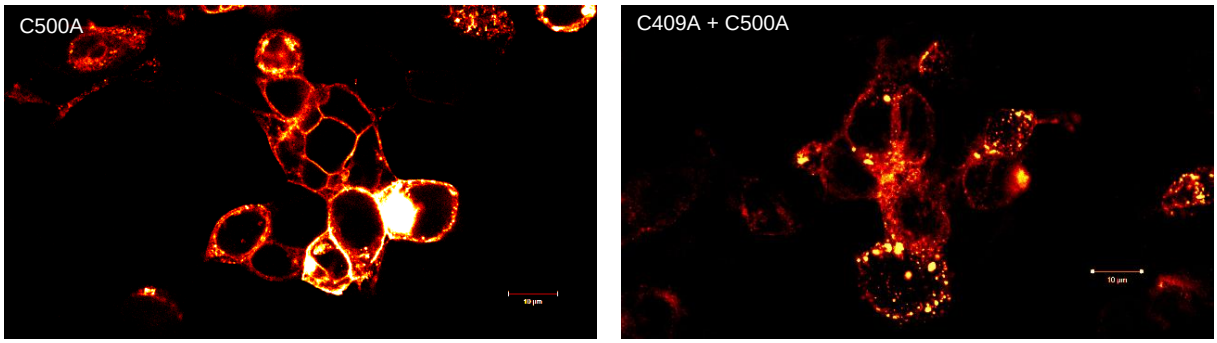

Fig. 28. Expression of YFP-Occludin^{C500A} or YFP-Occludin$^{C409+500A}$ in normoxic HEK-293 cells. While the substitution of the cysteine 500 for alanine (C500A) did not induce noticeable changes on the enrichment pattern of the molecule at cell-cell contacts, introduction of the additional C409A mutation drastically reduced the membranal localization of occludin.

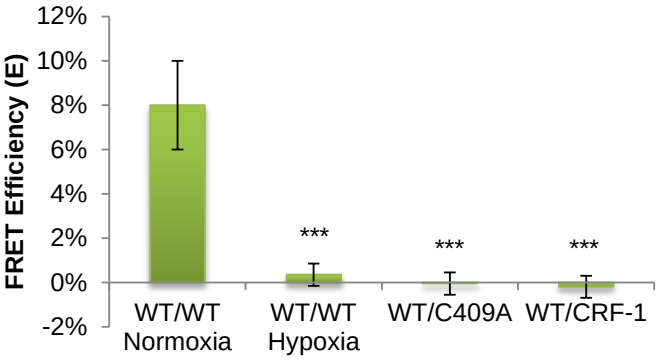

Fig. 29. Occludin self-interacts only in normoxia and if it is able to dimerize. The graph shows the interaction between CFP-Occludin^{WT} and YFP-Occludin^{WT} (WT/WT) in normoxia and hypoxia, or CFP-Occludin^{WT} and YFP-Occludin^{C409A} (WT/C409A). The average energy transfer efficiencies calculated by qλ-FRET plus standard error of mean are shown. The energy transfer between YFP-Occludin^{WT} and an unrelated molecule (Corticotropin releasing factor receptor 1-CFP) (WT/CRF-1) is shown as a negative control. *n*=10. *** $p < 0.001$. Error bars represent SEM.

3.6 THE INTERACTION OF OCCLUDIN WITH ZO-1 IS SENSITIVE TO THE ABILITY OF OCCLUDIN TO DIMERIZE.

To determine whether the dimerization of occludin had further biological effects, the interaction of ZO1 and Occludin was investigated. HEK-293 cells were cotransfected with ZO1-CFP and YFP-Occludin^{WT} or YFP-Occludin^{C409A}. The cells were then incubated in normoxic and in hypoxic conditions, and the expression pattern of the fluorescently labeled proteins was analyzed by confocal microscopy.

3.6.1 ZO-1 CFP IS EXPRESSED MAINLY IN THE CYTOSOL OF HEK-293 CELLS

Normoxic HEK-293 cells transfected with ZO1-CFP alone, expressed the protein mainly in the cytosol excluding the cell nuclei. Only small amounts of ZO-1 associated with the cell membrane, where it did not show any specific enrichment. In addition, ZO-1 was not observed in any intracellular compartment colocalizing with trypan-blue. When the cells were cultured under hypoxia, ZO-1 was found mostly in the cell nuclei (**Fig. 30**).

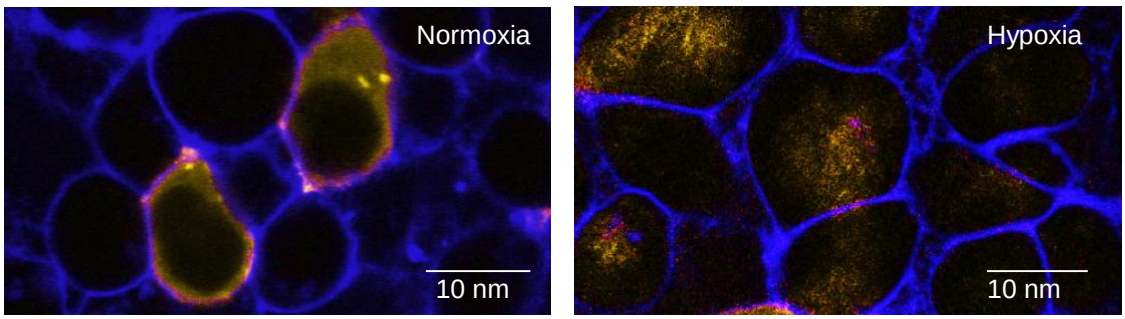

Fig. 30. The subcellular localization of ZO-1 CFP in HEK-293 cells changes during hypoxia. Hypoxia induced redistribution of ZO-1 from the cytosol to the nucleus. The blue signal corresponds to trypan blue staining. For visualization convenience, ZO1-CFP is shown here in yellow. Colocalization of ZO-1 and trypan blue is shown in purple

3.6.2 ZO-1 CFP REACHES THE PLASMA MEMBRANE IF COEXPRESSED WITH YFP-OCCLUDIN

The effect of occludin on the behavior of ZO-1 was assessed in HEK-293 cells. When coexpressed with YFP-Occludin^{WT}, ZO-1 CFP was found in the plasma membrane where both molecules colocalized (**Fig. 31 A**). ZO1-CFP was particularly enriched in rounded particles associated with the

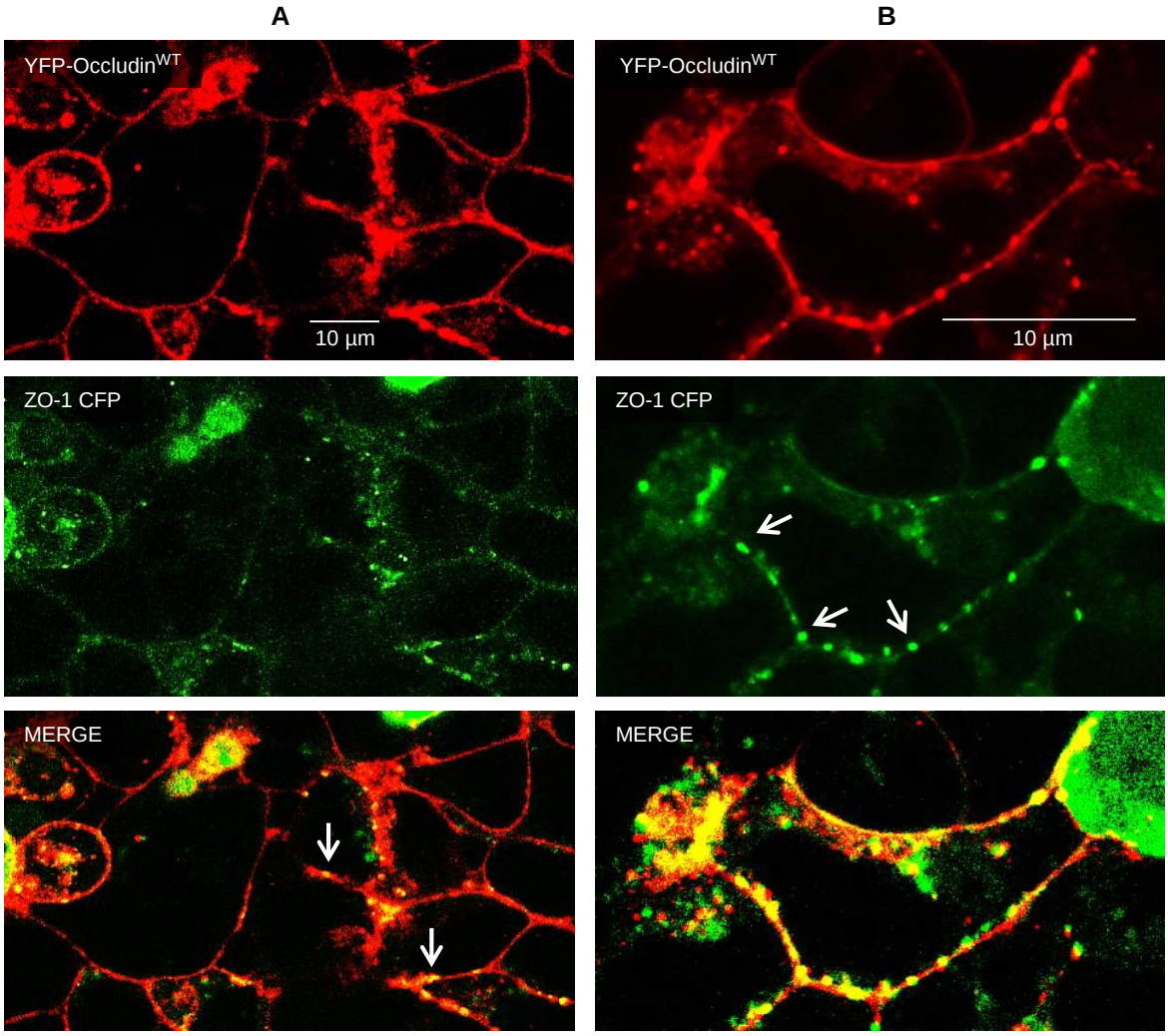

Fig. 31. YFP-Occludin^{WT} and ZO-1 CFP colocalize when coexpressed in normoxic HEK-293 cells.

A) Both molecules were found mainly in the plasma membrane. The merge image shows in orange to yellow scale the amount of colocalization. Yellow represents areas with the hightest colocalization. Notice the many yellow “dots” in proximity to the plasma membrane (arrows).

B) Zoomed detail of the membranal particulated colocalization of ZO1-CFP and YFP-Occludin^{WT}. The arrows show particulated aggregates associated with the plasma membrane, where both molecules colocalized. (The image corresponds to another field not shown in A)

plasma membrane, where strong colocalization with YFP-Occludin^{WT} existed (**Fig. 31 B arrows**), the nature of these particles was not investigated.

3.6.3 HYPOXIA DISSOCIATES ZO1-CFP AND YFP-OCCLUDIN^{WT}

When HEK-293 cells coexpressing CFP-ZO1 and YFP-Occludin^{WT} were cultured for 3 h in hypoxic conditions, not only the subcellular localization of YFP-Occludin^{WT} was changed, resembling the distribution of YFP-Occludin^{WT} expressed alone in hypoxic HEK-293 cells, but also the expression of ZO-1 was shifted from the membrane to a diffuse cytosolic distribution and also to the cell nuclei.

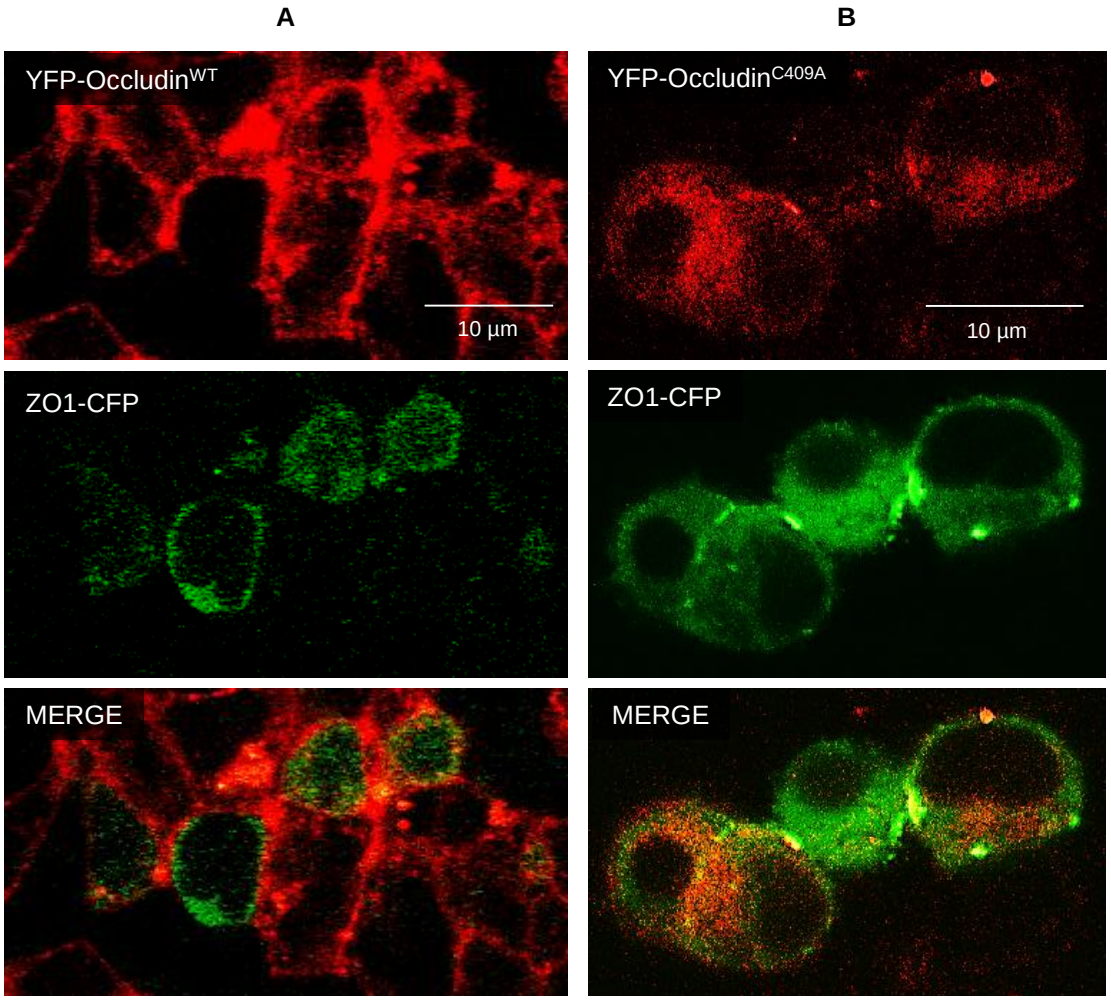

Fig. 32 ZO-1 and Occludin do not associate if occludin cannot dimerize

A) HEK-293 cells co-expressing YFP-Occludin^{WT} and ZO1-CFP during hypoxia. Both molecules dissociated, ZO1-CFP can be seen away from the plasma membrane and in the cell nuclei. YFP-Occludin^{WT} was retrieved from the plasma membrane and was seen mostly in the cytosol, as it happened when it was expressed alone in hypoxic HEK-293 cells. The colocalization of both molecules was rather poor.

B) HEK-293 cells co-expressing YFP-Occludin^{C409A} and ZO1-CFP in normoxia. Only small amounts of both molecules reached the plasma membrane. Both molecules followed the same behavior as when they were expressed separately in normoxic HEK-293 cells.

Although colocalization between ZO-1 and occludin was observed in some cytosolic aggregates and in membranal regions where YFP-Occludin^{WT} was still present, the main appearance was that both molecules, dissociated and were retrieved from the plasma membrane during hypoxia (**Fig. 32 A**).

3.6.4 YFP-Occludin^{C409A} is unable to recruit ZO1-CFP to the plasma membrane

In order to determine if the dissociation of occludin and ZO-1 during hypoxia was due to the loss on the ability of occludin to dimerize, the behavior of ZO1-CFP, when coexpressed with the non-dimerizing occludin mutant YFP-Occludin^{C409}, was analyzed in normoxic HEK-293 cells. A diffuse intracellular expression of ZO-1 was found, excluding the cell nuclei and with minimal membrane localization. YFP-Occludin^{C409A} showed a distribution that resembled its single expression in HEK-293 cells (**Fig. 32 B**). FRET analysis of ZO-1 CFP and YFP-Occludin^{C409A} coexpressed in normoxic HEK-293 cells revealed that, although some colocalization was found between ZO1-CFP and YFP-Occludin^{C409A}, the molecules did not interact. In contrast, ZO1-CFP and YFP-Occludin^{WT}, coexpressed in the same conditions, interacted with each other and showed FRET with an average of 24% (**Fig. 33**).

3.7 The dimeric assembly of the occludin coiled-coil domain.

To further characterize the role that the disulfide bridge mediated by the cysteine^{409} would play in the interaction of ZO-1 and occludin, the structural basis of this interaction was studied. The potential

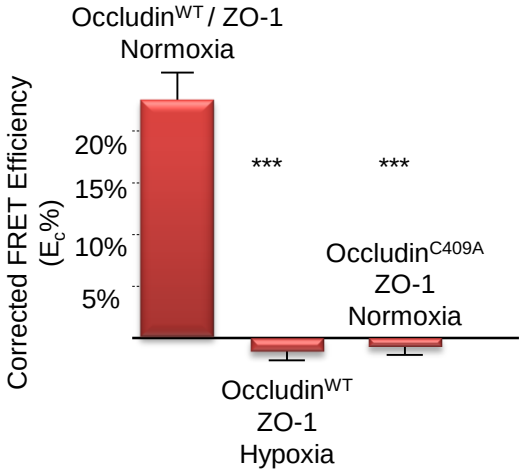

Fig. 33. The ability of occludin to dimerize has an impact in the ZO1 / Occludin interaction. The graphs shows the average FRET efficiency of the interaction of YFP-Occludin^{WT} and ZO1-CFP (24% in average) when co-expressed in normoxic HEK-293 cells. This interaction was lost if the cells were cultured in hypoxia. YFP-Occludin^{C409A} was unable to interact with ZO1-CFP if both molecules were coexpressed in normoxic HEK-293 cells. n=10 *** p<0.001. Error bars represent SEM.

oligomeric assemblies and binding interfaces of the coiled-coil domain of occludin (1XAW.PDB – fragment 384-522) were identified. Six assemblies were found, leading to the formation of dimers but not higher order oligomers; their features are shown in **table 1**.

Table 1. Thermodynamical features of the six possible dimeric assemblies of the coiled-coil domain of occludin

Assembly #	Monomer 1 Interfacing residues	Monomer 2 Interfacing residues	Interfacing Area Å^2	Δ^iG kcal/mol	P-value	Hydrogen bonds	Saline Bridges
1	31	31	945.7	-7.1	0.253	7	6
2	13	13	493.3	-5.1	0.214	4	None
3	10	10	358.9	5.4	0.919	12	2
4	5	7	277.0	-1.2	0.436	3	4
5	5	3	160.7	0.9	0.682	4	5
6	4	3	110.0	1.9	0.744	2	None

Monomers 1 and 2 refer to the **two interfacing structures** in monomeric form. In this case both are the same molecule situated in different positions within the crystal.

The interfacing areas were calculated as the difference of the total solvent accessible surface areas between the isolated and the interfacing monomers divided by two. Δ^iG is the free energy of binding. The P value indicates how hydrophobic the bindings are; a P > 0.5 indicates less hydrophobic assemblies and implies a crystal packing artifact, while P < 0.5 indicate that the molecular binding is more hydrophobic and is likely to be interaction-specific. The assembly # 1 had a high hydrophobic specificity (P=0.253) and the lowest Δ^iG (-7.1 kcal·mol^{-1}); thus, it was considered the most likely occurring structure; it was formed by two symmetrically located, antiparallel coiled-coil monomers, predicted to be bound by seven hydrogen bonds and six saline bridges (**Fig. 34**); its total solvent accessible surface had an area of 13540 Å^2, and its interacting interface was formed by 31 amino acids (per monomer), accounting for a buried surface of 945.7 Å^2 (per monomer). The predicted amino acids forming hydrogen bonds and salt bridges in this assembly are shown in **table 2**.

Table 2. Predicted hydrogen bonds and saline bridges in the assembly # 1

HYDROGEN BONDS			**SALINE BRIDGES**		
Monomer 1	Distance in Å	Monomer 2	Monomer 1	Distance in Å	Monomer 2
LYS 433	2.82	GLU 480	LYS 433 (2x)	2.82 and 3.10	GLU 480
GLN 441	2.90	GLU 456			
SER 448	3.38	SER 448			
ARG 459	3.85	ASP 437	ARG 459	3.85	ASP 437
GLU 480	2.82	LYS 433	GLU 480 (2x)	2.82 and 3.10	LYS 433
GLU 456	2.90	GLN 441			
ASP 437	3.85	ARG 459	ASP 437	3.85	ARG 459

The $\Delta^{i}G$ upon the formation of the binding interfaces approximated -3.5 kcal·mol^{-1} per monomer (accounting for the -7.5 kcal·mol^{-1} of the dimeric assembly). This value, being negative, indicated that the dimerization process would be energetically favorable; however, the dissociation energy (ΔG^{diss}) of the dimer was -0.1 kcal·mol^{-1}. The negative ΔG^{diss} indicated that the complex was thermodynamically unstable; hence, an additional source of energy would be required to maintain the structure in its dimeric form. In these conditions, a covalent bond located in close proximity to the coiled-coil domain would provide enough energy to maintain the structure dimerized. A disulfide bridge would contribute with additional -4 kcal/mol to the $\Delta^{i}G$ of the dimer, and its ΔG^{diss} of 62.6 kcal·mol^{-1}, markedly positive, would allow this bond to maintain the structure dimerized.

To evaluate whether the geometry of the dimeric coiled-coil domain of occludin would allow the formation of a disulfide bridge based on the cysteine^{409}, the distance between the N-terminal ends of each of the monomers was measured and compared with the length of the stretch of amino acids comprised between these ends and the cysteines^{409}. The two tryptophanes^{416} at the N-termini of the coiled-coil domain are located in opposite sides of the assembly, and are separated by 45.11 Å (**Fig. 34**). The theoretical distance between two amino acids, measured from one alpha carbon to the next one, is 3.89Å. The average measured length between two consecutive alpha carbons in the coiled-coil dimer was 3.8 Å. There are seven peptide bonds separating the cysteine^{409} from the triptophane^{416} (**Fig. 24-B**), thus the stretch from the cysteine^{409} to the aspartate^{415} should have an approximate length of 26.6 Å per monomer, providing that no loops or high angle turns are formed, indicating that this stretch has the proper length to allow both cysteines to approximate each other on top of the model (**Fig. 34 D and E**).

3.8 OCCLUDIN DOCKS INTO A NOTCH IN THE SH3-HINGE-GUK UNIT OF ZO1

In order to understand the binding of ZO-1 and occludin in structural terms, the binding regions of occludin and ZO-1 were identified in the molecular surface maps of the corresponding molecules. The known occludin and ZO-1 interacting regions (according to **Mueller et al., 2005**) are shown in table 3:

Table 3. Known binding regions between occludin and ZO-1

Occludin regions binding to ZO-1$^{597\text{-}633\ (Hinge)}$	Occludin regions binding to ZO-1$^{745\text{-}772\ (GuK)}$
400-433	400-433
452-485	445-487
480-521	

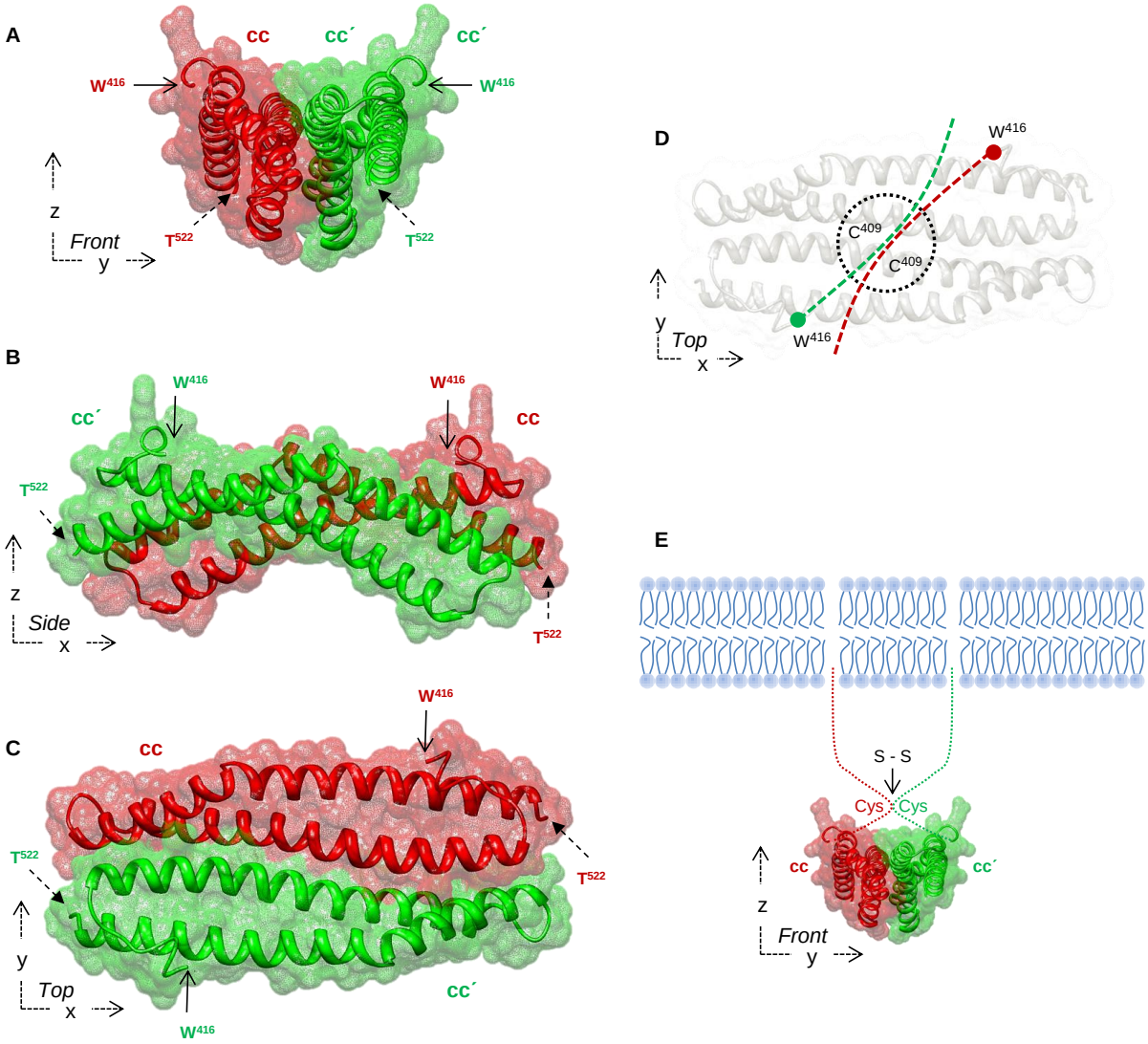

Fig. 34. Tridimensional structure of the predicted dimer of the coiled-coil domain of occludin. The dimeric assembly is flat, elongated, and forms and arch with a concavity looking downwards when seen from the side.

A, B and C) Top, side and frontal views. These positions, as well as the X,Y,Z orientations were arbitrarily selected but are consistent across all models. Each monomer is colored in red or green, the surface is shown as a semitransparent mesh. cc and cc´ identify each of the monomers. The triptophane^{416} (W^{416}) is the N-terminal amino acid of the monomers. The threonine^{522} (T^{522}) is located at the C-terminal end. The distance between the alpha carbons of the two triptophanes^{416} is 45.11Å.

D and E) Presumed spatial position of disulfide bridge mediated by the cysteine^{409}. Considering the length of the stretch between the two triptophanes^{416} (big red and green dots), and the length of the amino acid chains that span from those ends, the disulfide bridge should form in the region limited by the dotted circle, situated at the top-center of the dimer. The frontal view shows the presumed relative position of the dimeric coiled-coil domain, the disulfide bridge, and the plasma membrane.

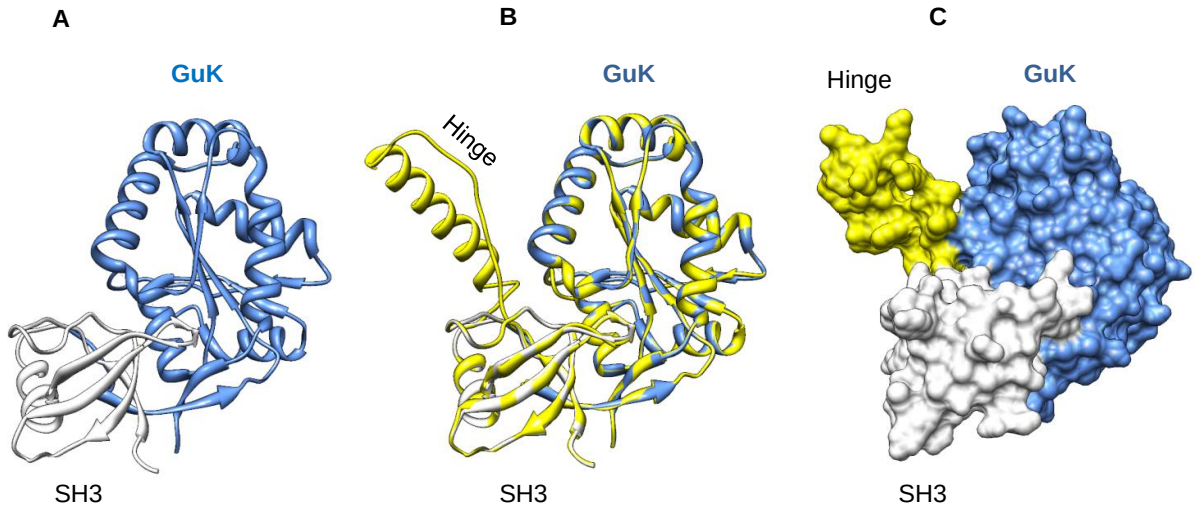

Fig. 35. Structure of the SH3-Hinge-GuK unit of ZO-1

A) The crystal structure of the fragmented SH3-GuK region of ZO-1 (3LH5.PDB) The SH3 domain (aa 515-584) is shown in white and the GuK$^{626-803}$fragment in blue. The hinge region (aa 589-625) and a short fragment inside the GuK domain (aa 684-686) are missing from the structure.

B and C) Based on the 3LH5 crystal an hybrid model was created (yellow). This model incorporates the hinge region and the complete GuK domain. B) The hybrid model and the crystal structure (blue and white) are shown superimposed. Aside from the missing fragments in the crystal, no spatial differences can be seen. C) Shows the surface of the SH3-Hinge-GuK hybrid model of ZO-1

The crystal structure of the ZO-1$^{516-803\Delta\mathbf{589-625}}$ fragment (3LH5.PDB) includes the SH3 and most of the GuK unit, but not the hinge region. Since the hinge region of ZO-1 is known to form a large binding surface for occludin, the whole ZO-1$^{516-766}$ fragment was re-modeled based on the 3LH5 crystal structure. The resulting hybrid structure is shown in **Fig. 35**.

A Ramachandran plot showed that 89.9% of residues of the hybrid model were in the most favored regions, 8.9% in additional allowed regions, 1.2% in generously allowed regions, and none in disallowed regions, thus it was considered to have an acceptable folding.

Using the dimeric model of the coiled-coil domain of occludin, the hybrid model of the SHG unit of ZO1, and considering the interacting regions of both molecules, a structural protein-protein interaction map for occludin and ZO-1 was generated. The occludin fragment 452-487 is known to bind both, the hinge fragment 597-633 and the GuK fragment 745-772; structurally, the only place where this could occur simultaneously is in a notch formed by these two domains, thus the coiled coil domain of occludin was positioned in that pocket, and the molecules were oriented, considering the sterical limitations that each model imposed on the other (**Fig. 36 A and B**).

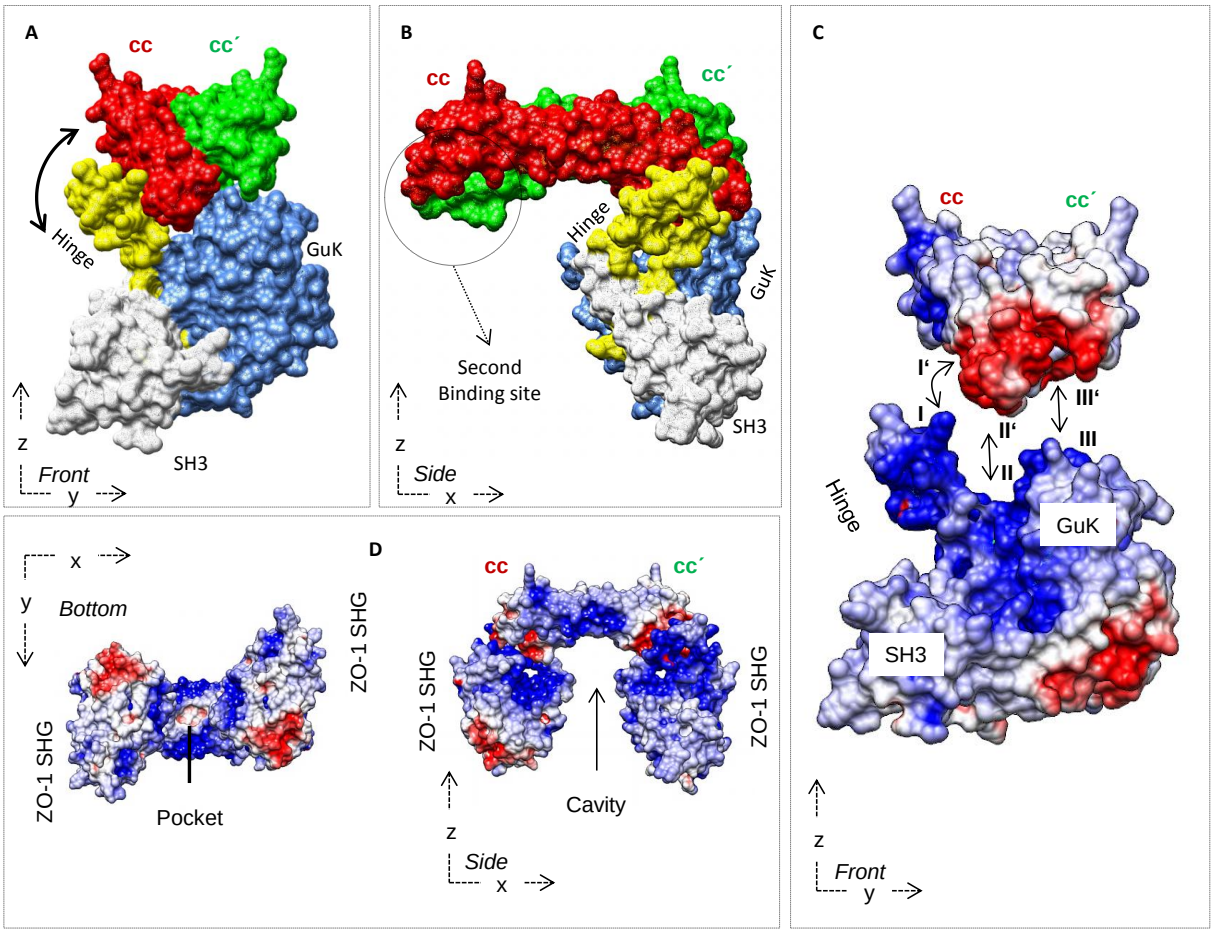

Fig. 36. The occludin/ZO-1 interaction model. The model was based on the known interacting areas for both molecules, and refined calculating their electrostatic surface potentials. It is composed of the dimeric coiled-coil domain of occludin associated by its lateral inferior surfaces with the monomeric SHG units of two ZO-1 molecules.

A and B) The dimeric coiled-coil domain of occludin (red/green) rests in the notch formed by the hinge (yellow) and GuK (blue) domains of the SHG unit of ZO-1. The possible mobility range of the hinge region is depicted by the curved arrow; the flexibility of this region could facilitate the binding of both molecules. A second binding site for the Hinge-GuK domain is encircled.

C) The model shows the electrostatic surface charge distribution on both the SHG unit of ZO-1 and the dimeric coiled-coil domain of occludin. The notch in the SHG unit of ZO-1, where occludin binds, is markedly positive (blue). All electronegative surfaces (red) are facing downwards, away from the occludin interacting region. The lateral-inferior surface of the dimeric coiled-coil of occludin is electronegative, and complements the charge of the notch in the SHG unit (binding pocket) of ZO-1. The binding model features three spatial landmarks on the SHG unit of ZO-1 (I, II and III); they are complimentary to the inferior surface of the coiled-coil domain (I' II' and III') - described in the text.

D) Side and bottom views of the model. The two SHG units bound to the dimeric coiled-coil domain of occludin are separated by a wide volume that forms a cavity, at the top of this cavity there is a small electronegative pocket in the inferior face of the dimeric coiled-coil domain.

The intensity of the colors correlates with the electrostatic charge intensities. Neutral regions are white. CC and CC´ correspond to each of the monomeric coiled-coil domains in the complex.

To refine the binding model, electrostatic potential surface maps were generated for both models and represented on their surface. The lateral ends of the dimeric coiled-coil domain of occludin were markedly electronegative on their inferior aspect, while the inferior middle region was strongly positive; these areas, showed diagonal symmetry and were limited by a near-to-neutral border. For the SHG unit, the whole region where the interaction with occludin occurs was markedly positive. Since the two lateral ends of the coiled-coil domain are symmetrical and share the same electrostatic charge, the dimeric coiled-coil domain was aligned against the positive top surfaces of two ZO1-SHG units, so the electrostatic surface distribution between the three models was complimentary. The resulting model is shown in **Fig. 36 C**. After binding the coiled-coil domain of occludin to the SHG units of two ZO-1 molecules, a large cavity was formed. The walls and the roof of such space were either neutral or positive, and the top of such cavity was riveted by a small electronegative pocket in the inferior aspect of the dimeric coiled-coil domain of occludin (**Fig. 36 D).**

Three spatial landmarks on the Hinge and GuK domains of ZO-1 were also identified: **I**) A set of two prominences formed by the lateral groups of the lysine^{616} and arginine^{618} on the hinge region, that could serve as a steric guide to position the coiled-coil domain of occludin **II**) the bottom of the hinge-GuK notch formed by the pairs leucine^{621}(hinge) and lysine^{763}(GuK), and histidine^{759}(hinge) and glutamate^{619}(GuK), that could determine how deep the coiled-coil domain could fall into the notch, and **III**) A set of prominences formed by the lateral groups of the, lysine^{733}, glutamate^{734}, lysine^{737}, and arginine^{752} on the GuK domain, that match the groove formed between the two coiled-coil domains.

The main features of the proposed occludin/ZO-1 model were: **1)** The coiled-coil domain of occludin dimerized **2)** Seven aminoacids in the coiled-coil domain presumably interacted; however, the Lys^{433} and Glu^{480} formed two saline bridges and an hydrogen bond with each other, likely having prominent role in the dimerization of occludin, **3)** The dimeric coiled-coil domain was stabilized by a disulfide-bridge mediated by the cys^{409}, and **4)** the two electronegative lateral ends of the dimeric coiled-coil domain of occludin docked into the strong electropositive notch formed between the hinge and GuK domains of two ZO-1 molecules forming and heterotetramer.

3.9 OCCLUDIN FORMS STRANDS IF IT CAN DIMERIZE AND ONLY IN PRESENCE OF ZO-1

The self-association capacity of the SHG unit of ZO-1 has been recently described (**Müller et. al. 2005**). Although the spatial localization of the SHG units in the occludin/ZO-1 interaction model prevents them from directly interact with each other, in the occludin/ZO-1 model, the SHG units could still associate by aligning their electronegative and electropositive faces sidewards between two occludin/ZO-1 heterotetramers, forming a polymeric occludin/ZO-1 structure.

To explore the polymerization of occludin in the plasma membrane, in the presence or absence of ZO1, freeze-fracture electron microscopy studies were performed in HEK-293 cells expressing both molecules (performed in cooperation with Susanne Krug – Charité Berlin).

HEK-293 cells coexpressing occludin and ZO-1 showed long (3-5 µm), sinuous, single threaded strands that did not branch to form networks. When these occludin/zo-1 expressing cells were cultured in hypoxia (preventing occludin dimerization) no strands were observed. Furthermore, the single expression of occludin^{WT}, occludin^{C409A} or the coexpression of occludin^{C409A} with ZO-1, in normoxia, did not result in the formation of strands. (**Fig. 37**).

3.10 The C-terminal domain of occludin is predicted to have structural similarities to oxidoreductases.

A theoretical model of the occludin fragment$^{266-415}$, including the membrane proximal C-terminal domain until immediately before the coiled-coil domain, was generated using I-TASSER. The crystallographic templates used to generate the model were tropomyosin (2TMA chain A), the 50S ribosomal protein L10 (2JL6 chain J), the extracellular domain of the LDL receptor (1N7D chain A), the

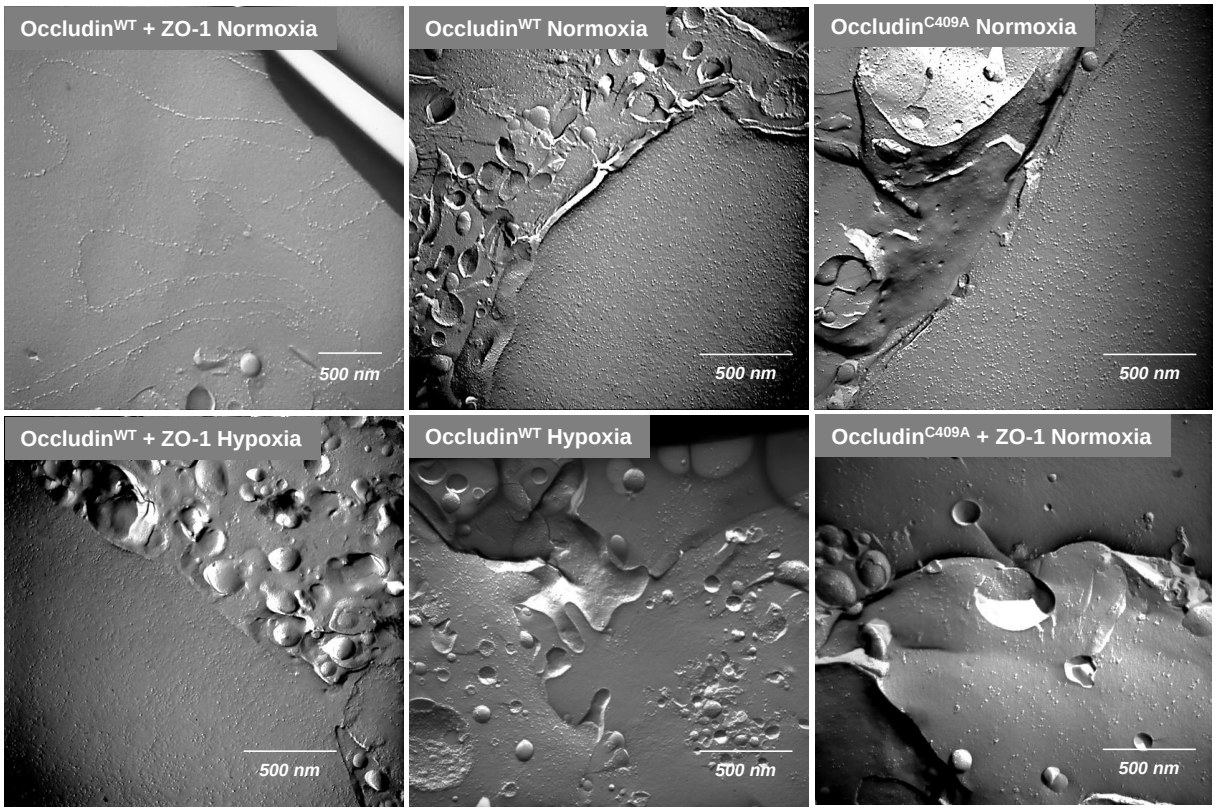

Fig. 37. YFP-Occludin^{WT} forms strands when coexpressed with ZO1-CFP in normoxic HEK-293 cells. In freeze fracture electron microscopy, strands were found only when occludin and ZO-1 were coexpressed in normoxic cells. Hypoxia prevented strands from being formed. YFP-Occludin^{WT} by itself was unable to form strands, and the non-dimerizing occludin mutant C409A was also unable to form strands, even if coexpressed with ZO-1. Untransfected HEK-293 cells did not show strands.

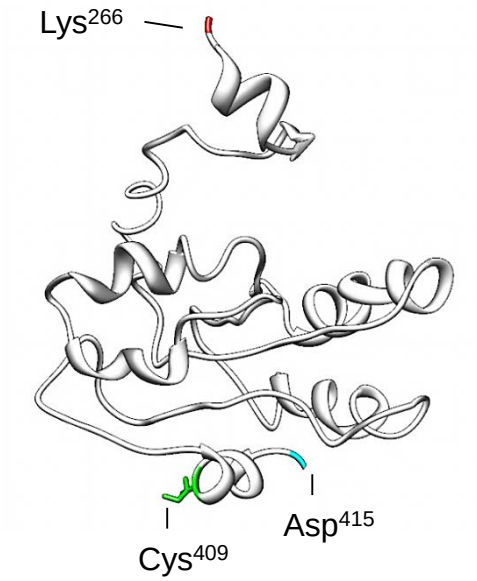

Fig. 38. The theoretical occludin$^{266\text{-}415}$ model. This model gives an insight into the general conformation of the occludin fragment located N-terminally to the coiled-coil domain.

human decay accelerating factor (1M11 chain R), the 50S ribosomal protein L5 (1P85 chain D), the 50S ribosomal protein L5 (1W0R chain A), the marine lipid containing bacteriophage PM2 (2W0C chain T) and the 16S ribosomal protein (2VQE chain A). Five possible models were obtained, and they were matched against the protein structures contained in three independent libraries (enzyme classification number, gene ontology vocabulary and ligand binding sites), considering the matched similarities, only one of the models was predicted to have a functional relevance, here-on referred to as the Occludin$^{266\text{-}415}$ model (**Fig. 38**). The estimated accuracy of this model, as determined by its TM-score was 0.33 ± 0.11 (at a resolution of 12.9 ± 4.2 Å). The TM score measures the structural similarity between two structures (Zhang and Skolnick 2004). A TM-score lower than 0.17 indicates only random similarities, while a score equal or higher than 0.5 is indicative of a correct topology; thus the occludin$^{266\text{-}415}$ model was considered to have an intermediate range of accuracy. On the other hand, the resolution of the model provided information about the general conformation of the molecule, but could not predict the position of individual rotamers, or the spatial position of individual atoms in the molecule.

The match between the occludin$^{266\text{-}415}$ model against the indexed structures in the enzyme classification number database, showed that the following proteins had structural resemblance to it: 1) N-terminal fragment of the phenylalanyl-tRNA synthetase ß-subunit from *Pyrococcus horikoshii* (2CXI.PDB), 2) Urocanase from *Bacillus subtilis* (2FKN.PDB), 3) B-ketoacyl-ACP synthase II (FabF) from *Staphylococcus aureus* (2GQD.PDB), and 4) RNA-dependent RNA polymerase construct 2 from bovine viral diarrhea virus (1S4F.PDB). The similarities between these structures and the occludin$^{266\text{-}415}$ model, expressed as their identity percentage, was for all cases 12% or lower with TM scores ranging from 0.3821 –intermediate accuracy- to 0.4995 –correct topology-. The coverage percentage

(how much of the total length of the enzymes was comparable with the occludin$^{266-415}$ model) ranged between 67% to 80%. The respective TM-scores, identity and coverage of these enzymes, compared to the occludin$^{266-415}$ model, are shown in **table 4**

Table 4. Top enzymes showing similarities to the occludin$^{266-415}$ model.

Rank	TM-score	Identity	Coverage	PDB name (chain)	EC number
1	0.4590	9%	71%	2CXI(A)	6.1.1.20
2	0.4995	7%	80%	2FKN(B)	4.2.1.49
3	0.4987	7%	80%	2FKN(A)	4.2.1.49
4	0.3821	12%	67%	2GQD(A)	2.3.1.179
5	0.4754	8%	73%	1S4F(A)	2.7.7.48

The match against the gene ontology vocabulary database showed similarities between the occludin$^{266-415}$ model and the following proteins: Ribosomal Protein L10-L12 complex (1ZAX.PDB), Tryptophan hydroxylase (1MLW.PDB), Suppressor of tubulin 2 (2QK1.PDB), Thiamine monophosphate kinase of *Thermus thermophilus* (2YXZ.PDB), 30S ribosomal protein from *Thermotoga maritime* (1VMB.PDB), Methanol dehydrogenase from *Hypomicrobium denitrificans* (2D0V.PDB), Rat xanthine oxidoreductase mutant -W^{335}A, F^{336}L- (2E3T.PDB), Cholesterol oxidase from *Bacillus sterolicum* (1i19.PDB), Urocanase from *Bacillus subtilis* (2FKN.PDB), and the iron hydrogenase 1 (3C8Y.PDB). Their respective TM-scores, identity and coverage, compared to occludin$^{266-415}$ model are shown in **table 5**.

Table 5. Top enzymes showing similarities to the structure of model 1.

Rank	TMscore	Identity	Coverage	PDB name (chain)
1	0.7344	7%	86%	1zax(A)
2	0.3524	13%	59%	1mlw(A)
3	0.3686	12%	61%	2qk1(A)
4	0.4096	11%	63%	2yxz(D)
5	0.3699	14%	52%	1vmb(A)
6	0.3765	10%	71%	2d0v(I)
7	0.4375	9%	70%	2e3t(B)
8	0.4666	8%	77%	1i19(B)
9	0.4999	7%	83%	2fkn(D)
10	0.4275	9%	77%	3c8y(A)

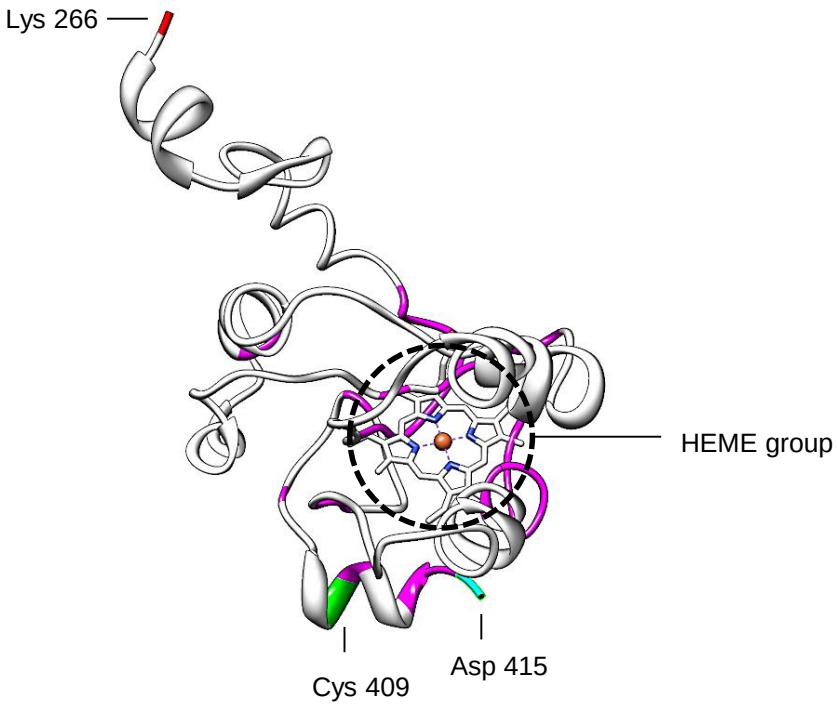

Fig. 39. Theoretical binding pocket of the occludin$^{266\text{-}415}$ model. By comparison with the analogue amino acids in enzymes showing structural similarities with the model, an HEME group might fit into the binding pocket of the model (dashed circle). The positions of the cysteine^{409}, Aspartate^{415} (the C-terminus of the model) and the Lysine^{266}(the N-terminus) are shown.

The relevant gene ontology terms associated with those enzymes were 5488, 3824, 16491, 43169, 43167, 46872, 5198, 5506, 46914 and 9055. They define the catalysis of redox reactions and molecular entities that serve as electron donors or acceptors.

The third functional match of the occludin$^{266\text{-}415}$ model, against known enzymatic binding sites, identified the following analog enzymes: 1) Horseradish peroxidase C1A compound I (1HCH.PDB), 2) Manganese peroxidase (1YYD.PDB), 3) Soybean peroxidase (1FHF.PDB), and 4) Fungal peroxidase from *Arthromyces ramosus* (1ARP.PDB). The following amino acids in the occludin$^{266\text{-}415}$ model formed a binding pocket analogue to the binding sites of those enzymes: ^{293}NVEEWVKNV^{301}, ^{327}SN^{328}, Y^{342}, D^{361}, ^{363}FRQPRYSSGG^{372}, ^{391}KRT^{393}, Y^{398}, Y^{402}, D410 and ^{413}EE^{414}. By comparing this pocket with the binding pockets of the analogue enzymes, it was found that the occludin$^{266\text{-}415}$ model might bind a prosthetic heme group (**Fig. 39**).

3.10.1 Cell extracts containing YFP-Occludin^{WT} have an increased NADH to NAD$^+$ conversion rate.

The similarities between the predicted model of the membrane-proximal C-terminal domain of occludin with a number of oxidoreductases prompted the likelihood that occludin could also show an oxidoreductase activity. Since the most similar oxidoreductase, the urocanase from *B. subtilis*, uses

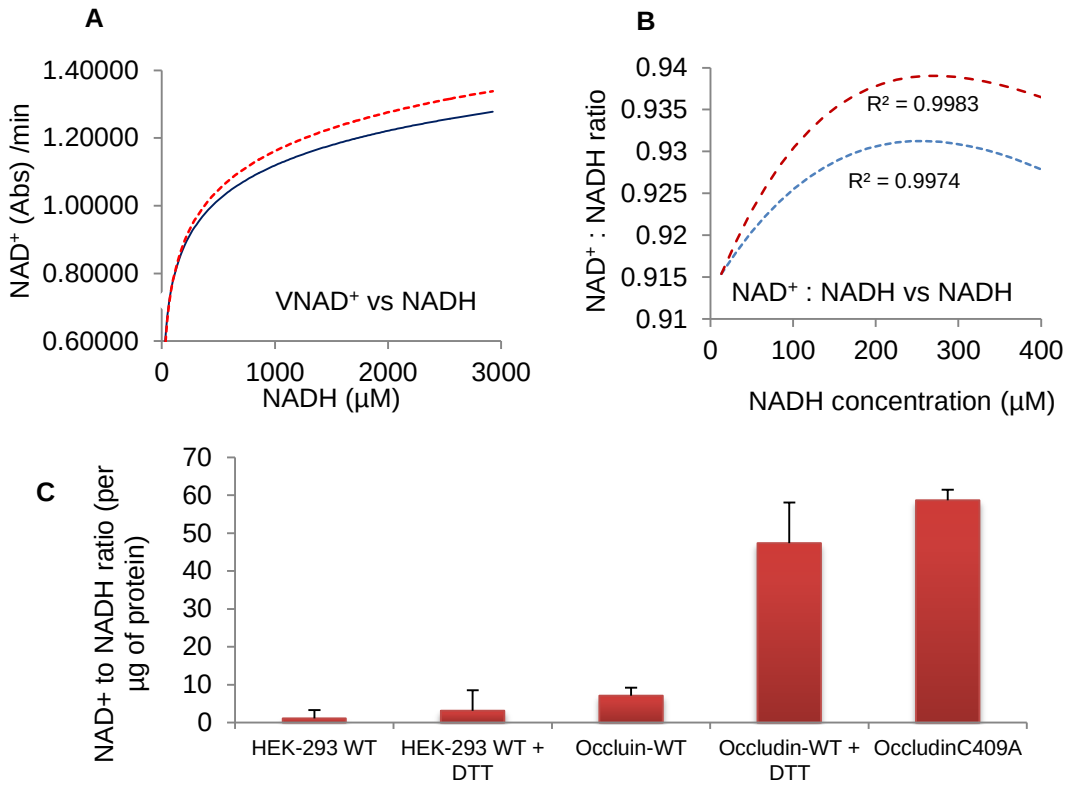

Fig. 40. The Triton X-100 soluble fraction of YFP-Occludin^{WT} expressing cells shows a higher NADH to NAD$^+$ conversion rate than untransfected cells.

A) Generation of NAD$^+$ vs the initial concentration of NADH. The graph shows a logarithmic regression of the conversion velocities of YFP-Occludin^{WT} expressing cells (red) and non-transfected cells (blue).

B) Eadie-Hofstee diagram. The graph shows a polynomial regression of the product (NAD$^+$) to substrate (NADH) ratio vs. the initial concentration of NADH. Although the peak velocities were different, both group of cells (expressing YFP-OccludinWT and non-transfected) achieved their maximum conversion rate when the initial substrate concentration (NADH) was approximately 250 µM.

C) NADH to NAD+ conversion ratio normalized to the sample protein concentration. The graph shows the ratio of NAD$^+$ to NADH relative to the amount of protein concentration in the samples. The initial NADH concentration was 250 µM and when used DTT was added at a concentration of 100 mM. Error bars represent SEM. n = 3 $p < 0.001$ for occludin^{C409A} vs occludin^{WT}, and HEK cells (with or without DTT). No significant difference was found between the occludin^{WT}+DTT samples and occludin^{C409A}.

NAD^+ as a cofactor, the ability of occludin to convert NAD^+ into NADH, or NADH into NAD^+ was explored. Triton X-100 extracts of HEK-293 cells expressing YFP-$Occludin^{WT}$ were incubated with NADH or NAD^+, and the respective production of NAD or NADH was measured by VIS-UV spectrophotometry. The incubation of the cell extracts with NAD+ did not produce noticeable changes in the concentration of NADH in the solution; however, the addition of NADH was promptly followed by an increase in the amount of NAD^+ in solution. The NADH to NAD^+ conversion rate of these extracts was compared to that of untransfected HEK-293 cells.

At low concentrations of NADH, between 10 and 100 µM, the conversion rate of the cells expressing YFP-$Occludin^{WT}$ was 99.8% of the rate of untransfected cells; however, at higher NADH concentrations, between 350 µM and 3 mM, the rate increased steadily up to 105.5% of the untransfected cells (**Fig. 40 A**). The peak velocity was achieved when the NADH concentration approximated 250 µM (**Fig. 40-B**).

Interestingly, for an initial NADH concentration of 250µM the average NADH to NAD^+ conversion ratio of the Triton X-100 extracts of cells expressing YFP-Occludin was significantly increased from 7.06 ± 2.16 per µg of protein to 47.3 ± 10.71 per µg of protein when DTT (100 mM) was added to the extracts. Furthermore, the NAD^+ to NADH ratio of cells expressing YFP-$Occludin^{C409A}$ was 58.64 ± 2.77 per µg of total protein, in absence of DTT. In comparison, the Triton X-100 extracts of untransfected HEK-293 cells showed a NAD^+ to NADH conversion rate of 1.09 ± 2.18 that increased to 3.15 ± 5.38 after the addition of 100 mM DTT (**Fig. 40-C**). These values were consistent across three different experiments.

3.11 Occludin interacts with claudin-5 in hypoxic and normoxic conditions

The interaction of occludin with a second tight junction molecule was also investigated under normoxic and hypoxic conditions. Claudin-5 has a key role in maintaining the barrier function of the TJ in the brain capillary endothelium, thus, the effects of hypoxia were investigated in HEK-293 cells expressing claudin 5-CFP alone, or coexpressing YFP-$Occludin^{WT}$ and claudin 5-CFP.

Claudin 5-CFP, when expressed alone, was found in the cell membrane during normoxic conditions; when coexpressed with YFP-$Occludin^{WT}$, claudin 5-CFP colocalized with YFP-$Occludin^{WT}$ at the cell membrane (**Fig. 41 A**). During hypoxic conditions, claudin 5-CFP, was internalized to intracellular compartments; however, a fraction of it was still found in the plasma membrane. When claudin-5 and YFP-$Occludin^{WT}$, were coexpressed during hypoxia, both molecules were internalized; however, a considerable amount of both proteins remained in the cell membrane where they colocalized (**Fig. 41-B**).

FRET analysis showed that YFP-Occludin^{WT} and claudin 5-CFP interacted when both colocalized in the plasma membrane, they showed an interaction efficiency of 5% ± 0.01 in normoxia, but also in hypoxic conditions (**Fig. 41 D**).

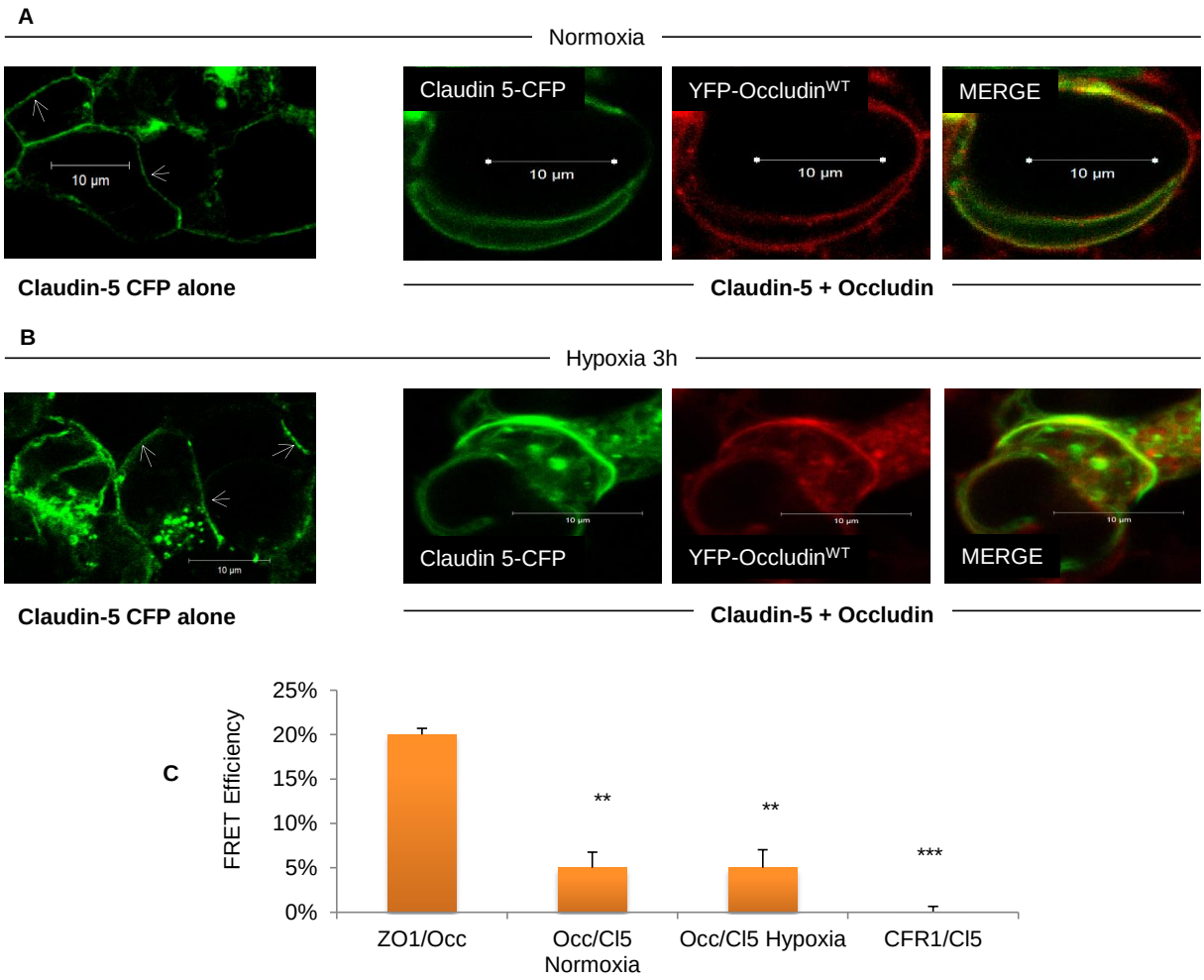

Fig. 41. Occludin interacts with claudin-5 in the cell membrane of HEK-293 cells in normoxic and hypoxic cells.

A).Normoxic HEK-293 cells expressing claudin 5-CFP alone, or coexpressing claudin-5 and occludin. Claudin-5 was localized in the plasma membrane (arrows). When coexpressed with occludin, both molecules colocalized in the cell membrane.

B) Hypoxic HEK-293 cells expressing claudin 5-CFP alone, or coexpressing claudin-5 and occludin. Claudin-5 was internalized after 3 h of hypoxia, but a fraction of it remained in the plasma membrane (arrows). When coexpressed with occludin, both molecules were internalized; however, considerable amounts of both molecules were also found in the plasma membrane where they colocalized.

C) FRET efficiency for the interaction of occludin with claudin-5. The columns show the average FRET efficiencies plus SEM. ZO1: ZO1-CFP, Occ: YFP-OccludinWT, Cl-5:Claudin 5-CFP. CFR-1:corticotropin releasing factor receptor-1 YFP. The efficiency for the ZO1 – occludin interaction is shown as positive control, while the interaction between CFR-1 and claudin-5 is a negative control. The occludin – claudin-5 interaction measurements were repeated in 40 different fields from 10 experimental repetitions, and in all cases, similar FRET efficiencies were found between the hypoxic and normoxic group of cells. n=10, ** $p<0.01$, *** $p< 0.001$

4 DISCUSSION

The TJ are determinants of cell polarity and transepithelial transport; thus, are one of the key elements of the BBB. Several proteins constitute the TJ, and the function of many of them is still not well defined, such is the case for occludin, the first transmembranal protein described; it has been suggested it regulates the TJ, but the mechanisms through which this regulation occurs are still obscure. Inflammation and peripheral pain decrease the expression of occludin, while hypoxia/reoxygenation induces retrieval of occludin from the plasma membrane in brain capillaries (McCaffrey et al., 2008 and 2009).

In that context, the behavior of occludin in response to changes in the intracellular redox potential was studied.

4.1 EXPERIMENTAL APPROACH

The behavior of occludin and ZO-1 were studied in absence of additional tight junction molecules, the TJ-free human embryonic kindey (HEK-293) cells were used as an expression system. These cells do not express claudins, but very low amounts of occludin and ZO-1 (Piontek et al., 2008; Traweger et al., 2002). Three hours of hypoxia were sufficient to induce physiological changes in these cells without compromising their viability.

Different techniques are used to study TJ proteins and their behavior. They are performed either in living cells (e.g. FRET, FRAP, FLIM, FLIP), fixed cells (based on immunodetection), cell extracts (usually involving immunodetection), or in purified proteins (e.g. mass spectrometry, gel chromatography). All have advantages, and in most cases, are complimentary. Studies in purified occludin and ZO-1 can demonstrate the existence of different oligomeric species, however these techniques usually require large amounts of highly purified proteins, and in the case of low abundant proteins an enrichment has to be performed (Lohrberg et al., 2009). Occludin and ZO-1 can be analyzed more easily in cell extracts of HEK-293 that express them; electrophoresis and immunodetection (e.g. Western-blot) can demonstrate and quantify the existence of different oligomeric species of these proteins if they are not denatured either by heat or reducing agents like DTT or ß-mercaptoethanol. However, Western-blots are subject to high variation between experiments and rely heavily on the quality and detection range of the antibodies used; furthermore, the ability of the antibodies to detect a protein may be hindered if their target epitope is blocked (such as during oligomerization), or the target protein has had its conformation changed as a result of manipulation, protein aggregation or changes in the physicochemical properties of the buffer where they are studied. In this work, monoclonal mouse antibodies, directed against the C-terminus of occludin, were originally used. Although they excelled in detecting monomeric occludin and showed different putatively phosphorylated species, they consistently failed to show dimeric or oligomeric forms of occludin (**Fig. 16**). That behavior could be explained if their target epitope, in the C-terminus of occludin, is blocked during the dimerization/oligomerization of the molecule.

Occludin and ZO-1 can also be studied, directly in their cellular environment, either in fixed or living cells. When fixed, HEK-293 cells can be immunostained and analyzed by fluorescence microscopy, or they can be further prepared for electron microscopy analysis. In our particular case, freeze-fracture electron microscopy was used to identify the polymerization of occludin, in the form of strands, in the cell membrane. In order to monitor physiological/pathological changes in the behavior of occludin and ZO-1, in living cells and real-time, fluorescently labeled (CFP or YFP) occludin and ZO-1 were used and analyzed by laser scanning confocal microscopy (LSM).

LSM is a standard technique to study TJ proteins; it can show structural detail up to 200 nm (the theoretical resolution limit of an optical system). Protein-protein interactions can be measured in LSM by means of fluorescence resonance energy transfer (FRET) (Piontek et al., 2008; Blasig et al., 2006). Widely available methods have been developed to measure FRET; as standard, it requires the specific excitation of the donor (CFP) with detection of the acceptor (YFP) fluorescence. Although simple to use, this standard FRET approach is prone to error due to the large spectral bleeding of the donor fluorescent emission into the acceptor detection channel. Several techniques, developed to counter this problem, require the recording of several additional control images of cells, separately expressing the donor and the acceptor, with different excitation and emission filter combinations (Gordon et al., 1998, Xia and Liu 2001, Chen et al., 2005), a computer algorithm is used to determine the different levels of spectral bleeding, and the information is used to remove the “contaminating” background from the final FRET images (Chen et al., 2007), a process called correction. Usually, the process of recording all the control images, required for a given FRET experiment, takes longer than the FRET measurement itself. The speed and accuracy of the process can be improved if spectral approaches are used (Clegg 1992, Zimmermann et al., 2002). In spectral FRET, the images are recorded at a series of discrete wavelength bands, generating what lambda (λ) stacks. The individual spectral signatures of the studied fluorophores, as well as the background noise, are obtained from the λ-stacks by comparing the recorded spectrum with pre-recorded spectra of each of the fluorophores (linear unmixing). Thus, linear unmixing is used to separate the different contributions of individual signals on each of the pixels of the acquired FRET image (Chen et al., 2007, Dickinson et al., 2003). Spectral FRET provides the best way to identify the different fluorescent signals in a sample.

Spectral measurements can also be used for in-vitro FRET analysis using spectrofluorometric approaches (Olwin et al., 1982, Chapman et al., 1992). Here, the amount of bleeding from the acceptor into the donor spectra is used as a direct indication of FRET, and, although extremely reliable, it requires the proteins to be extracted from the cell, thus the results obtained with this technique can be questionable and, since they are performed out of the cell, cannot provide spatial information (Xia and Liu 2001). FRET can also be measured by flow-cytometry (Trón et al., 1984) or by TIRF microscopy in single molecule approaches (Roy et al., 2008).

FRET by acceptor photobleaching is one of the most popular techniques to study protein-protein interactions in living cells; is very specific and lacks many of the disadvantages that other techniques have; however, it has a strong drawback, while bleaching the acceptor fluorophore, the donor is quenched up to some extent, leading to an underestimation of the FRET signal (Chen et al., 2007). On the other hand, overestimation can occur if extensive bleaching of YFP is used, due to YFP to CFP photoconversion (Valentin et al., 2005). Alternatively, FLIM can be performed; the fluorescence lifetime of a fluorophore is sensitive to the presence of other molecules that could influence its excited state (Centonze et al., 2003, Chen et al., 2003); however, the interpretation of FLIM data is often complicated since most of the known fluorophores exhibit multi-exponential fluorescent decays (Suhling et al., 2002); in particular, CFP exhibits different fluorescent states that limit its utility as a donor in FLIM FRET experiments (Tramier et al., 2004).

In FRET by acceptor photobleaching (apFRET), the CFP and YFP signals are measured before, during, and after the bleaching process. If FRET occurs, the intensity of CFP increases while the YFP intensity decreases; on the downside, the continuous scanning during apFRET is lengthy, giving enough time for the structure being recorded to move before the recordings are finished, and leading to false FRET appreciations; in spite of that, apFRET has been used successfully to detect the self-association potential of murine occludin (Blasig et al., 2006).

4.1.1 QUANTUM CORRECTED LAMBDA SCANNING FLUORESCENCE RESONANCE ENERGY TRANSFER

In this work, the expression levels of YFP/CFP tagged occludin and ZO-1 were generally low, and, in particular, the CFP constructs gave particularly low intensity yields that were prone to quenching during the FRET analysis. This posed not only a problem to detect occludin and ZO-1, but also rendered the apFRET approach unviable for the study of the homo and hetero-oligomerization of occludin and ZO-1. To counter this problem, a modified FRET approach, quantum corrected-lambda scanning FRET (qλ-FRET) was devised: using this approach, the samples were scanned once at the beginning of the procedure, bleached a single time and rescanned once at the end. Spectral readings were acquired in the CFP channel only, and based on the amount of YFP signal that bled to the CFP detection channel, the YFP spectrum was reconstructed. Besides increasing the scanning speed, qλ-FRET reduced drastically the CFP quenching during YFP bleaching, and allowed whole microscopic fields to be recorded at once.

The qλ-FRET efficiencies for the pairs claudin-5 YFP/claudin-5 CFP, occludin-YFP/Claudin-5 CFP and ZO-1 CFP/Claudin-5 YFP correlated linearly with those measured by apFRET. However, the qλ-FRET signal was consistently higher than that of apFRET, presumably, due to the inherent FRET signal underestimation that occurs after full YFP photobleaching. On the other hand, the mathematical algorithm used to correct the qλ-FRET measurements also considered the gamma correction factor used by others in the calculations of single molecule FRET (Roy et al., 2008, Ha et al., 1999).

Calculation of the FRET efficiencies for the molecules studied here, using either the formulas for single molecule FRET or qλ-FRET, led to similar results. Thus the qλ-FRET analysis was considered accurate and representative.

To ensure reproducible digitalization of the microscopical fields, the Nyquist criterion was considered for acquisition, thus, an accurate digital representation of the microscopic field was obtained in every recording. The pixel sizes of the acquired images were small enough to permit at least one pixel to be located between two separated visible structures; a pixel size that is 2.3 times smaller than the resolution limit of the optical system (theoretically 200 nm) is required to resolve such separation (Matsumoto 2002). If the pixel size is set to 0.2 µm, it would be impossible to digitally resolve two objects separated by exactly that distance. Thus, to digitally resolve two objects that were separated by the resolution limit of 200 nm, a pixel size of 0.09 µm had to be used if the Nyquist criterion was to be satisfied. Precautions were taken to satisfy that limit, especially in functional microscopy experiments (FRET).

4.1.2 FLUORESCENT POLYACRYLAMIDE GEL ELECTROPHORESIS (F-PAGE)

FRET experiments alone, could not determine the stoichiometry of the observed occludin self-interaction, thus a complementary technique, based on polyacrylamide-gel electrophoresis was developed to detect the different oligomeric forms of occludin.

In conventional Western-blots; oligomeric occludin proved to be difficult to detect. Taking advantage of the already tagged (YFP) occludin, a fluorescent polyacrylamide gel electrophoresis (F-PAGE) assay was implemented. A fluorescence gel retardation assay (Carey 1991) was modified to allow the direct detection of fluorescently labeled TJ proteins in cell extracts separated by electrophoresis. Originally, the gel retardation assay required purified fluorescently labeled proteins to be incubated in a native interaction buffer, and subsequently run in a native polyacrylamide gel. In this work, however, the goal was to identify the already formed oligomeric species of occludin, directly from the HEK cells where they were expressed. Thus, the procedure was modified so the proteins were extracted from the cells using a buffered detergent (Triton X-100), and loaded directly in the gel without intermediate incubation steps. The technique was successfully used to detect the different oligomeric species not only of occludin, but also of other fluorescently labeled membrane proteins, like claudin-5, claudin-12, and the ß subunit of the Na^+ / K^+-ATPase (**Fig. 42**).

F-PAGE provided an easy, accurate and reproducible way to identify the different oligomeric species of occludin without relying on antibodies. This also facilitated the study of different occludin mutants. Since the YFP signal was not quenched by DTT, this agent could still be used to chemically reduce the samples when required.

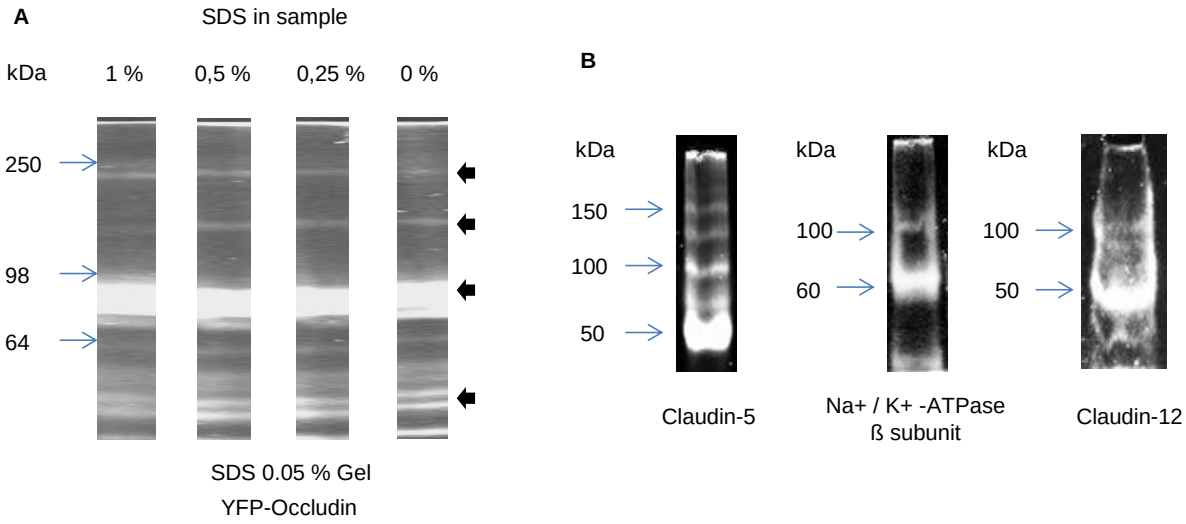

Fig. 42. Reproducibility of F-PAGE to detect oligomeric forms of different membrane proteins. A) Electrophoretic behavior of YFP-Occludin under different SDS concentrations. Dimers can be observed in samples treated under different concentrations of SDS. **B)** The different oligomeric species of fluorescently tagged claudin-5, the β subunit of the sodium pump and claudin 12 are shown by F-PAGE, showing the extensibility of the technique.

The F-PAGE introduced different advantages over a traditional Western blot; the observed signals corresponded only to the tagged protein, false positives, cross-reactivity or background "staining" were absent; besides, it prevented loss of protein due to incomplete blotting or excessive washing. The procedure was considerably fast, taking 40 to 50 min from the point when the cells were harvested until the final image is produced (while a conventional Western-blot takes at least twice the time). The migration of the proteins and separation of the bands can be monitored while the gel is still running, so the electrophoresis running conditions can be optimized on the fly, according to the running behavior of the proteins in question. Moreover, since no antibodies and no secondary detection kits are used, the procedure itself is cheaper compared to a traditional Western-blot. On the downside, it required fluorescently labeled proteins, so its flexibility was limited to the study of those proteins that were successfully fused with a fluorescent tag. It also required specialized laser-based detection equipment. In the long run, however, the cost/effectiveness ratio tilts the balance against immunodetection, especially if rare and expensive antibodies are needed or if, theoretically, a new molecule for which no antibodies existed is studied.

4.2 Expression of occludin in normoxia and hypoxia

When expressed in normoxic HEK-293 cells, YFP-Occludin was found mainly in the cell membrane and enriched at cell-cell contacts. The degree of enrichment at cell-cell contacts correlates with the capability of a membranal protein to self-interact in *trans*.

In order to properly identify the plasma membrane, trypan blue was used (Blasig et al., 2006). The cell-membrane associated YFP-Occludin signal (membrane pool) was quantified and compared to the

non-trypan-blue-colocalizing occludin signal (the intracellular pool). This provided a way to quantify the amount of occludin bound to the plasma membrane and objectively compare it between the different studied conditions i.e. hypoxia, TNF-α, or IFN-γ stimulation.

The redox status of the cytosol was evaluated by determining the cytosolic amount of NADH. One of the prominent metabolic features during hypoxia and inflammation is an imbalance of the cellular NADH/NAD^+ content. NADH is frequently used as a marker to monitor the redox status in living cells and tissues (Rex et al., 2001, Cordeiro et al., 1995). In order to test whether occludin was sensitive to the changes in the cytosolic content of NADH, besides hypoxia, its behavior was analyzed under the influence of Tumoral necrosis factor alpha (TNF-α) and interferon gamma (IFN-γ).

Only hypoxia and TNF-α significantly increased the cellular content of NADH, after a 3 h stimulation. Both inflammatory cytokines, TNF-α and IFN-γ, are known to generate oxidative stress (Mir et al., 2009, Soory et al., 2006); In this work, IFN-γ did not significantly increased the cytosolic NADH content, this could be explained by the fact that only a low dosage and a relative short incubation time were used in the experiments.

Only under hypoxia, or after TNF-α stimulation, occludin shifted from the membrane to the cytosolic pool, indicating that the increased cytosolic content of NADH, and thus an increase in the reducing potential of the cytosol, correlated with the cellular redistribution of occludin. This correlates with previous findings showing that occludin is lost from the cell membrane during inflammation or hypoxia/reoxygenation (McCaffrey et al., 2008; Mark et al., 2002).

It was previously suggested that the change in occludin behavior during hypoxia and inflammation was a result of changes in its oligomerization status (McCaffrey et al., 2008), and the precise mechanism for this to occur was still obscure. Thus in this work, the oligomerization mechanism of occludin, under redox challenging conditions, was studied.

4.2.1 CHANGES ON OCCLUDIN DIMERIZATION

Former studies, using deletion mutants of chick occludin expressed in Xenopus oocytes, showed that occludin can dimerize, and that the C-terminus of the molecule is necessary for the dimerization to take place (Chen et al., 1997). Subsequent studies showed that the dimerization of the purified, recombinant C-terminus of occludin is sensitive to reducing agents like DTT or GSH, in a dose-dependent manner, and for the case of GSH, within physiologically occurring concentrations (Walter et al., 2009). In agreement with those observations, in this work it is shown, that occludin dimerizes when expressed in normoxic cells, but its ability to dimerize was lost during hypoxia, or if occludin was extracted and treated with DTT. This indicated that a disulfide bridge was involved in the dimerization of occludin, and that the disulfide bridge was most likely located in its c-terminal domain. From the two cysteines in the occludin c-terminus, only the $cysteine^{409}$ was able to form a disulfide bridge. The cellular expression of occludin, carrying the C409A mutation, resembled the expression of $occludin^{WT}$

when studied under the influence of hypoxia or TNF-α. Substitution of the other cysteine in the membrane-distal C-terminal domain of occludin (Cys^{500}), buried into the coiled-coil domain, neither modified its subcellular localization nor prevented occludin from dimerizing; in contrast, a double mutation (C409+500A) induced its cellular redistribution and prevented the formation of dimers. This demonstrated that the cysteine 409 is involved in occludin dimerization, likely by forming a disulfide bridge, and that occludin needs to dimerize in order to be stably expressed in the cell surface.

4.2.2 BIOLOGICAL RELEVANCE OF THE OCCLUDIN CYTOSOLIC DISULFIDE BOND

A disulfide bridge is a covalent bond, derived from the coupling of two thiol groups that, at the protein level, are provided by the sulfur-containing lateral chain of the cysteines. Disulfide bridges are strong, have a dissociation energy of 62,6 kcal/ mol, are weaker than carbon-carbon or carbon-hydrogen bonds (Darwent 1970), and can be separated by polar agents, particularly by nucleophiles (Cremlyn 1996) such as thiols (e.g. glutathione).

Disulfide bonds play a key role in the proper folding of a protein by lowering its folding entropy; while linking two protein chains (from the same or different molecules), a disulfide bridge increases the effective local concentration of amino acids and lowers the amount of water molecules in between. Since water attacks the amidic hydrogen bonds formed between amino acids (breaking up the secondary structure), the disulfide bridges also contribute to stabilize the structure of the proteins. The presence of a disulfide bridge in occludin contributes to thermodynamically stabilize the dimerization of the coiled-coil domain.

Disulfide bond formation and disulfide rearrangements (reshuffling) are considered reversible processes, and are thermodynamically affected by the redox state of the environment in which they occur (Hwang et al., 1992, Gilbert 1990, Ziegler 1985). Subcellular compartmentalization plays an important role in regulating the reversible thiol/disulfide exchange reactions. Glutathione is the most abundant non-protein thiol in eukaryotic cells; the preferential compartmentalization of its oxidized, disulfide-bonded form (GSSG), in the endoplasmic reticulum (ER) is thought to be responsible for the differences in the redox potential between the ER and the cytosol. The ratio of reduced (GSH) to oxidized glutathione is approximately 100:1 in the cytosol, while it approaches only 3:1 in the ER (Hwang et al., 1992); this particular redox conditions of the ER are optimal for the formation of disulfide bridges during protein folding, catalyzed by protein disulfide isomerases; nevertheless it has been demonstrated that Ero1, a particular type of disulfide isomerase, catalyzes the formation of disulfide bonds independently of the concentration of GSH or GSSG (Tu and Weissman 2004); in any case, during protein folding, the disulfide bridges are formed inside of the ER, but the intermolecular disulfide bridge of occludin is paradoxically formed in the cytosol, under apparent reducing conditions.

It has been suggested that the redox state of the cytosol, in eukaryotic cells, is not constant, and that could change in response to different physiological stimuli. Molecular compartmentalization can provide small micro-environments within the cytosol, where redox state can considerably vary from the

bulk of the cytosol (cytosolic compartmentalization has been shown for other molecules like cAMP and PKA); however, demonstrating such cytosolic redox compartmentalization poses several technological challenges and has not been demonstrated so far (Schouten et al., 2002). It is therefore possible, that a putative TJ-redox compartment is formed beneath the cell membrane, where the TJ are located; here, the redox conditions could be suitable for maintaining occludin as a dimer.

The formation of disulfide bridges in the cytosol has been often associated with inactivated proteins (Anderson et al., 1995, Ziegler 1985); however, there is increasing evidence indicating that the redox-dependent modulation of specific proteins in the cytosol is an important regulatory mechanism in eukaryotic cells (Parks et al., 1997, Hérouart et al., 1993), furthermore, a number of molecules can form disulfide bridges under reducing conditions; in a specific case, a fragment of the plant antibody scFv, was better folded under mild reducing conditions when studied in a cell-free system, and the whole antibody formed a disulfide bridge in the cytosol of living cells (Schouten et al., 2002, Ryabova et al., 1997). In vitro studies have shown that various cytosolic enzymes can be reversibly activated or inactivated by incubation with disulfides or thiols (Abate et al., 1990, Staal et al., 1990) and several families of cytoplasmic proteins, including oxidoreductases, selectively form or break their disulfide bonds in response to cellular redox stress (Cumming et al., 2004). Although the biological significance of reversible thiol-disulfide exchange reactions in the cytosol is still controversial, there are no doubts about the role of redox modulation in regulating the activity of transcription factors in the cell nucleus or key enzymes in chloroplasts (Gilbert 1990). Thus, the disulfide bridge in occludin may not only be a structural determinant of its cellular expression, but also can constitute an additional regulatory point for its behavior, in particular, given the sensitivity of the interaction of occludin with ZO-1 and the effects of changing the cytosolic redox conditions on the subcellular localization of ZO-1, the disulfide bridge mediated dimerization of occludin can represent an additional regulatory step in the TJ behavior, and also on the TJ-signaling cascades, with implications ranging from gene expression (e.g. via ZONAB activation) to TJ reorganization, cell polarity, growth and differentiation.

4.3 THE INTERACTION OF OCCLUDIN WITH ZO-1 IS REDOX-SENSITIVE

Peptide mapping and mutation studies have shown that the interaction of occludin and ZO-1 occurs via the occludin coiled-coil domain and the SH3-Hinge-GuK unit of ZO-1 (Müller et al., 2005). To characterize the role that the cysteine^{409} played in the interaction of ZO-1 and occludin, the structural basis of this interaction was studied.

4.3.1 THE DIMERIC COILED-COIL DOMAIN OF OCCLUDIN

In a pioneering work, the structure of the coiled-coil domain of human occludin (aa 416-522) was resolved by x-ray crystallography (Li et al., 2005). In that work, two fragments of occludin were used, 384-522 (1XAW.PDB) and 413-522 (1WPA.PDB); both structures differed slightly by the spatial orientation of the coiled-coil domain in the crystals. Dynamic light-scattering and gel-filtration chromatography experiments showed that the occludin coiled-coil domain was monomeric.

Those observations were not only diametrally opposite from the former evidence showing that occludin dimerized in living cells (Chen et al., 1997), but also contrasted with recent work in our laboratory showing that a fragment of murine occludin containing the amino acids 406 to 522, dimerizes when studied by size exclusion chromatography (Walter et al., 2009). Interestingly, dimers were found only in those experiments where the studied occludin fragments contained the cysteine ^{409} (or its homologous in non-human occludin).

Theoretically, the coiled-coil domain of occludin could form six possible dimeric assemblies, but only one showed thermodynamic and hydrophobic profiles compatible with a non-artificial assembly (i.e. not a result of crystal packing). Further thermodynamic analysis revealed that the saline bridges and hydrogen bonds formed between two occludin monomers would be energetically insufficient to maintain a dimeric form; however, the disulfide bridge mediated by the cysteine^{409} has the necessary energy to maintain the coiled-coil dimerized.

The discrepancies found by many authors and the original description of the occludin coiled-coil domain as a monomer could be explained by the fact that, in the original experiments, chemically reducing conditions were used to isolate the coiled-coil domain. Furthermore, a second coiled-coil domain crystal, 1WPA.PDB (Li et al., 2005), that lacked a short aminoacid fragment where the cysteine^{409} is located, showed a shifted spatial orientation, compared to that of the cysteine^{409}-containing crystal (1XAW.PDB). Thus the absence of the occludin aminoacid motif, containing the cysteine^{409}, induced a noticeable change in the crystallization behavior of the coiled-coil domain of occludin.

4.3.2 THE OCCLUDIN / ZO-1 INTERACTION MODEL

ZO-1 requires occludin to reach the plasma membrane, where both molecules interacted. Conversely, during hypoxia, occludin and ZO-1 dissociated and were differentially redistributed in the cells, with ZO-1 traveling to the cell nucleus, while occludin was delocalized from the plasma membrane into intracellular compartments. Furthermore, the non-dimerizing occludin mutant (C409A) was unable to bind to ZO-1, and ZO-1 could not reach the plasma membrane when coexpressed with occludin^{C409A} in normoxic cells. This demonstrated that the interaction of occludin with ZO-1 relies on the ability of occludin to dimerize, and that the loss of occludin dimerization, as happens during redox challenging conditions, signifies a loss on its capacity to associate with ZO-1 and as a result, the ability of ZO-1 to reach the plasma membrane is impaired.

A structural model for the occludin / ZO-1 interaction was generated. The coiled-coil domain of occludin showed a unique diagonally symmetrical distribution of electrostatic charges on its surface, its two lateral ends were electronegative with a positive middle body. This electrostatic arrangement was complimentary to an electropositive surface on one of the faces of the SHG unit of ZO-1. The structure of both molecules was also complimentary, and correlated with the known interaction regions of ZO-1 and occludin (Müller et al., 2005; Schmidt 2004).

In the occludin/ZO-1 interaction model, the dimeric coiled-coil domain of occludin bound the SHG units of two ZO-1 molecules; hence, a hetero-tetrameric assembly was formed: a dimeric coiled coil domain stabilized by a disulfide bridge plus two separated ZO-1 molecules, attached to each lateral ends of the coiled-coil domain. The occludin/ZO-1 complex had a large open area in between the molecules, providing enough room where additional molecules, could complexate. Several signaling and regulatory molecules, such as $G\alpha_{i2}$ bind to the hinge region of ZO-1, thus it is likely that any of these could fit here.

Former surface plasmon resonance studies showed that the SHG unit of ZO-1 can also self-interact (Müller et al., 2005). This opened the possibility that ZO-1 would oligomerize via its SHG unit, in addition to the known dimerization mediated by its second PDZ domain. The SHG unit-dependent oligomerization of ZO-1 was not represented in our model; however, the peculiar symmetry of our model left open the flanks of the SHG units, and particularly, a small electronegative area was exposed in one side, while an electropositive region, apparently complimentary was exposed on the other side. Thus, a polymeric chain could be formed (**Fig. 43**) and could have a potential impact on the membranal organization of occludin, representing an additional element on the cellular organization of the tight junction molecules.

The polymerization of tight junction molecules correlates with their ability to form membranal strands and has been widely studied by freeze fracture electron microscopy (Tsukita and Furuse 1999, Murphy et al., 1982). Occludin has been shown to form short rudimentary strands by itself and copolymerize in claudin-1 and -2 based strands (Furuse et al., 1996 and 1998); moreover, the expression of occludin induces an increase in the width of the TJ strands in epithelial cells (Medina et al., 2000).

In this work, it is shown that occludin can indeed form strands, but only if co-expressed with ZO-1 and under normoxic conditions. Furthermore, correlating with its inability to associate with ZO-1, the non-

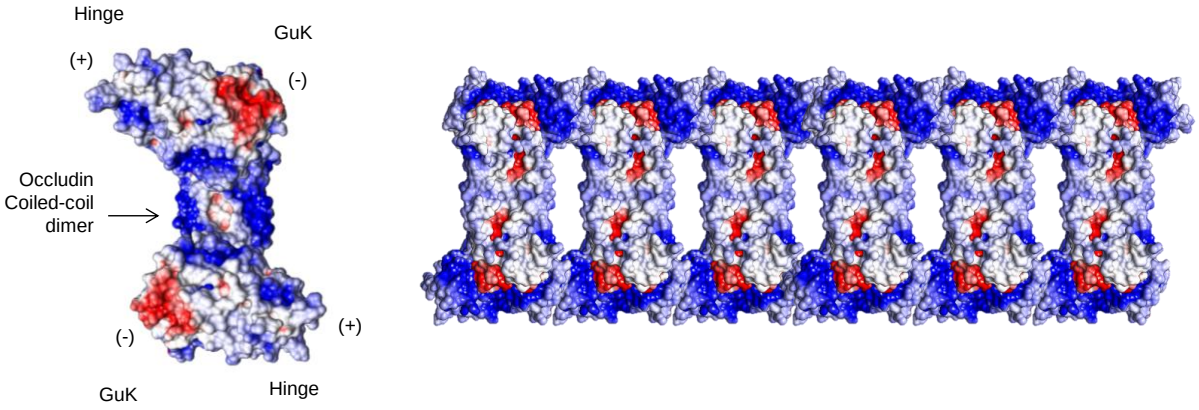

Fig. 43 The dimeric coiled-coil / SHG complex could polymerize. This polymeric model was created only as means to demonstrate 1) that it is possible for the coiled-coil/SHG complex to polymerize and 2) that such polymerization could represent the self-association of the SHG unit of ZO1 observed previously in SPR measurements (Müller 2005).

dimerizing occludin^{C409A} mutant was unable to form strands. Taken together, these observations indicate that a dimerizing-capable occludin is necessary to recruit ZO-1 to the plasma membrane, and that ZO-1 is needed by occludin to be organized in the plasma membrane. It is still not clear, however, whether the occludin based strands are functional in terms of increasing the paracellular tightness or are just a consequence of the ability of ZO-1 to oligomerize.

4.4 Biological implications

4.4.1 The regulatory region of occludin

The amino acid sequence of the membrane-proximal C-terminal domain of occludin is remarkably conserved among different mammalian species. Of particular interest, is the sequence immediately before (N-terminally) to the disulfide forming cysteine^{409} (**Fig. 44**), in this region, the tyrosines^{398} and -^{402}, as well as the threonines^{403} and -^{404}, and the serine^{408}, form a multi-phosphorylation stretch of amino acids immediately proximal to the cysteine^{409} that modulate the expression of occludin and ZO-1 in the cell membranes and the transepithelial permeability (Rao 2009; Feldman et al., 2005; Dörfel et al., 2009; Andreeva et al., 2006, Smales et al., 2003; Cordenonsi et al., 1999).

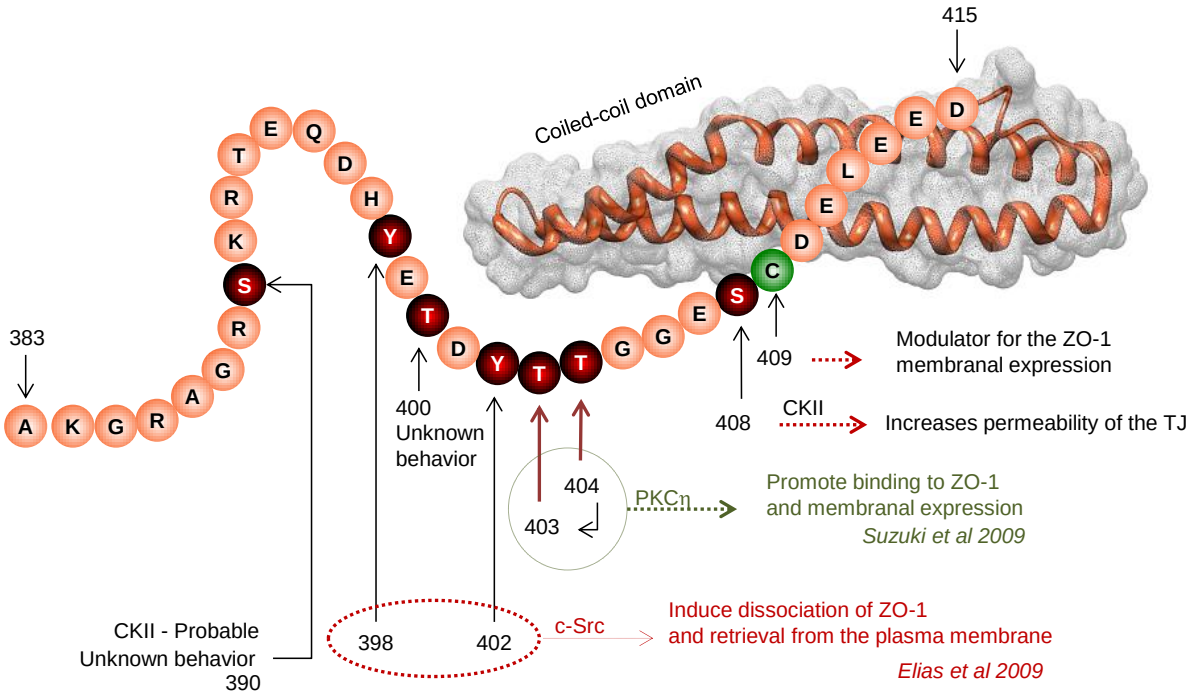


```
Human          384 KGRAGRSKRTEQDHYETDYTTGGESCDELEEDWIR 418
Chimpanzee     330 KGRAGRSKRTEQDHYETDYTTGGESCDELEEDWIR 364
Dog            383 KGRTGRPKRLEQDHYETDYTTGGESCDELEEDWIR 417
Horse          382 KGRAGKSKRPEQDHYETDYTTGGESCDELEEDWVR 416
Mouse          383 KGKAGKGKRTDPDHYETDYTTGGESCEELEEDWVR 417
```

Fig. 44. The regulatory domain of occludin. The region encompassed between the amino acids 384 and 418, immediately before the coiled-coil domain, is conserved among mammals, contains multiple phosphorylation sites, and the cysteine 409.

When the findings related to the cysteine^{409}-mediated dimerization of occludin, described here, are considered together with the physiological effects of the occludin phosphorylation, it becomes clear that the amino acid sequence immediately proximal to the coiled-coil domain plays a unique role in determining the behavior of occludin. By regulating the ability of occludin to be expressed in the plasma membrane as well as its association with ZO-1, chemical changes on this occludin regulatory region can directly influence the structure and function of the TJ. It is likely that the phosphorylation of the occludin regulatory region induces structural and thermodynamical changes on the c-terminus of the molecule, and as a consequence of that, the disulfide bridge mediated by the cysteine^{409}could be formed or dissociated.

4.4.2 OCCLUDIN, THE METABOLIC SENSOR OF THE TJ

Although at this point it is difficult to identify whether phosphorylation has a predominant effect on the behavior of occludin, rather than the redox-sensitive dimerization, experimental evidence suggests that the phosphorylation and the disulfide-bridge mediated oligomerization, work simultaneously. A number of inflammatory cytokines differentially promote the phosphorylation of occludin on serines, threonines or tyrosines, but also induce the cells to undergo redox stress (Blasig et al., 2010, Habib et al., 2010, Escobar et al., 2009, Floyd et al., 1999).

On the other hand, hypoxia itself induces the activation of members of the hypoxia inducible factor (HIF) family. During normoxia, the alpha subunits of these factors are proline-hydroxylated by the constitutively active HIF-prolyl-hydroxylases that use oxygen as cosubstrate; hydroxylated HIF's are recognized for ubiquitination and degradation in proteasome (Semenza 2004, Maxwell et al., 1999). Thus, under low oxygen concentrations, the HIF-prolyl-hydroxylases are inactive and the cellular concentration of HIF's increases. On the other hand, the inhibition of the electron transport chain, during hypoxia or inflammation, results in a buildup of succinate that further contributes to the inhibition of the HIF-prolyl-hydroxylases, increasing the stability of HIF's (Selak et al., 2005). The effects of HIF-1 have been particularly studied, it is considered the main factor controlling the cellular response to hypoxia, and its activation upregulates the expression of several genes to promote cell survivability under low oxygen conditions; these include the vascular endothelial growth factor (VEGF), erythropoietin and the glucose transporter-1 (Görlach and Bonello 2008, Déry et al., 2005). In particular, VEGF is known to delocalize occludin from the TJ, increasing the permeability across monolayers of brain microvascular endothelial cells (Wang et al., 2001); furthermore, VEGF induces phosphorylation of the serine^{490} in occludin, prompting its retrieval from the plasma membrane into early and late endosomes, and consequently, increasing the vascular endothelial permeability (Murakami et al., 2009).

Recently, it has been shown that HIF-1 is also responsive to many stimuli under normoxic conditions, including thrombin, growth factors, vasoactive peptides, insulin, lipopolysaccharide and inflammatory cytokines such as TNF-α, and in many cases, the involvement of oxygen reactive species has been demonstrated (Görlach 2001, Görlach and Bonello 2008, Bonello et al., 2007, Haddad and Land

2001). The mechanism underlying the activity of HIF-1 under such conditions has been associated to the activity of the the redox-sensitive nuclear factor κβ (NF-κβ). NF-κβ binds to a specific site on the HIF-1 gene promoter during normoxic or hypoxic conditions (Görlach and Bonello 2008). NF-κβ is a response element during inflammation and oxidative stress; TNF-α, thrombin, and H_2O_2 induce the phosphorylation of I-κβ, a repressor of the NF-κβ transcription factors, resulting on the upregulation of the NF-κβ transcription. Interestingly, HIF-1 can also upregulate the expression of NF-κβ by hyperphosphorylation of I-κβ (Scortegagna et al., 2008).

Besides stimulating the expression of HIF-1, NF-κβ suppresses the expression of occludin (Chen et al., 2011, Wachtel et al., 2001); it also regulates the expression of the inducible nitric oxide synthase (iNOS) that generates nitric oxide (NO). NO is a key signal molecule in the vascular endothelia, but it also generates peroxynitrite ($ONOO^-$) upon contact with the superoxide radical. Both, peroxynitrite and superoxide, are the main two molecules involved in redox stress in the vascular endothelia (Kohr et al., 2008, Mason et al., 2005), and they are known to induce the cellular redistribution of occludin in endothelial cells (Zhang et al., 2005). Peroxynitrite also induces the nitration of tyrosine residues on PP2A, rendering it immune to inactivation by phosphorylation, and increasing its phosphatase activity (Wu and Wilson 2008).

Altogether, the evidence shows that the signaling pathways of hypoxia, redox-stress, and phosphorylation, are intertwined and promote radical changes on the behavior of the TJ. In this context, the presence of a regulatory region in the C-terminus of occludin, enriched in tyrosines, serines and threonines, and capable of dimerizing the molecule by forming a disulfide bridge, imply that occludin has the potential to respond equally to phosphorylation cascades and to changes in the cellular redox potential. Furthermore, the redox and phosphorylation sensitive interaction of occludin with ZO-1, the main scaffolding protein of the TJ, suggests that occludin plays a pivotal role in the physiology of the TJ by functioning as a metabolic sensor.

4.5 THE NADH OXIDASE ACTIVITY OF OCCLUDIN

Given the strong interplay between occludin and ZO-1, and the regulatory function of the occludin C-terminal domain, the structure of the whole membrane-proximal C-terminal domain of occludin was modeled in-silico, to gain a further understanding on the sterical determinants of such interaction. The model included the fragment spanning from the lysine^{266}, the first intracellular amino acid after the 4th transmembranal domain, until the last amino acid of the regulatory region, the aspartate^{415}.

Unfortunately, the resulting theoretical structure did not provide additional information that could be used to refine the proposed occludin/ZO-1 interaction model. However, it unexpectedly showed several structural similarities with various oxidoreductases. The urocanase from *Bacillus subtilis* was the most similar enzyme; this enzyme is involved in the degradation of histidine, is known to tightly bind NAD^+ as an electrophilic cofactor, and has a conserved cysteine, required for its enzymatic

activity and presumably needed for binding NAD^+ (Rétey 1994). On the other hand, the manganese peroxidase and a fungal peroxidase (ligninase), showed similarities with the occludin$^{266-415}$ model. Both enzymes catalyze peroxide-dependent oxidative reactions, and they are known to bind N-Acetyl-D-Glucosamine -NAG- (Sundaramoorthy et al., 2005, Kunishima et al., 1994). NAG is a monosaccharide derivative from glucose that, in its polymeric form (chitosan), promotes the delocalization of occludin and ZO-1 from the plasma membrane, decreasing the paracellular tightness in mammalian epithelia (Smith et al., 2004, Dodane et al., 1999). That evidence prompted the likelihood of occludin functioning as an oxidase and this novel possibility was explored in preliminary experiments.

The NADH to NAD^+ conversion capacity of the Triton X-100 soluble fraction of HEK-293 cells expressing occludin, the same fraction where the occludin dimers were studied, was higher than the same fraction from non-transfected cells. The reaction peak occurred when the initial NADH concentration approximated 250 µM. Interestingly, when the monomerization of occludin was induced by chemical reduction, a strong increase in the NADH to NAD^+ conversion was observed; this results paired the NADH to NAD^+ conversion rate observed for the non-dimerizing occludin^{C409A} mutant. This striking behavior can represent a possible redox-protective effect of occludin on the tight junction compartment, thus when the cytosolic reducing conditions are increased, the dissociation of occludin dimers into monomers could trigger the occludin enzymatic activity as a possible defense mechanism. This might also give a biological significance to the membranal retention of occludin by claudin-5 under hypoxia. Claudin-5 was still found in the cell membrane during hypoxia, and its interaction with occludin could provide a mechanism to retain occludin and its NADH oxidase activity in the membrane.

These results further support the likelihood that occludin could indeed function as an NADH oxidase. Additional pilot experiments showed that the purified C-terminal domain of occludin has the same enzymatic behavior as the cellular extracts shown here.

Although the precise biological significance of the putative NADH oxidase activity of occludin still needs to be demonstrated, several indications might point to a robust role in regulating not only the TJ behavior, but also in modulating cell-death. Cytosolic depletion of NAD^+ is known to cause the translocation of the apoptosis inducing factor (AIF) from the mitochondria to the nucleus (Yu et al., 2002), furthermore, the histone deacetylase sirtuin-2 (Sir2) is a NAD^+ dependent enzyme that is involved in life span extension during mild cellular stress and starvation (Imai et al., 2000). On the other hand, NAD^+ is also an extracellular signaling molecule (Bruzzone et al., 2001, Takasawa et al., 1993) that is converted to cyclic ADP-ribose, which in turn, induces the Ca^{++} release by the endoplasmic reticulum; this mechanism has been linked to the amelioration of the inflammation-induced epithelial barrier dysfunction in enteral epithelial cells, in fact, the addition of NAD^+ to epithelial cells under inflammatory stimuli prevent the delocalization of ZO-1 and occludin from the tight junctions (Han et al., 2003).

4.6 CONCLUSIVE REMARKS

The TJ in the BBB are altered in several neuroinflammatory and ischemic conditions. As a consequence, the vectorial and specific transport capabilities the brain capillary endothelium is significantly altered, prompting severe alterations in the brain homeostasis, a life threatening condition. On the other hand, when the BBB is intact and therapeutic drugs need to be introduced into the brain parenchyma, the capillary endothelium becomes a formidable obstacle to bypass.

Here, evidence was presented to demonstrate that the transmembranal TJ protein occludin forms an intermolecular disulfide bridge to self-dimerize. The cysteine^{409} (in human) was identified as the key amino acid in this process. The behavior of occludin depended on its ability to form such disulfide bridge that turned out to be regulated by the intracellular redox conditions. Occludin was capable of interacting with ZO-1 and recruit it to the plasma membrane; however, a non-dimerizing occludin mutant, C409A, did not interact with ZO-1 and could not be stably expressed in the plasma membrane.

A structural model was proposed to better describe the interaction of occludin and ZO-1, thus the coiled-coil domain of occludin dimerizes and interacts with the SH3-hinge-GuK units of two ZO-1 molecules. Since the dimeric coiled-coil domain of occludin is predicted to be energetically unstable on its own, naturally tending to dissociate, the ZO-1/occludin heterotetramer could only occur if a disulfide bridge, mediated by the cysteine^{409}, is formed between two adjacent occludin molecules. This implies that the dimerization of occludin promotes its association with ZO-1 and helps ZO-1 to reach the cell surface.

The submembranal recruitment of ZO-1 is necessary for the transmembranal proteins of the TJ to be stably expressed in the cell membrane. In this work, it was shown that occludin reaches the plasma membrane by itself, but it forms membranal strands only if coexpressed with ZO-1, evidencing that ZO-1 also plays a role in organizing occludin in the cell membrane.

Under redox challenging conditions, as induced by hypoxia and inflammation, the disulfide bridge that mediates the dimerization of occludin is dissociated, leading to the monomerization of occludin and the separation of occludin and ZO-1. Since all the TJ proteins are interconnected forming a network, weakening their structural backbone would certainly result on instability of the whole network. Thus, the dissociation of occludin and ZO-1 is likely to weaken the structural stability of the TJ.

Under those conditions, the membrane stability of claudins, determinants of the paracellular tightness and permeability, would be altered, jeopardizing the control of the intercellular permeability. Here, it was found that occludin and claudin-5 can interact with each other under redox challenging conditions (hypoxia) with the same strength as they do in normoxia; this indicates that the mechanism of interaction between claudin-5 and occludin differs substantially from that of occludin and ZO-1. Preliminary observations showed that under hypoxia, more occludin remained in the plasma

membrane if coexpressed with claudin-5 than if expressed alone; indicating that claudin-5 could exert a protective effect in hypoxic conditions by preventing the cellular internalization of occludin.

The redox sensitivity of the ZO-1 and occludin interaction raises the possibility that the cells could directly modify the structural strength of the TJ, and the paracellular permeability, by physiologically modifying their intracellular redox balance. This likelihood is supported by the fact that, according to our former studies, the dimerization of the membrane-distal C-terminal domain of occludin is sensitive to changes in the concentration of GSH at physiological ranges (Walter et al., 2009).

The molecular model of the membrane-proximal C-terminal domain of occludin showed several similarities with a number of oxidoreductases, suggesting that occludin could also have an oxidoreductase activity; initial experiments showed that extracts of cells overexpressing occludin were able to convert NADH into NAD^+ at a higher rate than control cells. Furthermore, by structural homology comparison, a prosthetic (heme) binding site in the model was also suggested. Due to its spatial position, this pocket may be inaccessible while occludin is dimeric, and that suggested that the proposed oxidase activity of occludin might appear only if occludin is monomeric; in accordance to that, inducing the monomerization of occludin, by a reducing agent, prompted a strong increase in the ability of the cell extracts to convert generate NAD^+; furthermore, if the non-dimerizing occludin^{C409A} mutant was overexpressed, instead of the wild-type form, the cell extracts showed the same ability to generate NAD^+ as the chemically-reduced extracts. Thus, the function of occludin might not only be restricted to a mere metabolic sensor, but could also play an active role in the NADH/NAD^+ metabolism.

Finally, a regulatory domain can be identified in the C-terminal domain of occludin. This is formed by a stretch of amino acids located before the coiled-coil domain that contains the cysteine^{409} and several phosphorylation sites. The phosphorylation of different pairs of amino acids selectively induces the association of occludin with ZO-1 and their membranal localization, or the dissociation of both molecules and retrieval of occludin from the cell surface. Phosphorylation of these amino acids could induce sterical changes the vicinity of the cysteine^{409}, allowing or preventing it to form a disulfide bridge. Thus, phosphorylation may impose sterical constraints to the dimerization of occludin, and on the other hand, the redox-conditions of the cytosol must be modified to induce a change in the monomeric/dimeric status of occludin.

Altogether, the evidence shown here not only indicates that the association of occludin and ZO-1 is redox sensitive, but also reveals a fine interplay between occludin and ZO-1 where both molecules work in synchrony, first to help the TJ targeting of ZO-1 and then to help occludin to be well organized in the cell membrane. The redox sensitivity of this double play represents by itself a novel TJ regulatory mechanism that could have profound implications in the behavior of the TJ of epithelia and endothelia, during a wide spectrum of clinopathological conditions where the cells suffer a redox challenge.

5 REFERENCES

Abate C, Patel L, Rauscher FJ 3rd, Curran T. **Redox regulation of fos and jun DNA-binding activity in vitro.** Science. 1990; 249:1157-61.

Aijaz S, D'Atri F, Citi S, Balda MS, Matter K. **Binding of GEF-H1 to the tight junctionassociated adaptor cingulin results in inhibition of Rho signaling and G1/S phase transition.** Dev. Cell. 2005; 8:777–86.

Airy GB. **On the Diffraction of an Object-glass with Circular Aperture.** Transactions of the Cambridge Philosophical Society 1835; 5:283-291.

Anderson LE, Li D, Prakash N, Stevens FJ. **Identification of potential redox-sensitive cysteines in cytosolic forms of fructosebisphosphatase and glyceraldehyde-3-phosphate dehydrogenase.** Planta. 1995; 196:118-24.

Ando-Akatsuka Y, Saitou M, Hirase T, Kishi M, Sakakibara A, Itoh M, Yonemura S, Furuse M, Tsukita S. **Interspecies diversity of the occludin sequence: cDNA cloning of human, mouse, dog, and rat-kangaroo homologues.** J Cell Biol. 1996; 133:43-7.

Andreeva AY, Krause E, Müller EC, Blasig IE, Utepbergenov DI. **Protein kinase C regulates the phosphorylation and cellular localization of occludin.** J Biol Chem. 2001; 276:38480-6.

Andreeva AY, Piontek J, Blasig IE, Utepbergenov DI. **Assembly of tight junction is regulated by the antagonism of conventional and novel protein kinase C isoforms.** Int J Biochem Cell Biol. 2006;38: 222-33.

Andrews DL. **A unified theory of radiative and radiationless molecular energy transfer.** Chemical Physics. 1989; 135:195-201.

Arnold K, Bordoli L, Kopp J, Schwede T. **The SWISS-MODEL workspace: a web-based environment for protein structure homology modelling.** Bioinformatics. 2006; 22:195-201.

Baker NA, Sept D, Joseph S, Holst MJ, McCammon JA. **Electrostatics of nanosystems: application to microtubules and the ribosome.** Proc Natl Acad Sci U S A. 2001; 98:10037-41.

Balda MS, Flores-Maldonado C, Cereijido M, Matter K. **Multiple domains of occludin are involved in the regulation of paracellular permeability.** J Cell Biochem. 2000; 78:85-96.

Balda MS, Garrett MD, Matter K. **The ZO-1-associated Y-box factor ZONAB regulates epithelial cell proliferation and cell density.** J. Cell Biol. 2003; 160:423–32.

Balda MS, Matter K. **The tight junction protein ZO-1 and an interacting transcription factor regulate ErbB-2 expression.** EMBO J. 2000; 19:2024–33.

Barrios-Rodiles M, Brown KR, Ozdamar B, Bose R, Liu Z, Donovan RS, Shinjo F, Liu Y, Dembowy J, Taylor IW, Luga V, Przulj N, Robinson M, Suzuki H, Hayashizaki Y, Jurisica I. **High-throughput mapping of a dynamic signaling network in mammalian cells.** Science. 2005; 307:1621-5.

Betanzos A, Huerta M, Lopez-Bayghen E, Azuara E, Amerena J, Gonzalez-Mariscal L. **The tight junction protein ZO-2 associates with Jun, Fos and C/EBP transcription factors in epithelial cells.** Exp. Cell Res. 2004; 292:51–66.

Blasig I, Bellmann C, Del Vecchio G, Zwanziger D, Huber O, Haseloff RF. **Occludin Protein Family - Oxidative Stress and Reducing Conditions.** Antioxid Redox Signal. 2011. [Epub ahead of print].

Blasig IE, Winkler L, Lassowski B, Mueller SL, Zuleger N, Krause E, Krause G, Gast K, Kolbe M, Piontek J. **On the self-association potential of transmembrane tight junction proteins**. Cell Mol. Life Sci. 2006; 63:505-514.

Blom N, Gammeltoft S, Brunak S. **Sequence and structure-based prediction of eukaryotic protein phosphorylation sites.** J Mol Biol. 1999; 294:1351-62.

Bonello S, Zähringer C, BelAiba RS, Djordjevic T, Hess J, Michiels C, Kietzmann T, Görlach A. **Reactive oxygen species activate the HIF-1alpha promoter via a functional NFkappaB site.** Arterioscler Thromb Vasc Biol. 2007; 27:755-61.

Bose S, French S, Evans FJ, Joubert F, Balaban RS. **Metabolic network control of oxidative phosphorylation: multiple roles of inorganic phosphate.** J Biol Chem. 2003; 278:39155-65.

Brooks TA, Hawkins BT, Huber JD, Egleton RD, Davis TP. **Chronic inflammatory pain leads to increased BBB permeability and tight junction protein alterations.** Am J Physiol Heart Circ Physiol. 2005; 289:H738-43.

Bruce JI, Giovannucci DR, Blinder G, Shuttleworth TJ, Yule DI. **Modulation of [Ca2+]i signaling dynamics and metabolism by perinuclear mitochondria in mouse parotid acinar cells.** J Biol Chem. 2004; 279:12909-17.

Bruzzone S, Franco L, Guida L, Zocchi E, Contini P, Bisso A, Usai C, De Flora A. **A self-restricted CD38-connexin 43 cross-talk affects NAD and cyclic ADP-ribose metabolism and regulates intracellular calcium in 3T3 fibroblasts.** J Biol Chem 2001; 276:48300–48308.

Carey J. **Gel retardation.** Methods Enzymol. 1991; 208:103-17.

Centonze VE, Sun M, Masuda A, Gerritsen H, Herman B. **Fluorescence resonance energy transfer imaging microscopy.** Methods Enzymol. 2003; 360:542-60.

Chapman ER, Alexander K, Vorherr T, Carafoli E, Storm DR. **Fluorescence energy transfer analysis of calmodulin-peptide complexes.** Biochemistry. 1992; 31:12819-25.

Chen F, Hori T, Ohashi N, Baine AM, Eckman CB, Nguyen JH. **Occludin is regulated by epidermal growth factor receptor activation in brain endothelial cells and brains of mice with acute liver failure.** Hepatology 2011; 53:1294-305.

Chen Y, Mauldin JP, Day RN, Periasamy A. **Characterization of spectral FRET imaging microscopy for monitoring nuclear protein interactions.** J Microsc. 2007; 228:139-52.

Chen Y, Merzdorf C, Paul DL, Goodenough DA. **COOH terminus of occludin is required for tight junction barrier function in early Xenopus embryos.** J Cell Biol. 1997; 138:891-9.

Chen Y, Mills JD, Periasamy A. **Protein localization in living cells and tissues using FRET and FLIM.** Differentiation. 2003; 71:528-41.

Chen Y, Periasamy A. **Intensity range based quantitative FRET data analysis to localize protein molecules in live cell nuclei.** J Fluoresc. 2006; 16:95-104.

Choi YJ, Seelbach MJ, Pu H, Eum SY, Chen L, Zhang B, Hennig B, Toborek M. **Polychlorinated biphenyls disrupt intestinal integrity via NADPH oxidase-induced alterations of tight junction protein expression.** Environ Health Perspect. 2010; 118:976-81.

Clegg RM. **Fluorescence resonance energy transfer and nucleic acids.** Methods Enzymol. 1992; 211:353-88.

Cordeiro PG, Kirschner RE, Hu QY, Chiao JJ, Savage H, Alfano RR, Hoffman LA, Hidalgo DA. **Ultraviolet excitation fluorescence spectroscopy: a noninvasive method for the measurement of redox changes in ischemic myocutaneous flaps.** Plast Reconstr Surg. 1995; 96:673-80.

Cordenonsi M, Turco F, D'atri F, Hammar E, Martinucci G, Meggio F, Citi S. **Xenopus laevis occludin. Identification of in vitro phosphorylation sites by protein kinase CK2 and association with cingulin.** Eur J Biochem. 1999; 264:374-84.

Cremlyn R. J. **An Introduction to Organosulfur Chemistry.** John Wiley & Sons Inc. United Kingdom. 1996.

Cumming RC, Andon NL, Haynes PA, Park M, Fischer WH, Schubert D. **Protein disulfide bond formation in the cytoplasm during oxidative stress.** J Biol Chem. 2004; 279:21749-58.

Darwent BB. **Bond Dissociation Energies in Simple Molecules**, National Standard Reference Data Series 31. National Bureau of Standards. United States Department of Commerce. USA. 1970.

Dawson D. **Comprehensive Physiology. Principles of Membrane Transport**. John Wiley & Sons, Inc. published online. 2010.
http://www.comprehensivephysiology.com/WileyCDA/CompPhysArticle/refId-cp060401.html

Day RN, Periasamy A, Schaufele F. **Fluorescence resonance energy transfer microscopy of localized protein interactions in the living cell nucleus.** Methods. 2001; 25:4-18.

Deanfield J, Donald A, Ferri C, Giannattasio C, Halcox J, Halligan S, Lerman A, Mancia G, Oliver JJ, Pessina AC, Rizzoni D, Rossi GP, Salvetti A, Schiffrin EL, Taddei S, Webb DJ. **Endothelial function and dysfunction. Part I: Methodological issues for assessment in the different vascular beds: a statement by the Working Group on Endothelin and Endothelial Factors of the European Society of Hypertension.** J Hypertens. 2005; 23:7-17.

del Zoppo GJ, Mabuchi T**. Cerebral microvessel responses to focal ischemia.** J Cereb Blood Flow Metab. 2003; 23:879-94.

Déry MA, Michaud MD, Richard DE. **Hypoxia-inducible factor 1: regulation by hypoxic and non-hypoxic activators.** Int J Biochem Cell Biol. 2005; 37:535-40.

Dickinson ME, Simbuerger E, Zimmermann B, Waters CW, Fraser SE. **Multiphoton excitation spectra in biological samples.** J Biomed Opt. 2003; 8:329-38.

Dodane V, Amin Khan M, Merwin JR. **Effect of chitosan on epithelial permeability and structure.** Int J Pharm. 1999; 182:21-32.

Dolinsky TJ, Czodrowski P, Li H, Nielsen JE, Jensen JH, Klebe G, Baker NA. **PDB2PQR: expanding and upgrading automated preparation of biomolecular structures for molecular simulations.** Nucleic Acids Res. 2007; 35 (Web Server issue):W522-5.

Dolinsky TJ, Nielsen JE, McCammon JA, Baker NA. **PDB2PQR: an automated pipeline for the setup of Poisson-Boltzmann electrostatics calculations.** Nucleic Acids Res. 2004; 32 (Web Server issue):W665-7.

Dörfel MJ, Westphal JK, Huber O. **Differential Phosphorylation of Occludin and Tricellulin by CK2 and CK1.** Ann N Y Acad Sci. 2009; 1165:69-73.

Du Bois Reymond EH. **Untersuchungen über Tierische Elektrizität.** Reimer. Berlin, Germany. 1848.

Du Bois-Reymond EH. **Vorlaufiger Abriss einer Untersuchung über den sogenannten Froschstrom und über die elektromotorischen Fische.** Poggendorffs Ann. Phys. Chem. 1843; 58:1–22.

Ehrlich P. **Das Sauerstoff-Bedürfniss des Organismus: eine farbenanalytische Studie.** Berlin: Hirschwald. Germany. 1885.

El-Benna J, Dang PM, Gougerot-Pocidalo MA, Marie JC, Braut-Boucher F. **p47phox, the phagocyte NADPH oxidase/NOX2 organizer: structure, phosphorylation and implication in diseases**. Exp Mol Med, 2009; 41:217–225.

Elchuri S, Oberley TD, Qi W, Eisenstein RS, Jackson Roberts L, Van Remmen H, Epstein CJ, Huang TT. **CuZnSOD deficiency leads to persistent and widespread oxidative damage and hepatocarcinogenesis later in life.** Oncogene 2005; 24:367–80.

Elias BC, Suzuki T, Seth A, Giorgianni F, Kale G, Shen L, Turner JR, Naren A, Desiderio DM, and Rao R. **Phosphorylation of Tyr-398 and Tyr-402 in Occludin Prevents Its Interaction with ZO-1 and Destabilizes Its Assembly at the TJ**. J Biol Chem 2009; 284:1559-1569.

Escobar J, Pereda J, Arduini A, Sandoval J, Sabater L, Aparisi L, López-Rodas G, Sastre J. **Cross-talk between oxidative stress and pro-inflammatory cytokines in acute pancreatitis: a key role for protein phosphatases.** Curr Pharm Des. 2009; 15:3027-42.

Farquhar MG, Palade GE. **Junctional complexes in various epithelia.** J Cell Biol. 1963; 17:375-412.

Feldman GJ, Mullin JM, Ryan MP. **Occludin: structure, function and regulation.** Adv Drug Deliv Rev. 2005; 57:883-917.

Fischer S, Renz D, Kleinstück J, Schaper W, Karliczek GF. **In vitro effects of anaesthetic agents on the BBB.** Anaesthesist. 2004; 53:1177-84.

Floyd RA, Hensley K, Jaffery F, Maidt L, Robinson K, Pye Q, Stewart C. **Increased oxidative stress brought on by pro-inflammatory cytokines in neurodegenerative processes and the protective role of nitrone-based free radical traps.** Life Sci. 1999; 65:1893-9.

Frömter E, Diamond J. **Route of passive ion permeation in epithelia.** Nat New Biol. 1972; 235:9-13.

Furuse M, Fujimoto K, Sato N, Hirase T, Tsukita S, Tsukita S. **Overexpression of occludin, a tight junction-associated integral membrane protein, induces the formation of intracellular multilamellar bodies bearing tight junction-like structures.** J Cell Sci. 1996; 109:429-35.

Furuse M, Fujita K, Hiiragi T, Fujimoto K, Tsukita S. **Claudin-1 and -2: novel integral membrane proteins localizing at TJ with no sequence similarity to occludin.** J Cell Biol. 1998; 141:1539-50.

Furuse M, Furuse K, Sasaki H, Tsukita S. **Conversion of zonulae occludentes from tight to leaky strand type by introducing claudin-2 into Madin-Darby canine kidney I cells.** J. Cell Biol. 2001; 153:263–72.

Furuse M, Hirase T, Itoh M, Nagafuchi A, Yonemura S, Tsukita S, Tsukita S. **Occludin: a novel integral membrane protein localizing at TJ.** J Cell Biol. 1993; 123:1777-88.

Furuse M, Itoh M, Hirase T, Nagafuchi A, Yonemura S, Tsukita S, Tsukita S**. Direct association of occludin with ZO-1 and its possible involvement in the localization of occludin at TJ.** J Cell Biol. 1994; 127:1617-26.

Furuse M, Sasaki H, Fujimoto K, Tsukita S. **A single gene product, claudin-1 or -2, reconstitutes tight junction strands and recruits occludin in fibroblasts.** J Cell Biol. 1998; 143:391-401.

Furuse M, Sasaki H, Tsukita S. **Manner of interaction of heterogeneous claudin species within and between tight junction strands.** J. Cell Biol. 1999; 147:891–903.

Gilbert HF. **Molecular and cellular aspects of thiol-disulfide exchange.** Adv Enzymol Relat Areas Mol Biol. 1990; 63:69-172.

Gonzalez-Mariscal L, Betanzos A, Avila-Flores A. **MAGUK proteins: structure and role in the tight junction**. Semin. Cell Dev. Biol. 2000; 11:315–24.

Gonzalez-Mariscal L, Betanzos A, Nava P, Jaramillo BE. **Tight junction proteins.** Prog. Biophys. Mol. Biol. 2003; 81:1-44.

Gordon GW, Berry G, Liang XH, Levine B, Herman B. **Quantitative fluorescence resonance energy transfer measurements using fluorescence microscopy.** Biophys. J. 1998; 74:2702–2713.

Görlach A, Bonello S. **The cross-talk between NF-kappaB and HIF-1: further evidence for a significant liaison.** Biochem J. 2008; 412:e17-9.

Görlach A, Diebold I, Schini-Kerth VB, Berchner-Pfannschmidt U, Roth U, Brandes RP, Kietzmann T, Busse R. **Thrombin activates the hypoxia-inducible factor-1 signaling pathway in vascular smooth muscle cells: Role of the p22(phox)-containing NADPH oxidase.** Circ Res. 2001; 89:47-54.

Gray, H. **Anatomy of the Human Body**. Philadelphia: Lea & Febiger, USA. 1918.

Ha T, Ting AY, Liang J, Caldwell WB, Deniz AA, Chemla DS, Schultz PG, Weiss S. **Single-molecule fluorescence spectroscopy of enzyme conformational dynamics and cleavage mechanism.** Proc Natl Acad Sci USA. 1999; 96:893-8.

Habib N, Goswami G, Mungre S. **Inflammatory cytokines induce oxidative stress and apoptosis in PC12 cells.** FASEB J. 2010; 24(Meeting Abstract Supplement):485.

Haddad JJ, Land SC. **A non-hypoxic, ROS-sensitive pathway mediates TNF-alpha-dependent regulation of HIF-1alpha.** FEBS Lett. 2001; 505:269-74.

Han X, Uchiyama T, Sappington PL, Yaguchi A, Yang R, Fink MP, Delude RL. **NAD+ ameliorates inflammation-induced epithelial barrier dysfunction in cultured enterocytes and mouse ileal mucosa.** J Pharmacol Exp Ther. 2003; 307:443-9.

Harhaj NS, Felinski EA, Wolpert EB, Sundstrom JM, Gardner TW, Antonetti DA. **VEGF activation of protein kinase C stimulates occludin phosphorylation and contributes to endothelial permeability.** Invest Ophthalmol Vis Sci. 2006; 47:5106-15.

Harrison DG, Gongora MC. **Oxidative stress and hypertension**. Med Clin North Am. 2009; 93:621–635.

Haseloff RF., Piontek J., Blasig IE. **The Investigation of cis-and trans-interactions between claudins**. Current Topics in Membranes. Vol 65, Burlington: Academic Press. USA. 2010.

Heinrich N, Meyer MR, Furkert J, Sasse A, Beyermann M, Bönigk W, Berger H. **Corticotropin-releasing factor (CRF) agonists stimulate testosterone production in mouse leydig cells through CRF receptor-1.** Endocrinology. 1998; 139:651-8.

Hérouart D, Van Montagu M, Inzé D. **Redox-activated expression of the cytosolic copper/zinc superoxide dismutase gene in Nicotiana.** Proc Natl Acad Sci USA. 1993; 90:3108-12.

Huber J.D., Hau V. S., Borg L., Campos C. R., Egleton R. D., and Davis T. P. **BBB TJ are altered during a 72-h exposure to -carrageenan-induced inflammatory pain.** Am J Physiol Heart Circ Physiol. 2002; 283:H1532-H1537.

Hwang C, Sinskey AJ, Lodish HF. **Oxidized redox state of glutathione in the endoplasmic reticulum.** Science. 1992; 257:1496–1502.

Ikeda E, Flamme I, Risau W. **Developing brain cells produce factors capable of inducing the HT7 antigen, a BBB-specific molecule, in chick endothelial cells**. Neurosci Lett. 1996; 209:149-52.

Imai S, Armstrong CM, Kaeberlein M, and Guarente L. **Transcriptional silencing and longevity protein Sir2 is an NAD-dependent histone deacetylase.** Nature 2000; 403, 795–800.

Jain E., Bairoch A., Duvaud S., Phan I., Redaschi N., Suzek B.E., Martin M.J., McGarvey P., and Gasteiger E. **Infrastructure for the life sciences: design and implementation of the UniProt website.** BMC Bioinformatics. 2009; 10:136.

Janzer RC, Raff MC. **Astrocytes induce BBB properties in endothelial cells.** Nature. 1987; 325:253-7.

Jaramillo BE, Ponce A, Moreno J, Betanzos A, Huerta M, Lopez-Bayghen E, Gonzalez-Mariscal L. **Characterization of the tight junction protein ZO-2 localized at the nucleus of epithelial cells.** Exp. Cell Res. 2004. 297:247–58.

Kasimova MR, Grigiene J, Krab K, Hagedorn PH, Flyvbjerg H, Andersen PE, Møller IM. **The free NADH concentration is kept constant in plant mitochondria under different metabolic conditions.** Plant Cell. 2006; 18:688-98.

Kay M, Swift L, Martell B, Arutunyan A, Sarvazyan N. **Locations of ectopic beats coincide with spatial gradients of NADH in a regional model of low-flow reperfusion.** Am J Physiol Heart Circ Physiol. 2008; 294:H2400-5.

Koefoed-Johnsen V and Ussing HH. **The nature of the frog skin potential.** Acta Physiol Scand 1958; 42: 298–308.

Kohr MJ, Wang H, Wheeler DG, Velayutham M, Zweier JL, Ziolo MT. **Targeting of phospholamban by peroxynitrite decreases beta-adrenergic stimulation in cardiomyocytes.** Cardiovasc Res. 2008; 77:353-61.

Krause G, Winkler L, Mueller SL, Haseloff RF, Piontek J, Blasig IE. **Structure and function of claudins.** Biochim Biophys Acta. 2008; 1778:631-45.

Krissinel E, Henrick K. **Inference of macromolecular assemblies from crystalline state.** J Mol Biol. 2007; 372:774-97.

Krizbai IA, Bauer H, Bresgen N, Eckl PM, Farkas A, Szatmari E, Traweger A, Wejksza K, and Bauer HC. **Effect of oxidative stress on the junctional proteins of cultured cerebral endothelial cells.** Cell Mol Neurobiol 2005; 25:129-139.

Kunishima N, Fukuyama K, Matsubara H, Hatanaka H, Shibano Y, Amachi T. **Crystal structure of the fungal peroxidase from Arthromyces ramosus at 1.9 A resolution. Structural comparisons with the lignin and cytochrome c peroxidases.** J Mol Biol. 1994; 235:331-44.

Laemmli UK. **Cleavage of structural proteins during the assembly of the head of bacteriophage T4.** Nature. 1970; 227:680-5.

Li Y, Fanning AS, Anderson JM, Lavie A. **Structure of the conserved cytoplasmic C-terminal domain of occludin: identification of the ZO-1 binding surface.** J Mol Biol. 2005; 352:151-64.

Li Y, Zhang Y. **REMO: A new protocol to refine full atomic protein models from C-alpha traces by optimizing hydrogen-bonding networks.** Proteins. 2009; 76:665-76.

Liu S, Yang W, Shen L, Turner JR, Coyne CB, Wang T. **Tight junction proteins claudin-1 and occludin control hepatitis C virus entry and are downregulated during infection to prevent superinfection.** J Virol. 2009; 83(4):2011-4.

Lodish H, Berk A, Zipursky SL, et al. **Molecular Cell Biology**. W. H. Freeman. USA. 2000.

Lohrberg D, Krause E, Schümann M, Piontek J, Winkler L, Blasig IE, Haseloff RF.
A strategy for enrichment of claudins based on their affinity to Clostridium perfringens enterotoxin. BMC Mol Biol. 2009; 10:61.

Lye M.F, Fanning A.S, Su Y, Anderson J.M., Lavie A. **Insights into regulated ligand binding sites from the structure of ZO-1 Src homology 3-guanylate kinase module.** J Biol Chem. 2010; 285:13907-17.

Mark K.S., Davis T.P. **Cerebral microvascular changes in permeability and TJ induced by hypoxia-reoxygenation.** Am J Physiol Heart Circ Physiol. 2002; 282:H1485-94.

Mason RP, Kalinowski L, Jacob RF, Jacoby AM, Malinski T. **Nebivolol reduces nitroxidative stress and restores nitric oxide bioavailability in endothelium of black Americans.** Circulation. 2005; 112:3795-801.

Matsumoto B. **Cell Biological Applications of confocal microscopy.** Methods in cell biology Vol. 70**.** Elsevier Science: Academic Press. USA 2002.

Maxwell PH, Wiesener MS, Chang GW, Clifford SC, Vaux EC, Cockman ME, Wykoff CC, Pugh CW, Maher ER, Ratcliffe PJ. **The tumour suppressor protein VHL targets hypoxia-inducible factors for oxygen-dependent proteolysis.** Nature. 1999; 399:271-5.

McCaffrey G, Seelbach MJ, Staatz WD, Nametz N, Quigley C, Campos CR, Brooks TA, Davis TP. **Occludin oligomeric assembly at TJ of the BBB is disrupted by peripheral inflammatory hyperalgesia.** J Neurochem. 2008; 106:2395-409.

McCaffrey G, Staatz WD, Quigley CA, Nametz N, Seelbach MJ, Campos CR, Brooks TA, Egleton RD, Davis TP. **TJ contain oligomeric protein assembly critical for maintaining BBB integrity in vivo. J Neurochem.** 2007; 203: 2540-2555.

McCaffrey G, Willis CL, Staatz WD, Nametz N, Quigley CA, Hom S, Lochhead JJ, Davis TP. **Occludin oligomeric assemblies at TJ of the BBB are altered by hypoxia and reoxygenation stress.** J Neurochem. 2009; 110:58-71.

Medina R, Rahner C, Mitic LL, Anderson JM, Van Itallie CM. **Occludin localization at the tight junction requires the second extracellular loop.** J Membr Biol. 2000; 178:235-47.

Mir M., Asensio VJ., Tolosa L., Gou-Fabregas M., Soler RM., Llado J., Olmos G. **Tumor necrosis factor alpha and interferon gamma cooperatively induce oxidative stress and motoneuron death in rat spinal cord embryonic explants.** Neuroscience. 2009 162:959-971.

Müller SL, Portwich M, Schmidt A, Utepbergenov DI, Huber O, Blasig IE, Krause G. **The tight junction protein occludin and the adherens junction protein alpha-catenin share a common interaction mechanism with ZO-1.** J Biol Chem. 2005; 280:3747-56.

Murakami T, Felinski EA, Antonetti DA. **Occludin phosphorylation and ubiquitination regulate tight junction trafficking and vascular endothelial growth factor-induced permeability.** J Biol Chem. 2009; 284:21036-46.

Murphy CR, Swift JG, Need JA, Mukherjee TM, Rogers AW. **A freeze-fracture electron microscopic study of TJ of epithelial cells in the human uterus.** Anat Embryol (Berl). 1982; 163:367-70.

Nusrat A, Chen JA, Foley CS, Liang TW, Tom J, Cromwell M, Quan C, Mrsny RJ.**The coiled-coil domain of occludin can act to organize structural and functional elements of the epithelial tight junction**. J Biol Chem. 2000; 275:29816-22.

Nyquist H. **Certain topics in telegraph transmission theory**. AIEE Trans. 1928; 47:617-644.

Olwin BB, Keller CH, Storm DR. **Interaction of a fluorescent N-dansylaziridine derivative of troponin I with calmodulin in the absence and presence of calcium.** Biochemistry. 1982; 21:5669-75.

Palade GE. **A study of fixation for electron microscopy.** J Exp Med. 1952; 95:285-98.

Parks D, Bolinger R, Mann K. **Redox state regulates binding of p53 to sequence-specific DNA, but not to non-specific or mismatched DNA.** Nucleic Acids Res. 1997; 25:1289-95.

Pettersen EF, Goddard TD, Huang CC, Couch GS, Greenblatt DM, Meng EC, Ferrin TE. **UCSF Chimera--a visualization system for exploratory research and analysis.** J Comput Chem. 2004; 25:1605-12.

Piontek J, Winkler L, Wolburg H, Muller SL, Zuleger N, Piehl C, Wiesner B, Krause G, Blasig IE. **Formation of tight junction: determinants of homophilic interaction between classic claudins**. FASEB J, 2008; 22:146-158.

Ploss A, Evans MJ, Gaysinskaya VA, Panis M, You H, de Jong YP, Rice CM. **Human occludin is a hepatitis C virus entry factor required for infection of mouse cells** Nature 2009; 457:882-886

Rao R. **Occludin phosphorylation in regulation of epithelial TJ.** Ann N Y Acad Sci. 2009; 1165:62-8.

Rao RK, Basuroy S, Rao VU, Karnaky KJ, and Gupta A. **Tyrosine phosphorylation and dissociation of occludin-Z0-1 and E-cadherin-beta-catenin complexes from the cytoskeleton by oxidative stress.** Biochem J 2002; 368: 471-481.

Raymond SB, Skoch J, Hynynen K, Bacskai BJ. **Multiphoton imaging of ultrasound/Optison mediated cerebrovascular effects in vivo.** J Cereb Blood Flow Metab. 2007; 27:393-403.

Rétey J. **The urocanase story: a novel role of NAD+ as electrophile.** Arch Biochem Biophys. 1994; 314:1-16.

Rex A., Pfeifer L., Fink H.. **Determination of NADH in frozen rat brain sections by laser-induced fluorescence.** Biol Chem. 2001; 382:1727-32.

Roy A, Kucukural A, Zhang Y. **I-TASSER: a unified platform for automated protein structure and function prediction.** Nat Protoc. 2010; 5:725-38.

Roy R, Hohng S, Ha T. **A practical guide to single-molecule FRET.** Nat Methods. 2008; 5:507-16.

Ryabova LA, Desplancq D, Spirin AS, Plückthun A. **Functional antibody production using cell-free translation: effects of protein disulfide isomerase and chaperones.** Nat Biotechnol. 1997; 15:79-84.

Schmidt A, Utepbergenov DI, Mueller SL, Beyermann M, Schneider-Mergener J, Krause G, Blasig IE.**Occludin binds to the SH3-hinge-GuK unit of zonula occludens protein 1: potential mechanism of tight junction regulation.** Cell Mol Life Sci. 2004; 61:1354-65.

Schneeberger EE, Lynch RD. **Structure, function, and regulation of cellular TJ.** Am. J. Physiol. 1992; 262:L647–L661.

Schouten A, Roosien J, Bakker J, Schots A. **Formation of disulfide bridges by a single-chain Fv antibody in the reducing ectopic environment of the plant cytosol.** J Biol Chem. 2002; 277:19339-45.

Scortegagna M, Cataisson C, Martin RJ, Hicklin DJ, Schreiber RD, Yuspa SH, Arbeit JM. **HIF-1alpha regulates epithelial inflammation by cell autonomous NFkappaB activation and paracrine stromal remodeling.** Blood. 2008; 111:3343-54.

Selak MA, Armour SM, MacKenzie ED, Boulahbel H, Watson DG, Mansfield KD, Pan Y, Simon MC, Thompson CB, Gottlieb E. **Succinate links TCA cycle dysfunction to oncogenesis by inhibiting HIF-alpha prolyl hydroxylase.** Cancer Cell. 2005; 7:77-85.

Semenza GL. **Hydroxylation of HIF-1: oxygen sensing at the molecular level.** Physiology (Bethesda). 2004; 19:176-82.

Seth A, Sheth P, Elias BC, Rao R. **Protein phosphatases 2A and 1 interact with occludin and negatively regulate the assembly of TJ in the CACO-2 cell monolayer.** J Biol Chem. 2007; 282:11487-98.

Shannon CE. **A Mathematical Theory of Communication**. Bell Syst. Techn. J. 1948; 27:379-423.

Sheth P, Samak G, Shull JA, Seth A, Rao R. **Protein phosphatase 2A plays a role in hydrogen peroxide-induced disruption of TJ in Caco-2 cell monolayers** Biochem J. 2009; 421:59-70.

Shin K, Fogg VC, Margolis B. **TJ and cell polarity.** Annu Rev Cell Dev Biol. 2006; 22:207-35.

Skou, JC. **The influence of some cations on an adenosine triphosphatase from the peripheral nerves.** Biochim. et biophys. acta 1957; 23:394.

Smales C, Ellis M, Baumber R, Hussain N, Desmond H, Staddon JM. **Occludin phosphorylation identification of an occludin kinase in brain and cell extracts as CK2.** FEBS Lett. 2003; 545:161-6.

Smith J, Wood E, Dornish M. **Effect of chitosan on epithelial cell TJ** Pharm Res. 2004; 21:43-9.

Soory M., and Tilakaratne A. **Oxidative stress induced by TNF-alpha and glucose in an osteoblastic model and therapeutic implications of minocycline.** Endocrine Abstracts. 2006; 12: 45.

Spring, K. **Routes and mechanism of fluid transport by epithelia.** Annu. Rev. Physiol. 1998; 60:105–119.

Staal FJ, Roederer M, Herzenberg LA, Herzenberg LA. **Intracellular thiols regulate activation of nuclear factor kappa B and transcription of human immunodeficiency virus.** Proc Natl Acad Sci USA. 1990; 87:9943-7.

Stevenson BR, Goodenough DA. **Zonulae occludentes in junctional complex-enriched fractions from mouse liver: preliminary morphological and biochemical characterization.** J Cell Biol. 1984; 98:1209-1221.

Stevenson BR, Siliciano JD, Mooseker MS, Goodenough DA. **Identification of ZO-1: a high molecular weight polypeptide associated with the tight junction (zonula occludens) in a variety of epithelia.** J Cell Biol. 1986; 103:755-66.

Suhling K, Siegel J, Phillips D, French PM, Lévêque-Fort S, Webb SE, Davis DM. **Imaging the environment of green fluorescent protein.** Biophys J. 2002; 83:3589-95.

Sundaramoorthy M, Youngs HL, Gold MH, Poulos TL. **High-resolution crystal structure of manganese peroxidase: substrate and inhibitor complexes.** Biochemistry. 2005; 44:6463-70.

Sundstrom JM, Tash BR, Murakami T, Flanagan JM, Bewley MC, Stanley BA, Gonsar KB, Antonetti DA. **Identification and analysis of occludin phosphosites: a combined mass spectrometry and bioinformatics approach.** J Proteome Res. 2009; 8:808-17.

Suzuki T, Elias BC, Seth A, Shen L, Turner JR, Giorgianni F, Desiderio D, Guntaka R, and Rao R. **PKC eta regulates occludin phosphorylation and epithelial tight junction integrity.** Proc Natl Acad Sci USA. 2009; 106:61-66.

Takasawa S, Nata K, Yonekura H, Okamoto H. **Cyclic ADP-ribose in insulin secretion from pancreatic beta cells.** Science 1993; 259:370–373.

Testut L. **Traité d'Anatomie humaine**. Doin Ed, Paris, France. 1896.

Tramier M, Kemnitz K, Durieux C, Coppey-Moisan M. **Picosecond time-resolved microspectrofluorometry in live cells exemplified by complex fluorescence dynamics of popular probes ethidium and cyan fluorescent protein.** J Microsc. 2004; 213:110-8.

Traweger A, Fang D, Liu YC, Stelzhammer W, Krizbai IA, Fresser F, Bauer HC, Bauer H.
The tight junction-specific protein occludin is a functional target of the E3 ubiquitin-protein ligase itch. J Biol Chem. 2002; 277:10201-8.

Trón L, Szöllósi J, Damjanovich S, Helliwell SH, Arndt-Jovin DJ, Jovin TM. **Flow cytometric measurement of fluorescence resonance energy transfer on cell surfaces. Quantitative evaluation of the transfer efficiency on a cell-by-cell basis.** Biophys J. 1984; 45:939-46.

Tsukita S, Furuse M, Itoh M. **Multifunctional strands in TJ.** Nat Rev Mol Cell Biol. 2001; 2:285-93.

Tsukita S, Furuse M. **Occludin and claudins in tight-junction strands: leading or supporting players?** Trends Cell Biol. 1999; 9:268-73.
Tu BP, Weissman JS. **Oxidative protein folding in eukaryotes mechanisms and consequences.** J Cell Biol. 2004; 164:341-6.

Ussing HH and Zerahn K. **Active transport of sodium as the source of electric current in the short-circuited isolated frog skin.** Acta Physiol Scand 1951; 23:110-127.

Ussing HH, Windhager EE. **Nature of shunt path and active sodium transport path through frog skin epithelium.** Acta Physiol Scand. 1964; 61:484-504.

Valentin G, Verheggen C, Piolot T, Neel H, Coppey-Moisan M, Bertrand E. **Photoconversion of YFP into a CFP-like species during acceptor photobleaching FRET experiments.** Nat Methods. 2005; 2:801.

Van Itallie CM, Anderson JM. **Occludin confers adhesiveness when expressed in fibroblasts.** J. Cell Sci. 1997; 110:1113-21.

Walter JK., Castro V., Voss M., Gast K., Rueckert C., Piontek J., and Blasig IE. **Redox sensitivity of the dimerization of occludin.** Cell. Mol. Life Sci. 2009; 66:3655–3662

Wachtel M, Bolliger MF, Ishihara H, Frei K, Bluethmann H, Gloor SM. **Down-regulation of occludin expression in astrocytes by tumour necrosis factor (TNF) is mediated via TNF type-1 receptor and nuclear factor-kappaB activation.** J Neurochem. 2001; 78:155-62.

Wajc E, Bakker-Grunwald T, Applebaum SW. **Binding and uptake of trypan blue by developing oocytes of *Locusta migratoria migratorioides*.** J Embryol Exp Morphol. 1977; 37:1-11.

Wallace RA, Ho T. **Protein incorporation by isolated amphibian oocytes. II. A survey of inhibitors.** J Exp Zool. 1972; 181:303-17.

Wang W, Dentler WL, Borchardt RT. **VEGF increases BMEC monolayer permeability by affecting occludin expression and tight junction assembly.** Am J Physiol Heart Circ Physiol. 2001; 280:H434-40.

Wang, J., Cieplak, P. and Kollman, P. A. **How well does a restrained electrostatic potential (RESP) model perform in calculating conformational energies of organic and biological molecules?** J Comput Chem. 2000; 21:1049-1074

Westphal JK, Dörfel MJ, Krug SM, Cording JD, Piontek J, Blasig IE, Tauber R, Fromm M, Huber O. **Tricellulin forms homomeric and heteromeric tight junctional complexes.** Cell Mol Life Sci. 2010; 67:2057-68.

Wouters FS, Bastiaens PI, Wirtz KW, Jovin TM. **FRET microscopy demonstrates molecular association of non-specific lipid transfer protein (nsL-TP) with fatty acid oxidation enzymes in peroxisomes.** EMBO J. 1998; 17:7179-89.

Wu F, Wilson JX. **Peroxynitrite-dependent activation of protein phosphatase type 2A mediates microvascular endothelial barrier dysfunction.** Cardiovasc Res. 2009; 81:38-45.

Wu S, Zhang Y. **LOMETS: a local meta-threading-server for protein structure prediction.** Nucleic Acids Research 2007; 35: 3375-82.

Xia Z, Liu Y. **Reliable and global measurement of fluorescence resonance energy transfer using fluorescence microscopes**. Biophys J. 2001; 81:2395-402.

Yu SW, Wang H, Poitras MF, Coombs C, Bowers WJ, Federoff HJ, Poirier GG, Dawson TM, and Dawson VL **Mediation of poly(ADP-ribose) polymerase-1-dependent cell death by apoptosis-inducing factor.** Science 2002; 297: 259–263.

Zhang Y, Skolnick J. **Scoring function for automated assessment of protein structure template quality.** Proteins. 2004; 57:702-10.

Zhang Y, Skolnick J. **SPICKER: a clustering approach to identify near-native protein folds.** J Comput Chem. 2004; 25:865-71.

Zhang Y, Skolnick J. **TM-align: a protein structure alignment algorithm based on the TM-score.** Nucleic Acids Res. 2005; 33:2302-9.

Zhang Y, Zhao S, Gu Y, Lewis DF, Alexander JS, Wang Y. **Effects of peroxynitrite and superoxide radicals on endothelial monolayer permeability: potential role of peroxynitrite in preeclampsia.** J Soc Gynecol Investig. 2005; 12:586-92.

Zhang Y. **I-TASSER server for protein 3D structure prediction.** BMC Bioinformatics. 2008; 9:40.

Ziegler DM. **Role of reversible oxidation-reduction of enzyme thiols-disulfides in metabolic regulation.** Annu Rev Biochem. 1985; 54:305-29.

Zimmermann T, Rietdorf J, Girod A, Georget V, Pepperkok R. **Spectral imaging and linear un-mixing enables improved FRET efficiency with a novel GFP2-YFP FRET pair.** FEBS Lett. 2002; 532:245-9.

6 APENDIX

6.1 AMINO ACID SEQUENCE OF HUMAN OCCLUDIN

Uniprot accession number Q16625

```
        10         20         30         40         50         60
MSSRPLESPP PYRPDEFKPN HYAPSNDIYG GEMHVRPMLS QPAYSFYPED EILHFYKWTS
        70         80         90        100        110        120
PPGVIRILSM LIIVMCIAIF ACVASTLAWD RGYGTSLLGG SVGYPYGGSG FGSYGSGYGY
       130        140        150        160        170        180
GYGYGYGYGG YTDPRAAKGF MLAMAAFCFI AALVIFVTSV IRSEMSRTRR YYLSVIIVSA
       190        200        210        220        230        240
ILGIMVFIAT IVYIMGVNPT AQSSGSLYGS QIYALCNQFY TPAATGLYVD QYLYHYCVVD
       250        260        270        280        290        300
PQEAIAIVLG FMIIVAFALI IFFAVKTRRK MDRYDKSNIL WDKEHIYDEQ PPNVEEWVKN
       310        320        330        340        350        360
VSAGTQDVPS PPSDYVERVD SPMAYSSNGK VNDKRFYPES SYKSTPVPEV VQELPLTSPV
       370        380        390        400        410        420
DDFRQPRYSS GGNFETPSKR APAKGRAGRS KRTEQDHYET DYTTGGESCD ELEEDWIREY
       430        440        450        460        470        480
PPITSDQQRQ LYKRNFDTGL QEYKSLQSEL DEINKELSRL DKELDDYREE SEEYMAAADE
       490        500        510        520
YNRLKQVKGS ADYKSKKNHC KQLKSKLSHI KKMVGDYDRQ KT
```

The N-terminal domain of occludin encompasses the amino acids 1 to 64. The gray regions mark the four transmembranal domains. The MARVEL domain comprises the amino acids 60 to 269 and is shown underlined with a dotted line. The C-terminal domain starts at the amino acid 266, its membrane-proximal region is highlighted in yellow and the membrane-distal underlined with a double line. The conserved regulatory region is shown in green. After the cysteine[409], a small flexible fragment, blue, connects the regulatory region with the coiled-coil domain, highlighted in red.

6.2 AMINO ACID SEQUENCE OF THE SH3-HINGE-GUK UNIT OF HUMAN ZO-1

Uniprot Accession number *Q07157*

```
       490        500        510        520        530        540
EEAVLFLLDL PKGEEVTILA QKKKDVYRRI VESDVGDSFY IRTHFEYEKE SPYGLSFNKG
       550        560        570        580        590        600
EVFRVVDTLY NGKLGSWLAI RIGKNHKEVE RGIIPNKNRA EQLASVQYTL PKTAGGDRAD
       610        620        630        640        650        660
FWRFRGLRSS KRNLRKSRED LSAQPVQTKF PAYERVVLRE AGFLRPVTIF GPIADVAREK
       670        680        690        700        710        720
LAREEPDIYQ IAKSEPRDAG TDQRSSGIIR LHTIKQIIDQ DKHALLDVTP NAVDRLNYAQ
       730        740        750        760        770        780
WYPIVVFLNP DSKQGVKTMR MRLCPESRKS ARKLYERSHK LRKNNHHLFT TTINLNSMND
```

The SH3 domain starts at the amino acid 515 and is shown in grey, the hinge region is highlighted in yellow and the GuK unit in blue.

6.3 Comparison of FRET efficiencies between conventional AP-FRET and qλ-FRET

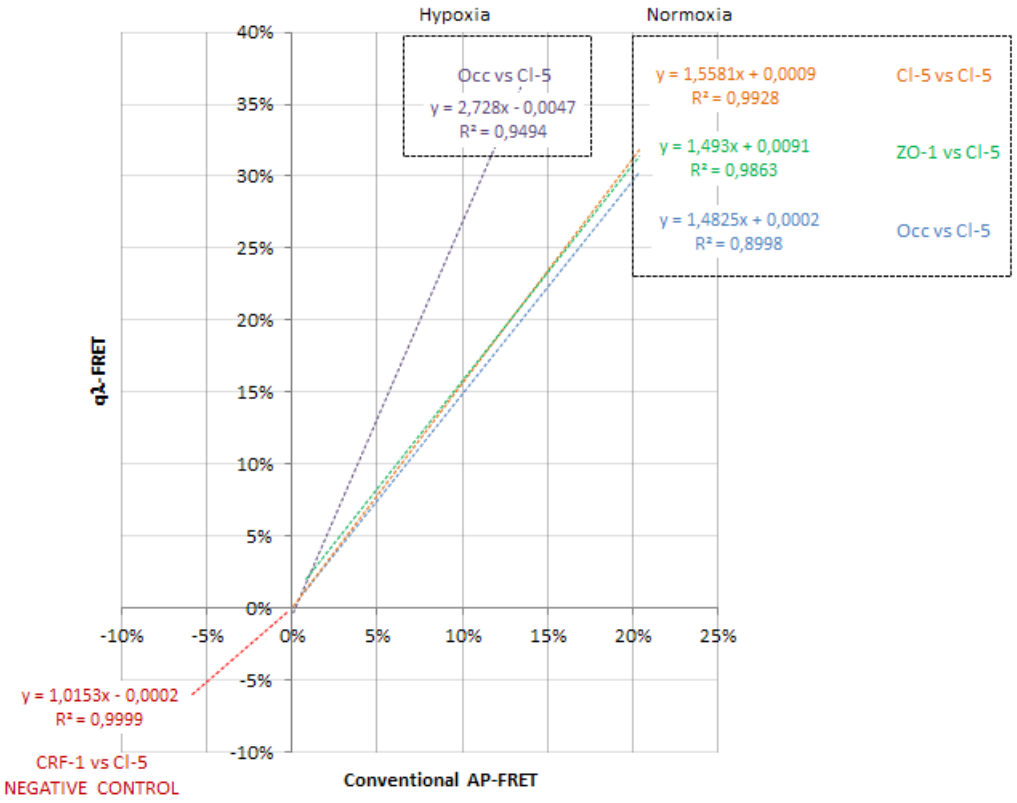

The graph shows the correlation of different FRET efficiencies measured by qλ-FRET or by conventional FRET by acceptor photobleaching (AP-FRET) for the interacting pairs, Claudin 5-CFP vs Claudin 5-YFP (orange), ZO-1 CFP vs Claudin 5-YFP (green), YFP-Occludin vs Claudin 5-CFP (blue), or the not-interacting Corticotropin releasing factor receptor -1 YFP vs Claudin-5 CFP (red – negative control). Under normoxic conditions, the qλ-FRET efficiencies were ~1.5 times of those obtained by AP-FRET. These results are in agreement with the known underestimation of energy transfer that occurs during AP-FRET due CFP quenching and lack of YFP correction (Chen et al., 2007). For the negative control, the results of both techniques were similar. During hypoxia, for the occludin and claudin-5 interaction, the qλ-FRET efficiencies were 2.7 times higher than those obtained by conventional AP-FRET.

6.4 Surface electronegativity of the dimeric coiled-coil domain of occludin

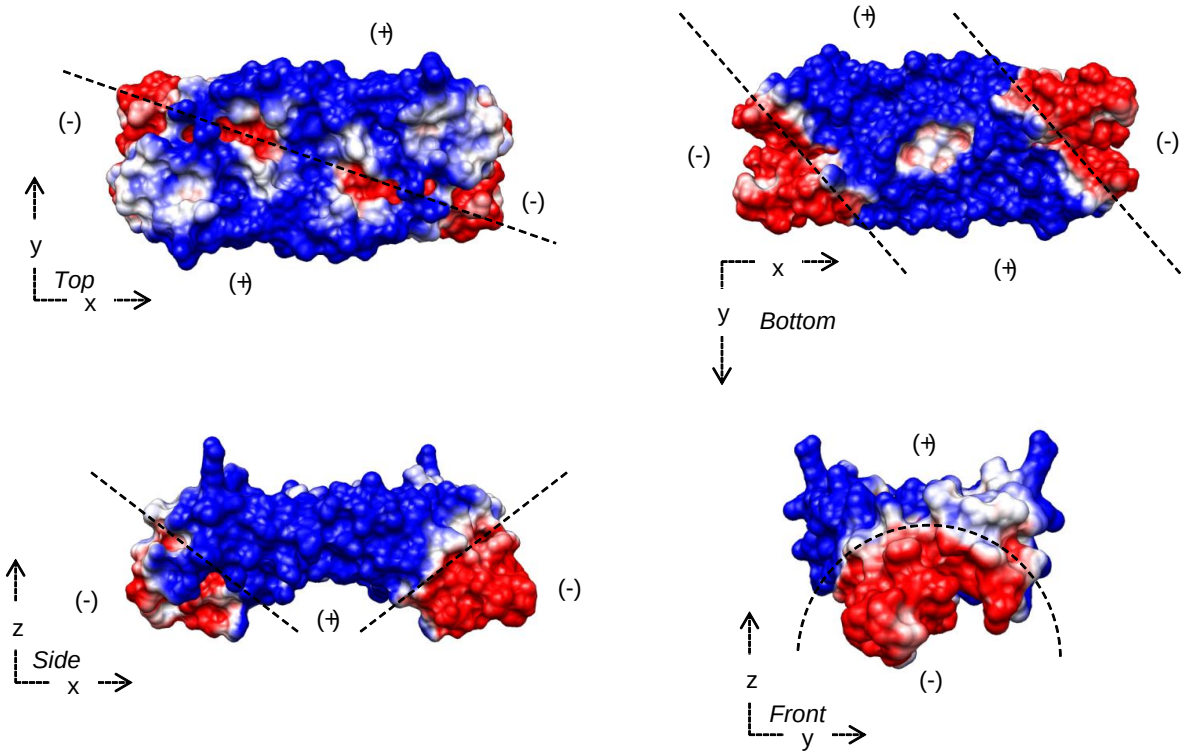

The diagonal symmetry of the charge distribution is evident. The dimer is electronegative in the inferior surface of its lateral ends. The central body of the dimer is positive as it is most of its upper surface

6.5 Surface electronegativity of the SH3-Hinge-GuK unit of ZO-1

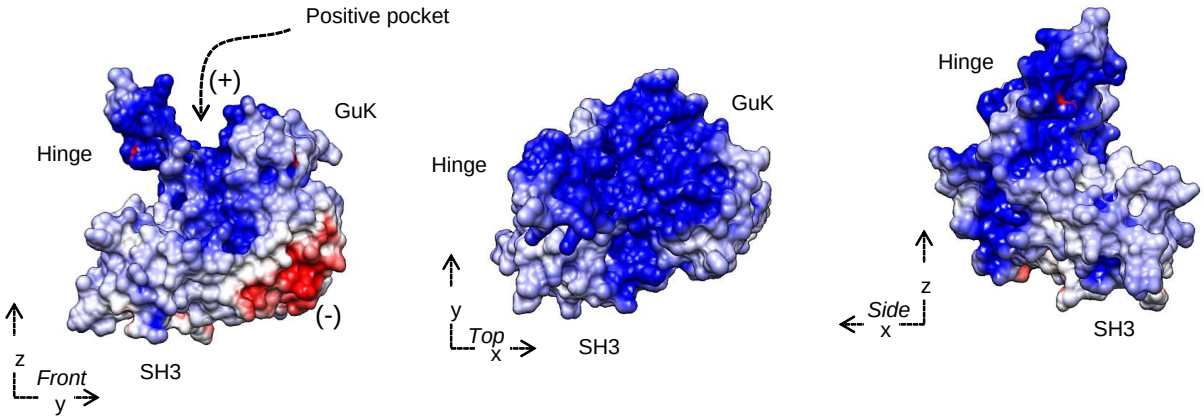

The notch where the coiled-coil domain of occludin binds is markedly electropositive (blue). All electronegative surfaces (red) are facing downwards, away from the occludin interacting region. The intensity of the colors correlates with the electrostatic charge intensities. Neutral regions are white.

6.6 PREDICTED DIMERIC ASSEMBLIES OF THE OCCLUDIN COILED-COIL DOMAIN

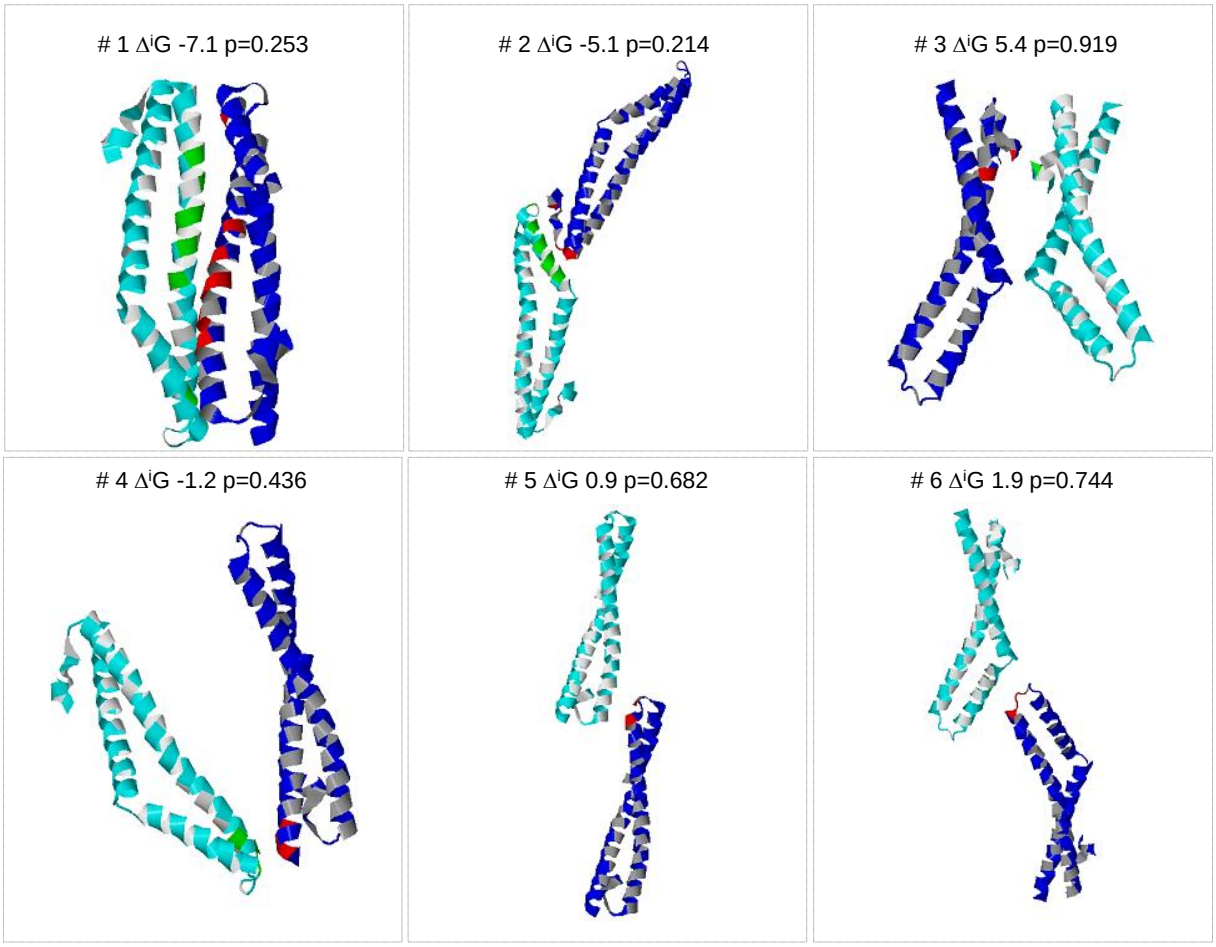

Each monomer is either dark or light blue, the interfacing residues are represented in green and red. The ΔiG and hydrophobicity p values are given for each of them.

Publications based on this work:

The content of this dissertation has been partially published in:

J.K. Walter, **V. Castro**, M. Voss, K. Gast, C. Rueckert, J. Piontek and Ingolf E. Blasig. **Redox sensitivity of the dimerization of occludin.** Cell. Mol. Life Sci. 2009; 66:3655–3662
DOI: 10.1007/s00018-009-0150-z
http://dx.doi.org/10.1007/s00018-009-0150-z

Two additional publications are currently under preparation.

Castro V., Bellmann C., Krug S., Fromm M., Blasig E. **The interplay between occludin and ZO-1 is redox sensitive and constitutes a novel tight junction regulatory mechanism** (to be submitted)

Castro V., and Blasig E. **The tight junction protein occludin is a novel NADH oxidase and regulates the cytosolic balance of NADH/NAD+** (to be sumbitted)

Awards:

This work has been presented partially in a number of local and international conferences where it has been awarded:

Bellman C, **Castro V**, Krug S, Fromm M, Blasig I.
The dimerization of occludin is a precondition for the redox sensitive interplay between occludin and ZO-1 and constitutes a novel tight junction regulatory mechanism.
9th International Conference on Cerebral Vascular Biology, Leiden, The Netherlands.
June 2011

Victor Castro, Christian Bellmann, Susanne Krug, Michael Fromm and Ingolf Blasig
The Occludin / ZO-1 interplay evidences a novel TJ regulatory mechanism based on the redox sensitivity of occludin dimerization
13th International Symposium of Signal Transduction in the Blood Brain Barrier. Zürich, Switzerland.
September. 2010.

Victor Castro, Christian Bellmann, Susanne Krug, Michael Fromm and Ingolf Blasig
Occludin forms a disulfide bridge in order to dimerize and recruit ZO-1 to the cell membrane
Life under reconstruction. Berlin, Germany.
May. 2010

Other publications:

M. Singh Bal*, **V. Castro***, J. Piontek, C. Rueckert, J.K. Walter, A. Shymanets, A. Kurig, H. Haase, B. Nuernberg and I. E. Blasig. **The hinge-region of the scaffolding protein of cell contacts Zonula occludens protein 1 interacts with various signaling proteins.** Submitted (May 2011 - Journal of Cell Science)

* Contributed equally

VICTOR MANUEL CASTRO VILLELA
CURRICULUM VITAE

DUE TO DATA PROTECTION REASONS, THE CURRICULUM VITAE IS NOT INCLUDED IN THE ONLINE VERSION

VICTOR MANUEL CASTRO VILLELA
CURRICULUM VITAE

DUE TO DATA PROTECTION REASONS, THE CURRICULUM VITAE IS NOT INCLUDED IN THE ONLINE VERSION

VICTOR MANUEL CASTRO VILLELA
CURRICULUM VITAE

DUE TO DATA PROTECTION REASONS, THE CURRICULUM VITAE IS NOT INCLUDED IN THE ONLINE VERSION

VICTOR MANUEL CASTRO VILLELA
CURRICULUM VITAE

DUE TO DATA PROTECTION REASONS, THE CURRICULUM VITAE IS NOT INCLUDED IN THE ONLINE VERSION

VICTOR MANUEL CASTRO VILLELA
CURRICULUM VITAE

DUE TO DATA PROTECTION REASONS, THE CURRICULUM VITAE IS NOT INCLUDED IN THE ONLINE VERSION